USC–SIPI REPORT #233

Localization from Near-Source Quasi-Static Electromagnetic Fields

by

John Compton Mosher

May 1993

Signal and Image Processing Institute
UNIVERSITY OF SOUTHERN CALIFORNIA
Department of Electrical Engineering-Systems
3740 McClintock Avenue, Room 404
Los Angeles, CA 90089-2564 U.S.A.

Dedication

My patient wife, Diana.

Acknowledgments

Professor Richard M. Leahy has been invaluable to me for his guidance. He directed me to a very interesting topic, then provided me the background, resources and contacts to pursue the research. I also thank the members of my guidance committees: Professors Lloyd Griffiths, Manbir Singh, George Bekey, and C.C. Kuo. I also thank Professor Jerry Mendel for his early guidance in my program.

Another person important to my research program was Dr. Paul S. Lewis and his support from the Los Alamos National Laboratory Graduate Research Program. In addition to thoroughly reviewing my publications, Paul provided me access to the Biophysics Group of Los Alamos. Their director, Dr. Chris Wood, provided opportunities for me to present and test my research against his group's research data. I particularly thank Dr. Jeff Lewine for his phantom data, Dr. Cheryl Aine for her feedback on the algorithms, and Dr. Heidi Schlitt for her clarifications on my notation.

At Scientific Applications & Research Associates, I thank Dr. Parviz Parhami and Dr. Timothy Rynne for encouraging me to submit the NASA Small Business Innovations Grant proposal. I also thank NASA for providing me the funding to apply my research against their weather data. I also thank Tim for his input on thunderstorm physics and assistance in interpreting the basic storm models.

At TRW, Dr. Parviz Parhami and Dr. Charles Wuller of SEDD supported my application for the fellowship program. In the last years, as the defense cutbacks resulted in company reorganizations, Dr. Brad Flanders and Barry Pearce of ATD gave me important support to finish the program.

At the University of Southern California, Dr. Xiao-hong Yan, Zhenyu Zhou, Dr. Zhenyu Wu, Xiao-feng Zhao, Dr. Samuel Song, and Erkan Mumcuoglu all added

Table of Contents

List of Figures

List of Tables

Abstract

A wide range of research has been published on the problem of estimating the parameters of electromagnetic and acoustical sources from measurements of signals measured at an array of sensors. In the quasi-static electromagnetic cases examined here, the signal variation from a point source is relatively slow with respect to the signal propagation and the spacing of the array of sensors. As such, the location of the point sources can only be determined from the spatial diversity of the received signal across the array. The inverse source localization problem is complicated by unknown model order and strong local minima.

The nonlinear optimization problem is posed for solving for the parameters of the quasi-static source model. The transient nature of the sources can be exploited to allow subspace approaches to separate out the signal portion of the spatial correlation matrix. Decomposition techniques are examined for improved processing, and an adaptation of MUltiple SIgnal Characterization (MUSIC) is presented for solving the source localization problem. Recent results on calculating the Cramer-Rao error lower bounds are extended to the multidimensional problem here.

This thesis focuses on the problem of source localization in magnetoencephalography (MEG), with a secondary application to thunderstorm source localization. Comparisons are also made between MEG and its electrical equivalent, electroencephalography (EEG). The error lower bounds are examined in detail for several MEG and EEG configurations, as well as localizing thunderstorm cells over Cape Canaveral and Kennedy Space Center. Time-eigenspectrum is introduced as a parsing technique for improving the performance of the optimization problem.

Chapter 1

Introduction

A wide range of research has been published on the problem of estimating the parameters of electromagnetic and acoustical sources from measurements of signals at an array of sensors. In the quasi-static electromagnetic cases examined here, the signal variation from a point source is relatively slow with respect to the signal propagation and the spacing of the array of sensors. Consequently, the location of the point sources can only be determined from the spatial diversity of the received signal across the array. The inverse source localization problem is complicated by unknown model order and strong local minima.

This thesis focuses on the problem of source localization in magnetoencephalography (MEG), with a secondary application to thunderstorm source localization. The processing of magnetoencephalography (MEG) data distinguishes itself from conventional array processing techniques on several points. The evoked response signal received at the array is transient. Preferably, assumptions about an appropriate model for the transient are minimal, thus precluding the use of pattern matching or matched filtering techniques. The signal is assumed quasi-static, so that fluctuations in the signal arrive simultaneously at all sensors and thus no time-of-arrival information is available. The location must be derived solely from the spatial disparity of the signal across the array, hence the "near-source" designation of this research. The evoked response time series from distinct sources can be assumed to be at best only linearly independent, so that partial temporal coherence often degrades minimum variance approaches. Conventional approaches reduce coherence through spatial smoothing, which depends on the

shift invariance of an array; the spatial disparity of the MEG signal makes this approach inappropriate. The MEG dipole model generates a three-dimensional manifold, such that the orientation or "polarization" of the neural source must be considered. The MEG model also suffers from a rank deficiency in the radial direction, which can complicate the formulation.

These differences notwithstanding, the MEG model can be recast into formulations similar to other source localization problems. This dissertation examines in detail the basic MEG current dipole model and its variations, then presents methods for solving for the parameters of the model, beginning with the conventional nonlinear least-squares approach. A suboptimal approach to solving the difficult nonlinear problem is introduced, then shown to be a variation of MUltiple SIgnal Characterization (MUSIC). Cramer-Rao Lower Bounds for the multidimensional array manifold problem are derived, then simplified to a meaningful closed form expression for lower bounds on localization error. The technique of time-eigenanalysis is introduced to analyze the short-time correlations in the signal. Information from the time-eigenanalysis is used to parse the transient neural signal into appropriate segments that enhance the SNR and success of the MUSIC techniques.

This research and its extensions of array signal processing techniques are also applicable to other problems of near-source quasi-static electromagnetic fields. In addition to demonstrating the novel approaches with the MEG model, this thesis also presents applications in electroencephalography (EEG) and thunderstorm source localization. We discuss the background of the MEG model in more detail below. We then follow with a brief introduction to the thunderstorm source model.

Chapter 2
Localization Background

2.1 Magnetoencephalography

Magnetoencephalograms (MEG) (and electroencephalograms (EEG)) are non-invasive methods of studying the functional activity of the human brain with millisecond temporal resolution. Much of the work in MEG and EEG in the last few decades has been focused on estimating the properties of the internal sources of the fields from the external measurements (e.g., Snyder 1991). The most straightforward model for describing the external evoked magnetic field or surface evoked potential is the single equivalent current dipole. This model and its variations, both in EEG and MEG, contains a transfer function or lead field model to relate each dipole's intensity, orientation, and location to the externally measured fields. The general inverse problem is to find the three location parameters and the three moment parameters that comprise the unknown parameters for each dipole.

An array of Superconducting QUantum Interference Device (SQUID) biomagnetometers may be used to measure the spatio-temporal magnetoencephalogram (MEG) produced by the brain. Given these external magnetic field measurements, one would like to compute a "neuromagnetic image," specifying the three-dimensional current density that produced the magnetic field. Accomplishing this requires inversion of the Biot-Savart law. Unfortunately, this general inverse problem is ill-posed because different neural current distributions may produce the same external field measurements. As a result, physical models of the underlying current distributions are employed; Williamson et al. (1983) provide a good overview of the general topic.

3

Of particular interest is the localization of the neural currents evoked in response to a given sensory stimulus, such as auditory or visual. An external magnetic field may be produced by this *primary* neural current, for which the simplest and most widely used composite model is the "dipole in a sphere." Here, the primary current is modeled as a *current dipole* or set of dipoles, and the head is modeled as a conductive sphere. A current dipole can accurately model neural activity localized to one site, representing the coherent activation of a large number of individual neurons (Scherg and von Cramon 1985a). The *return* or global *volume* currents are distributed over the sphere of the head, and the external magnetic field generated by the volume currents has no component normal to the head surface (Trip 1982, Ilmoniemi *et al.* 1985, Sarvas 1987). Thus, in this simple model, the component of the magnetic field oriented radially from the head is produced by the primary dipole current alone.

Given a suitable source and head model, the inverse problem can be reduced to the nonlinear optimization problem of computing the location and moment parameters of the set of dipoles whose field best matches the MEG measurements in a least-squares sense. Singh *et al.* (1984) discussed neuromagnetic imaging (NMI), which extends the dipole model by assuming a large set of current dipoles, each with a fixed location at the center of a voxel (volume element) of a three-dimensional volume within the brain. The MEG data and image are linearly related; however, because of the large number of unknowns in the three-dimensional image, there is generally not a unique solution. Ilmoniemi *et al.* (1985) described the general forward problem and presented minimum norm inverse solutions. Jeffs *et al.* (1987) investigated several cost functions to select an appropriate solution from the set of feasible solutions. Dallas (1985) investigated the imaging problem using a direct Fourier-based inversion approach, Alvarez (1990) recently presented Fourier-based solutions for the two-dimensional case, and Wikswo *et al.* (1990) have had success in imaging two-dimensional objects with their MicroS-

4

QUID apparatus. In this thesis we present methods for solving for a small parsimonious set of dipoles as a means of avoiding the ill-posed problem associated with the full three-dimensional image model.

As in all modeling situations, a trade-off exists between model complexity and generality and the ability to reliably estimate the model parameters from the given measurement data. Initial MEG dipole models used single time "snapshots" of the measured spatial magnetic field, where a spatial dipole model was fitted at an instance in time, usually at a local or global response peak. These MEG models are direct counterparts of EEG dipole models, known as *instantaneous state* dipole models (Wood 1982). To increase the complexity of the source models that can be effectively employed, researchers have begun to incorporate temporal modeling assumptions. The addition of a temporal model increases the range of the measurements that can be used in model fitting. A *spatio-temporal* dipole model and the necessary associated assumptions are presented in detail in (Scherg and von Cramon 1985a, Scherg 1989).

The spatio-temporal models differ in the manner in which they describe the time dependence of the data. Scherg and von Cramon (1985a, 1985b) use dipoles fixed in an unknown location *and* orientation, and therefore the time dependence is represented by a scalar time series specifying the magnitude and polarity of the current flow. Maier *et al.* (1987) implicitly assume the same model, but use principal components analysis (PCA) to derive the locations. Achim *et al.* (1988) compare the instantaneous state dipole model with PCA dipole fitting and spatio-temporal modeling; in their three-dipole fixed orientation spatio-temporal model, they assume that two of the dipoles are known in orientation and location (information obtained from the instantaneous state dipole model), and thus search for only one unknown dipole location and orientation. In (Scherg and von Cramon 1986), Scherg and von Cramon have fixed location, but unconstrained orientation, and they introduce the idea of *dipole source potentials*, or *regional*

dipoles (Scherg 1989), where three *elemental dipoles* with orientations in orthogonal directions may occupy the same physical location.

These differences in formulation can be grouped into three spatio-temporal dipole models: i) unconstrained ("moving and rotating") dipoles, ii) dipoles with a fixed location ("rotating" or "regional"), and iii) dipoles with a fixed location and a fixed orientation ("fixed"). We assume that the parameters of location, orientation, and magnitude are all unknown. Our intent here is not to argue the merits of one model over another, but rather to show how each model may be solved efficiently within a common linear algebraic framework. In each case, we show that the model can be mathematically reduced to the same general expression, allowing the same approach to finding the inverse solution. This expression will unify our approach to solving the inverse problem, no matter which model we choose.

Neuromagnetic fields are very weak, ranging from 10^{-12} to 10^{-14} tesla (T). In comparison, the Earth's magnetic field is in the μT region at about 5×10^{-5} T and urban background noise can generate fields roughly at 10^{-6} T. Measurements are made typically in a magnetically shielded room using superconducting quantum interference devices (SQUIDS) in conjunction with a gradiometer configuration for the pickup coils. To keep the noise of the electronics below that of the fields, as well as achieve superconductivity, the entire sensor arrangement is refrigerated to near absolute zero in a Dewar filled with liquid helium.

Fig. 1 displays a schematic illustration of a single sensor system. The gradiometer configuration uses pickup coils wound in opposing directions, such that spatially distant signals are canceled as they pass through all of the coils. The weak and dissipating neural fields effectively pass only through the nearest coil and are therefore not canceled. The single channel system is also expanded to 7 and 37 channel systems. More

6
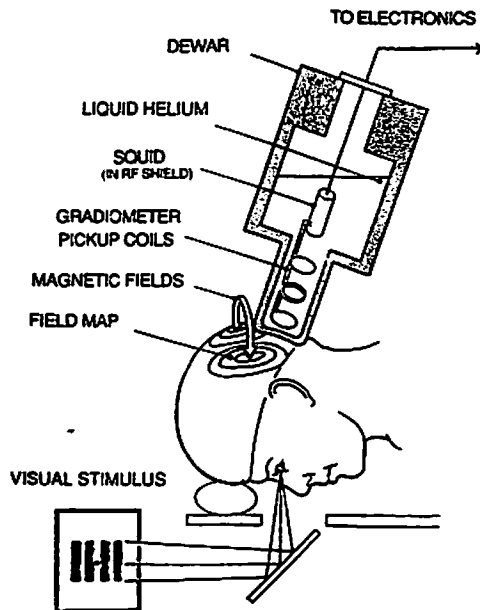
FIGURE 1. Single MEG sensor schematic from (Lewis and George 1990). The single channel sensor depicted here is also configured in a 7 and 37 sensor "bowl"-like arrangements, which allow the cluster of sensors to be placed next to the scalp. Other arrangements include a helmet of fixed sensors sites about the entire head.

recently, a 61 position "helmet" with two sensor orientations per position was introduced, as well as a 64 channel first-order gradiometer system.

The diameter of the pickup coil is typically 1-2 cm, and the sensor integrates the magnetic flux passing normal through the plane of the coil. The thickness of the Dewar wall, the thickness of the skull, and the minor standoff of the Dewar from the patient's scalp typically separate the coil and the nearest neural source by at least 1-2 cm. In (Jeffs et al. 1987), simulations show that each of the gradiometer coils can be reasonably replaced with a simpler point source sensor model measuring the field at the center of the coil.

7

In EEG, the typical use of the sensor data is to generate three dimensional contours by interpolating between the data points. Given MEG sensors' much greater cost, generating contours from MEG data offers little advantage. The focus has instead been on source localization, which attempts to infer from these external magnetic fields what and where the underlying sources were. Although EEG data has also been used for attempts at source localization, the simplicity of the MEG model (discussed in Chapter 3) relative to the EEG model implies a greater chance for success in arriving at a solution.

In Chapter 3, we present each of the three data models, and in Chapter 4, we discuss the calculation of the error function in fitting these models to spatio-temporal data. In Section 4.2, we present a computer simulation to illustrate the performance of these spatio-temporal modeling techniques. Chapter 5 presents a new suboptimal but faster method of solving the least-squares problem using a *subspace scanning* approach. In Section 5.2, we discuss how this subspace scanning is statistically equivalent to the MUltiple SIgnal Classification method (MUSIC) (Schmidt 1986). We also present analysis to show that although PCA dipole fitting is similar to these subspace methods, PCA will generally fail in the multiple dipole case, whereas these methods will generally succeed. We present a simulation of this scanning method, using the same example data from Section 4.2. We then present results from an actual somatosensory experiment.

2.2 Electroencephalography

As part of the Cramer-Rao Lower Bound studies presented in Chapter 7, we compare the lower bounds of magnetoencephalographic arrays with those of electroencephalographic arrays. The research and computational work of the EEG specific formulas was conducted by Michael E. Spencer. A summary of the EEG model is presented in Section 3.3 and in (Mosher *et al.* 1993). For our purposes in this dissertation, the EEG

8

model is treated as a variation of the MEG manifold, although obviously more complicated. Background and derivation details will be presented in Mr. Spencer's dissertation.

2.3 Thunderstorm localization

Lightning has always been a primary safety concern at NASA. Most systems concentrate on detecting lightning occurrence and locations, but do not locate the source of the lightning. Kennedy Space Center (KSC) is high on the isokeraunic curve averaging 80 to 90 days per year during which thunderstorm activities occur. This frequency of activity greatly influences both normal operations and launch operations. The electric field mill network is an electrical system, deployed at KSC, of which the implementation provides information on lightning location and storm electrification. The electric field mill network, however, does not identify the electric field structure aloft. NASA has criteria that limit activities and launches when field levels exceed 1kV/m. A more accurate determination of the distribution and strength of storm cells is needed to assess their ability to produce triggered lightning. If a new technique could infer the electric field structure aloft from ground-based data, NASA could improve lead time to issue and cancel storm warnings.

We adapted the MUSIC eigenanalysis approach developed in this research, which allows us to scan three dimensional space searching for multiple electromagnetic sources. This technique should significantly enhance NASA's ability to characterize potential electrified sources and thus enhance the ability to determine the probability of triggering lightning with launch vehicles. This new method is very graphically oriented in a manner quite consistent with existing RADAR and lightning systems in use, and therefore should readily integrate into forecasters' needs for rapidly assessing information in a real-time operational environment. The end goal is to process the data from the KSC field mill into useful interpretations about the nature of an electrified storm cell.

This dissertation includes summaries of some of our activities under a grant from NASA KSC.

Cloud generation, electrification, and thunderstorm physics are complex and well beyond the scope of this dissertation. However, at the simplest modeling level, the thunderstorm localization problem at NASA is remarkably similar to the MEG/EEG problem. An isolated thunderstorm cell can be modeled as a point charge positioned above a perfect grounding plane. The electric field at the Earth's surface ranges from -300 volts/meter (v/m) in fair weather to as high as +15,000 v/m as a storm cell passes directly overhead. Excepting lightning strikes, the signal recorded by a ground-based array of sensors is effectively quasi-static, and inverting the array of signals and determining the source locations suffers from the same problems that plague MEG and EEG research.

The electric field mill in use at Kennedy Space Center-Cape Canaveral Air Force Station (KSC-CCAFS) is shown conceptually in Fig. 2, along with a photograph of field mill 4. An overview of the field mill theory and design is presented in (Maier and Strange 1988). The KSC-CCAFS field mill array comprises 31 such field mills in a network across the Cape, as structured during the summer of 1991. Fig. 3 presents the location of the sensors, numbered 1 to 34; sensor numbers 3, 24, and 31 were not used. The mills measures the DC and low frequency electric field (to 5 Hz) at the Earth's surface, producing a measurement situation not unlike MEG or EEG.

The data sets recorded at CCAFS are based on a 10 bit digital word sampled 60 times a second. The base quantization level is 30 v/m, with the zero baseline set at codeword 512 (out of 1024 possible). The dynamic range is limited to codewords between 12 and 1012, representing values of +/- 15 kV/m. The data stream from all sensors is time-tagged and recorded continuously. Reduced 10 samples per second data sets are also made available.
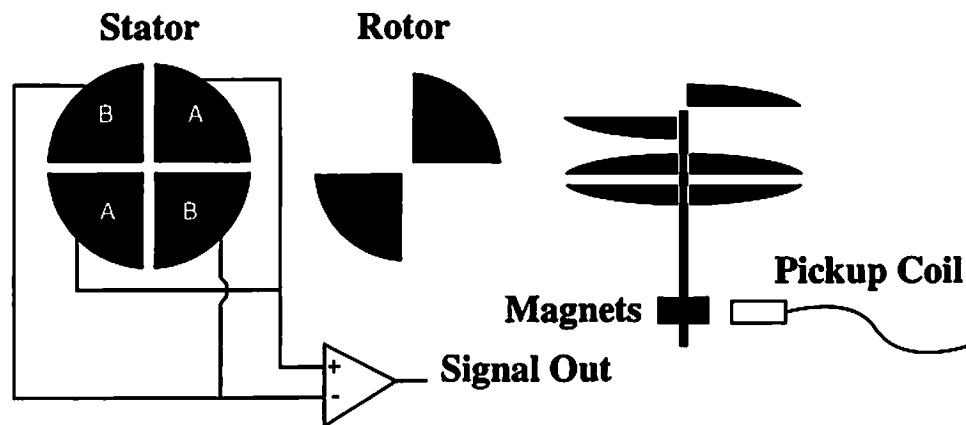
FIGURE 2. Exploded view of the mechanical parts of an electric field mill and the basic wiring of the stator plates (Maier and Strange 1988). The pickup coil senses the alignment of the rotor blades over the stator blades and picks off the signal from the differential amp. At the bottom is a photograph of Field Mill #4 in operation. The cement pad at the base of the sensor is two foot by two foot in dimensions.

11
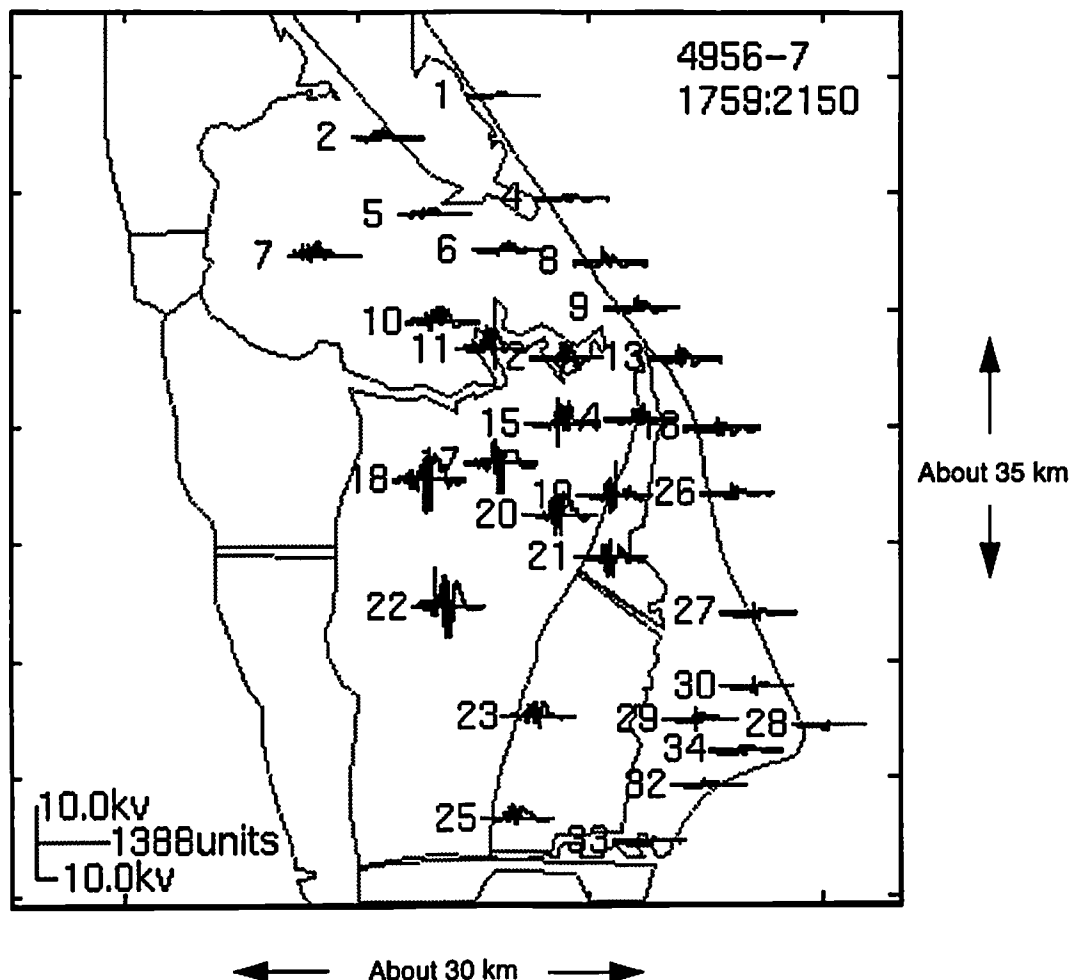
FIGURE 3. The electric field mill network at Kennedy Space Center and the Cape Canaveral Air Force Station, as configured during the summer of 1991. Overlaid is the sensor response to a thunderstorm over a four hour period. We note that the storm is apparently to the west of the KSC array and somewhat southern, as seen by the relative lack of activity on the oceanside and northern sensors.

Because NASA has no reliable source inversion technique to use operationally, the primary use of the data is for generating contour maps. The contours are generated from one minute averages and updated every five minutes in normal operations. The contour algorithm is based on an exactly constrained set of linear equations, representing a set of point charges of unknown intensities six kilometers above each field mill. The model is inverted to obtain the charge intensities, then these charge intensities are used in a new forward model representing a fine contour grid. Isocontours are typically drawn

12

at 1000 V/m, and the zero contour specially denoted. Interpretation of the contours is not unlike interpretations of EEG contours.

In theory, the field mill can also be used to assess lightning strikes, as described in (Maier and Strange 1988). In practice, the role of detecting and locating cloud to ground lightning strikes is assumed by specialized detection arrays, such as the National Lightning and Detection Network. The electric field mill represents one of several modalities in use by operational personnel to assess thunderstorm threats. The primary tools in assessment, in order of importance, are weather radar, lightning detection, and electric field mill data.

The primary operational procedure for the field mill data focuses on the field level value; in general, values above 1 kV/m will halt launch operations, and values above 2 kV/m will halt ground operations. Unfortunately, these levels are also found under non-threatening conditions, such as fog, smoke, or sea spray. The limitation in setting better launch and ground field mill criteria appears to center on the need for objective interpretations of the array output. Indeed, one of the promises of the techniques presented in this research is to better integrate the interpretation of field mill data into real-time operations, such that unnecessary operational halts can be avoided.

As an example of a data set, Fig. 3 shows the electric fields recorded over a four hour period, as a storm grew, then dissipated. Fig. 4 shows an overlay of all of the sensor recordings. The tail portion of this data set will be examined more closely as an application of time-eigenspectrum and MUSIC (Section 9.3).
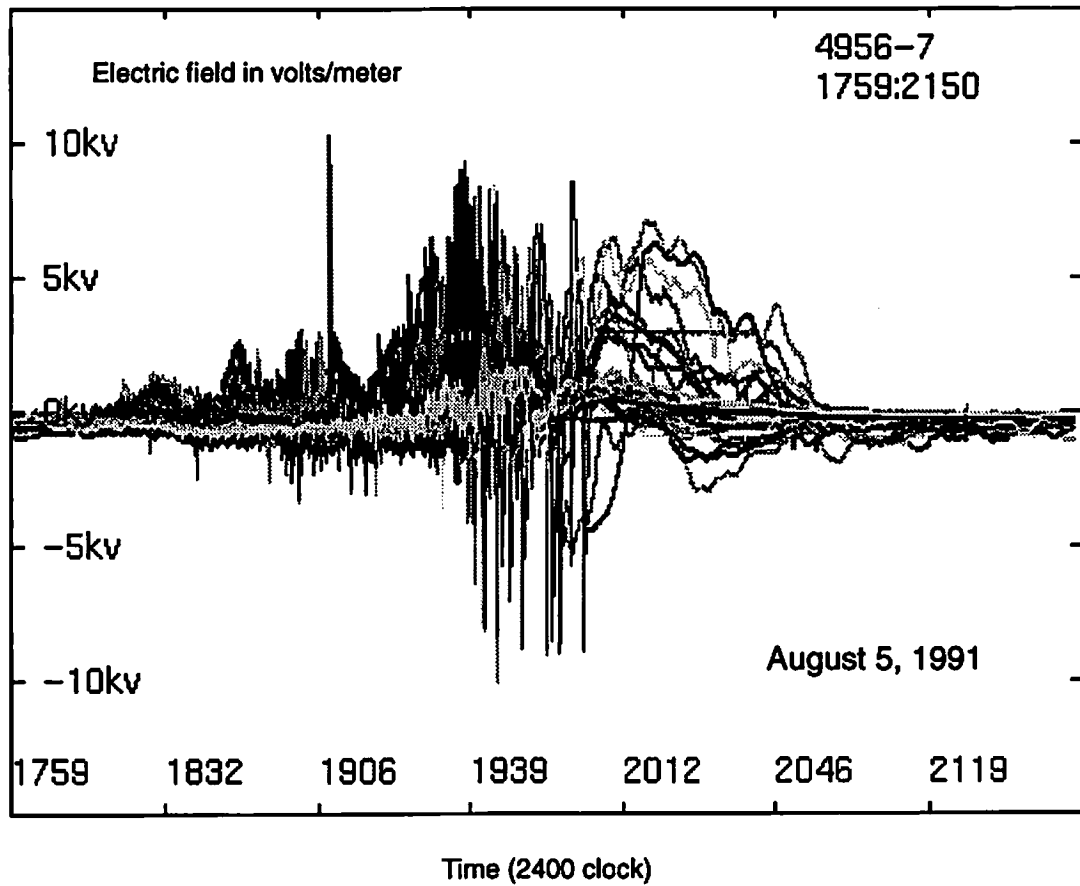
FIGURE 4. August 5, 1991 KSC data set. Fig. 3 shows the spatial distribution of the data about the Cape. This figure is the overlay of those data sets.

14

Chapter 3
Forward Models

In this chapter we first discuss the general spatiotemporal model common to MEG, EEG, and the thunderstorm localization. We then present MEG and EEG version of the "dipole in a sphere" model, where sources are represented by current dipoles, and the head is modeled as a four concentric shell sphere. This model illustrates how we adapt a specific MEG or EEG model to the general electromagnetic model, which is in turn used to determine the Cramer-Rao lower bounds. We then follow with a brief summary of the simple thunderstorm model.

As discussed in the chapter "Localization Background" on page 3, physical models are used to represent both the neural current sources and the enclosing head shape and conductivity. Source models range from simple current dipoles to complex current surfaces. Head shape and conductivity models range from spherically symmetric conductors to finite element models based on individual anatomy. The combination of source and head model is known as the forward model. Given any arbitrary static current distribution, the magnetic field can be obtained from the Biot-Savart law. For source dipoles in a spherically symmetric conductor, Ilmoniemi *et al.* (1985) point out that the source model can be reduced to consideration of just the primary source elements, regardless of the orientation of the sensors outside of the sphere. If the measurements are restricted to the radial orientation, the model simplifies further (Ilmoniemi *et al.* 1985, Sarvas 1987).

Although the degree of complexity can vary greatly, in all cases the forward model specifies the complete current distribution within the head via a set of source

parameters (e.g., locations, magnitudes). In other words the forward model provides a mapping from the source parameters to the resulting magnetic fields. In general, we can partition the parameters of any forward model into linear and nonlinear parameters. In this chapter, we show how this partition of spatiotemporal models provides a convenient algebraic form, a form which highlights the difficult nonlinear parameters. Although our development utilizes a specific forward model–current dipoles in a spherically symmetric conductor–the basic approach can be applied to any forward model.

3.1 General Model

By the superposition of electromagnetic sources, we can always separate the intensity of the sources as a linear term, whether we are considering these simple EEG and MEG spherical models or any other combination of head and source model. The vector of measured samples at time j can be modeled as

$$a(j) = \sum_{i=1}^{p} G(l_i)q_i(j) = [G(l_1), ..., G(l_p)] \begin{bmatrix} q_1(j) \\ ... \\ q_p(j) \end{bmatrix} = G(l)q(j), \qquad \text{(EQ 1)}$$

where $a(j)$ represents the column vector of surface potential or magnetic field measurements, or a combination of both. Column vectors l and q are both concatenations of the parameters for p dipoles, $l = \begin{bmatrix} \vec{l}_1, ..., \vec{l}_p \end{bmatrix}^T$ and $q = \begin{bmatrix} \vec{q}_1, ..., \vec{q}_p \end{bmatrix}^T$. The vector $\vec{l}_i$ represents the three-dimensional location of the ith current dipole, and $\vec{q}_i$ represents the corresponding three-dimensional dipole moment. The matrix $G(\vec{l}_i)$ represents the "gain transfer" matrix for the ith dipole, which relates the dipoles' moments to the vector of measurements and has a nonlinear dependence on the dipole locations.

For n time slices, we can extend this model by assuming that the dipole locations are fixed, yet allowing the dipole moments to vary with time:

$$A = [a(1), ..., a(n)] = G(l) [q(1), ..., q(n)] = G(l)Q \quad . \qquad \text{(EQ 2)}$$

We present in the next section a detailed description of the MEG model, then follow it with an overview of the EEG model and the thunderstorm model. The EEG model derivation and its partial derivatives were provided by Michael E. Spencer.

3.2 MEG Model

3.2.1 Biot-Savart Law

In this section, we present the Biot-Savart law in a convenient discrete matrix notation for discrete source elements, which we then use to develop the spatiotemporal dipole models commonly used in MEG research. The general model in every case requires determining the unknown set of parameters $\{l, M, S\}$. The linear time varying parameters, S, can always be found using a direct pseudoinverse solution, but, in general, the time invariant location parameters, l, must be found using an iterative nonlinear minimization algorithm. The block diagonal matrix, M, depends on whether we use the rotating or fixed dipole model; in the rotating model, M is simply an identity matrix, and in the fixed model, M contains the unit orientation parameters, m. The goal here is to show that each model can be expressed in a common framework and solved in a similarly efficient manner.

We begin by examining the model for a single dipole, then expand this model to account for multiple dipoles. Establishing an origin, denoting the pth dipole position

as l_p, and observing the mth measurement at sensor location p_m, we can write the Biot-Savart law for a current dipole as

$$b_m = k \frac{q_p \times (p_m - l_p)}{\|p_m - l_p\|^3} ,$$

(EQ 3)

where $k = \mu_0 / (4\pi)$ is a constant, q_p is the dipole moment, l_p is the dipole location, p_m is the ith measurement sensor location, and b_m is the magnetic field at p_m. A SQUID bio-magnetometer is used to acquire the magnetic field at position p_m, but it measures only one component of the three-dimensional field. Thus, only a scalar measurement is made:

$$b_m = b_m \cdot r_m ,$$

(EQ 4)

where r_m denotes the unit orientation of the mth sensor. The operation " $\cdot$ " denotes the dot product of two vectors.

Combining equations (3) and (4) yields

$$b_m = k \frac{(p_m - l_p) \times r_m \cdot q_p}{\|p_m - l_p\|^3} = g_m \cdot q_p$$

(EQ 5)

The vector g_m can be viewed as a gain vector, relating the moment intensity of the dipole to the measurement at position p_m. If we let each gain vector be represented as a 1×3 row vector and the moment as a 3×1 column vector, then we can arrange the measurements from m locations in a matrix form,

$$b = \begin{bmatrix} b_1 \\ \dots \\ b_m \end{bmatrix} = k \begin{bmatrix} \dfrac{(p_1 - l_p) \times r_1}{\|p_1 - l_p\|^3} \\ \dots \\ \dfrac{(p_m - l_p) \times r_m}{\|p_m - l_p\|^3} \end{bmatrix} \begin{bmatrix} q_p \end{bmatrix} = \begin{bmatrix} g_1 \\ \dots \\ g_m \end{bmatrix} \begin{bmatrix} q_p \end{bmatrix} = G_p(l_p, p) q_p .$$

(EQ 6)

The matrix $G_p(l_p, p)$ can be considered to be the gain or relationship between a unit moment source at l_p and the column vector of measurement locations p. From this

18

form we clearly see the linear relationship between the moment q_p and the measurements vector b. As we will show in Section 4.1.2, this form also focuses our attention on the more difficult nonlinear parameters in the matrix $G_p(l_p, p)$.

Although derived for a single dipole, each column in $G_p(l_p, p)$ could also be viewed as the model for three elemental dipoles or *dipole source components*, with all three sharing the same location, but in oblique directions (Scherg and von Cramon 1986). For simplicity, we will continue referring to these collocated elemental dipoles as one dipole, with moment q. This model easily extends to the multiple dipole (not collocated) case by superposition. For p dipoles,

$$b = \begin{bmatrix} G_1 & \cdots & G_p \end{bmatrix} \begin{bmatrix} q_1 \\ \cdots \\ q_p \end{bmatrix} \qquad \text{(EQ 7)}$$

or simply $b = G(l, p)q$, where $G(l, p)$ can be partitioned into the smaller matrices $G_p(l_p, p)$, as defined in (6). Similarly, q may be partitioned as the concatenation of the moment vectors for each of the p dipoles. For m sensors and p dipoles, vector b is $m \times 1$, matrix G is $m \times 3p$, and vector q is $3p \times 1$. For notational simplicity, we usually drop the dependence on l and p from our notation of G.

3.2.2 Dipole in a Sphere

Our model in Equation (7) describes the external magnetic field as the sum of the individual fields from p dipoles. For simplicity in deriving the model, the biomagnetometer is assumed to make a perfect point field measurement. We also assume that this field is due to the local primary current only, as we are ignoring the global volume or return currents. In more sophisticated head and source models, the return currents, the finite coil area, and the gradiometer configuration of a practical SQUID biomagnetometer

could also be included, resulting in a very similar formulation to that presented here (Ilmoniemi *et al.* 1985, Sarvas 1987, Jeffs *et al.* 1987).

Many researchers have correctly noted that only the two tangential dipole moment components need be computed for the "dipole in a sphere" model. A radially oriented dipole inside a spherically symmetric conductor produces no external magnetic field, since the field from the surface return currents cancels the field from the primary dipole current (Trip 1982, Ilmoniemi *et al.* 1985, Sarvas 1987, Nunez 1986, Williamson and Kaufman 1981). Additionally, the magnetic field normal to the surface of the sphere (i.e., radial from the center of the sphere) is due solely to the primary *tangential* dipole currents; volume or return currents in the surface of the sphere contribute nothing to the radial magnetic field.

A common MEG geometry is therefore an array of sensors arranged radially about the surface of the head, which is sensitive only to the tangentially oriented primary dipole currents. As noted by (Ilmoniemi *et al.* 1985, Sarvas 1987), the nonradial sensor orientations record magnetic fields that are also functions of only the tangential dipole moments, but the associated model is not as simple as for the radial sensors.

In this research we will therefore assume that the radial component is immeasurable and that only the two tangential components are measurable. Thus each submatrix G_p will be $m \times 2$, corresponding to the gain in the two tangential directions. We can refer to these two tangential components as ϕ and θ, e.g., $G_p = [G_\phi \ G_\theta]$. We emphasize that although we are using the dipole in a sphere model as an example, all results are sufficiently general such that extensions to other models containing all three moment components are straightforward, such as for the EEG model.

3.2.3 Unconstrained Location and Orientation

The *instantaneous state dipole* (Wood 1982) is the simplest of the dipole models, for which we consider just a single time slice of data, typically at the peak of the observed MEG response. The straightforward extension to the full temporal information is simply to treat each time slice with a separate static model. At each time slice, the locations and moments are calculated for each dipole, independently of all other time slices. Since no constraints are placed on the parameters of the dipole, this model allows both moving and rotating dipoles. The model is simply Equation (7) with a time parameter n inserted, $b(n) = G(n)q(n)$, which we would solve for each n, $n = 1, ..., n$.

3.2.4 Fixed Location, Unconstrained Orientation

When the instantaneous dipole model is solved for several sequential time points, the location of the dipole can appear to move as a function of time. Many researchers believe it is more realistic to assume that different parts of the cortex with different cortical function are activated electrically when they perform their specific tasks (George *et al.* 1989, Demunck 1990). The "movement" seen in the instantaneous state dipole would therefore be more accurately modeled as two or more stationary dipoles which are activating electrically at different times. Rather than allowing the dipole locations to vary with time, as in the above model, this second model restricts the location of the dipoles to be constant throughout the measurement interval, but allows the moment intensities and orientations to vary. We begin with the previous model, fix the gain matrix to be a constant with respect to time, and represent the model in a compact matrix form,

$$\left[b(1) \ ... \ b(n)\right] = G\left[q(1) \ ... \ q(n)\right] \tag{EQ 8}$$

or $B = GQ$. Each column of the Q matrix may be partitioned to represent the moments of p dipoles at time n,

$$q(n) = \begin{bmatrix} q_1(n) \\ \dots \\ q_p(n) \end{bmatrix} = \begin{bmatrix} m_1(n)s_1(n) \\ \dots \\ m_p(n)s_p(n) \end{bmatrix} \quad \text{(EQ 9)}$$

where each partition $q_p(n)$ can be represented by its unit moment orientation $m_p(n)$ and scalar intensity $s_p(n)$. Hence, each row of Q can represent the time series for one component of one tangential dipole (Scherg and von Cramon 1986).

3.2.5 Fixed Location and Orientation

Since no constraints are placed on the time series of the three components for each dipole, the orientation of the dipole can vary or "rotate" over time. Some researchers (Scherg and von Cramon 1985a, 1985b) argue that physiologically a dipole orientation should not rotate, because the dipole model represents a fixed neuroanatomical structure. If we fix the unit orientation of each moment to be the same for all time slices and allow only the magnitude and polarity, $s_p(n)$, of the moment to vary, then we can express the matrix Q from above as

$$Q = \begin{bmatrix} m_1 \begin{bmatrix} s_1(1) \dots s_1(n) \end{bmatrix} \\ \dots \\ m_p \begin{bmatrix} s_p(1) \dots s_p(n) \end{bmatrix} \end{bmatrix}$$

$$= \begin{bmatrix} m_1 & 0 \\ & \dots & \\ 0 & m_p \end{bmatrix} \begin{bmatrix} s_1(1) \dots s_1(n) \\ \dots \\ s_p(1) \dots s_p(n) \end{bmatrix} \quad \text{(EQ 10)}$$

$$= MS$$

22

Thus, our constrained model is now separated into three components,

$$
B = \begin{bmatrix} b_1(1) & \dots & b_1(n) \\ & \dots & \\ b_m(1) & \dots & b_m(n) \end{bmatrix} = GMS .
\tag{EQ 11}
$$

As before, G represents the $m \times p$ gain matrix between p unit dipoles and the array of m sensors. The $2p \times p$ block diagonal matrix M represents the fixed unit orientation moments. The moment intensity matrix S is $p \times n$.

Grouping as $B = (G\,M)\,S = A\,S$, we retain the same general separation into two matrices as for the other models. The difference here is that we have both the time invariant location l and moment orientation parameters M in the first matrix A, rather than just the location as before. Each column of G represents the gain of one *component* of one dipole, but each column of $A = [A_1, \dots, A_p] = G\,M$ now represents one *complete* dipole.

3.2.6 General MEG Model

The most general model contains both rotating and fixed dipoles. We might argue that two fixed dipoles may be so closely located that they appear in our data as one rotating dipole. We may also have rotating dipoles that rotate so little as to appear fixed in orientation. The general model accounts for both types and will be useful in deriving further results in this paper.

We simply alter our definition of a rotating dipole to be one which *must* rotate, such that its two component time series cannot be partitioned as a fixed moment orientation and a scalar time series (i.e., the time series are linearly independent). For p_r rotating dipoles and p_f fixed dipoles, we partition the pairs of rows of Q as the rank two

submatrix $Q_{rp} = [q_{\phi p} \; q_{\theta p}]^T$ for rotating dipoles and the rank one submatrix $Q_{fp} = [m_p \; s_p^T]$ for fixed:

$$Q = \begin{bmatrix} \begin{bmatrix} [q_{\phi 1} q_{\theta 1}]^T \\ \cdots \\ [q_{\phi p_r} q_{\theta p_r}]^T \end{bmatrix} \\ \begin{bmatrix} m_{(p_r+1)} s^T_{(p_r+1)} \\ \cdots \\ m_p s^T_p \end{bmatrix} \end{bmatrix} = \begin{bmatrix} I_{2p_r} & & & 0 \\ & m_{(p_r+1)} & & \\ & & \cdots & \\ 0 & & & m_p \end{bmatrix} \begin{bmatrix} \begin{bmatrix} [q_{\phi 1} q_{\theta 1}]^T \\ \cdots \\ [q_{\phi p_r} q_{\theta p_r}]^T \end{bmatrix} \\ \begin{bmatrix} s^T_{(p_r+1)} \\ \cdots \\ s^T_p \end{bmatrix} \end{bmatrix}, \qquad \text{(EQ 12)}$$

where s_p is the scalar amplitude over time for the pth fixed dipole, $q_{\phi p}$ is the scalar amplitude over time of the ϕ component of the pth dipole (likewise, θ), and I_{2pr} is a $2p_r \times 2p_r$ identity matrix. We can now express our model as $B = G\,Q = G\,(M\,S) = H\,S$, where $H = G\,M$ is our "hybrid" gain matrix, a combination of the previously defined G_p and A_p submatrices,

$$GM = H = [G_1, \ldots, G_{pr}, A_1, \ldots, A_{pf}] \, . \qquad \text{(EQ 13)}$$

The rank of this matrix H is $r = 2\,p_r + p_f$, which is effectively the number of *dipole source components* (Scherg and von Cramon 1986) in our model. The matrix S is the corresponding time series for *each* dipole component; if two dipole components are collocated, then by our definition they represent one rotating dipole.

The rotating and fixed models are just specializations of this model, and the instantaneous dipole model is just this model for one time slice. For no fixed dipoles ($p_f = 0$), M is simply a $2p_r \times 2p_r$ identity matrix, and we have the rotating dipole model of Equation (8), with $3p$ unknown location parameters in the gain matrix $H(l,M) = G(l)$. Similarly, for no rotating dipoles ($p_r = 0$), we have the fixed dipole model of Equation (11), with $4p$ unknown location and constrained unit moment parameters in the gain matrix $H(l,M) = A(l,M)$. As we will show in Chapter 5, successful localization

24

requires that we determine the rank r, i.e., the number of dipole components, but not necessarily the number of rotating and fixed dipoles.

3.3 EEG Model

One study completed in this research was a comparison of the lower bounds between MEG and EEG for effectively identical head models and array configurations. We present in this section research work performed by Michael E. Spencer.

The EEG dipole model is more complex than the MEG model, and assumptions must be made for the conductivities and shell thicknesses. The earliest models were for the dipole in a single homogeneous sphere (Wilson and Bayley 1950), which led to a closed form solution (Brody *et al.* 1973); however, this single sphere model is too simplistic because it does not model the relatively high resistivity of the skull layer. A three concentric sphere model that includes the scalp and skull layers was derived by (Arthur and Geselowitz 1970). The four sphere model, which also accounts for the cerebrospinal fluid layer, is derived by (Cuffin and Cohen 1979). Other models recently published include the three eccentric sphere model (Cuffin 1991) and the four sphere anisotropic model (Zhou and van Oosterom 1992).

In this research we use the four concentric sphere model. For a single dipole model at point $\vec{l}$, each element in (1) of the column vector of surface potential measurements represents the voltage at a single surface point $\vec{p}$ and is expressed as the inner product of the (3 x 1) gain vector $\vec{g}_v$ and the (3 x 1) dipole moment vector $\vec{q}$:

$$V(\vec{p}) = \vec{g}_v^T(\vec{l}, \vec{p})\vec{q} ,$$ (EQ 14)

where for clarity we show the dependence of the gain vector on both the dipole location and sensor position. The gain matrix $G(\vec{l})$ for a single dipole is the concatenation of the gain vectors for all sensor positions $\vec{p}$.

Fig. 5 shows the coordinate system used for the basic EEG formulas. For a dipole on the z-axis, the potential on the surface of the four sphere model referenced to infinity is given by (Cuffin and Cohen 1979). Other dipole locations are found by applying rotation transformations to the basic formulas. We can express the gain vector for the four sphere model for arbitrary dipole position $\vec{l}$ as

$$\vec{g}_V(\vec{l}, \vec{p}) = \sum_{n=1}^{\infty} w(n) \left(\frac{\|\vec{l}\|}{R}\right)^{n-1} \left[\vec{a}_{x'} P_n^1(\cos\theta') \cos\phi' + \vec{a}_{y'} P_n^1(\cos\theta') \sin\phi' + \vec{a}_{z'} n P_n(\cos\theta')\right] \quad \text{(EQ 15)}$$

where

$$P_n(\cdot) \quad = \quad \text{Legendre polynomial of order n,}$$

$$P_n^1(\cdot) \quad = \quad \text{Associated Legendre polynomial,}$$

$$R \quad = \quad \text{outside radius of head sphere (in m),}$$

$$\vec{a}_{x'}, \vec{a}_{y'}, \vec{a}_{z'} \quad = \quad \text{basis for rotated coordinate axes that place the dipole on the z'-axis, i.e. } 0 = \vec{a}_{x'} \cdot \vec{l}, \ 0 = \vec{a}_{y'} \cdot \vec{l}, \text{ and } \|\vec{l}\| = \vec{a}_{z'} \cdot \vec{l},$$

$$\theta', \phi' \quad = \quad \text{polar coordinates of } \vec{p} \text{ in the rotated system (Fig. 5).}$$

The weighting function $w(n)$ in (15) is given by

$$w(n) = \left(\frac{1}{4\pi\gamma_4 R^2}\right) \frac{(2n+1)^4 (cd)^{2n+1}}{n\Gamma(n)} \quad \text{(EQ 16)}$$

where

$$\Gamma(n) = d^{2n+1} \{b^{2n+1} n(k_1-1)(k_2-1)(n+1) + c^{2n+1}(k_1 n+n+1)(k_2 n+n+1)\}$$
$$\cdot \{(k_3 n+n+1) + (n+1)(k_3-1)d^{2n+1}\}$$
$$+ (n+1)c^{2n+1}\{b^{2n+1}(k_1-1)(k_2 n+k_2+n) + c^{2n+1}(k_1 n+n+1)(k_2-1)\}$$
$$\cdot \{n(k_3-1) + (k_3 n+k_3+n)d^{2n+1}\} \quad \text{(EQ 17)}$$

$$k_1 = \frac{\gamma_1}{\gamma_2}, \quad k_2 = \frac{\gamma_2}{\gamma_3}, \quad k_3 = \frac{\gamma_3}{\gamma_4}, \quad \text{(EQ 18)}$$

26
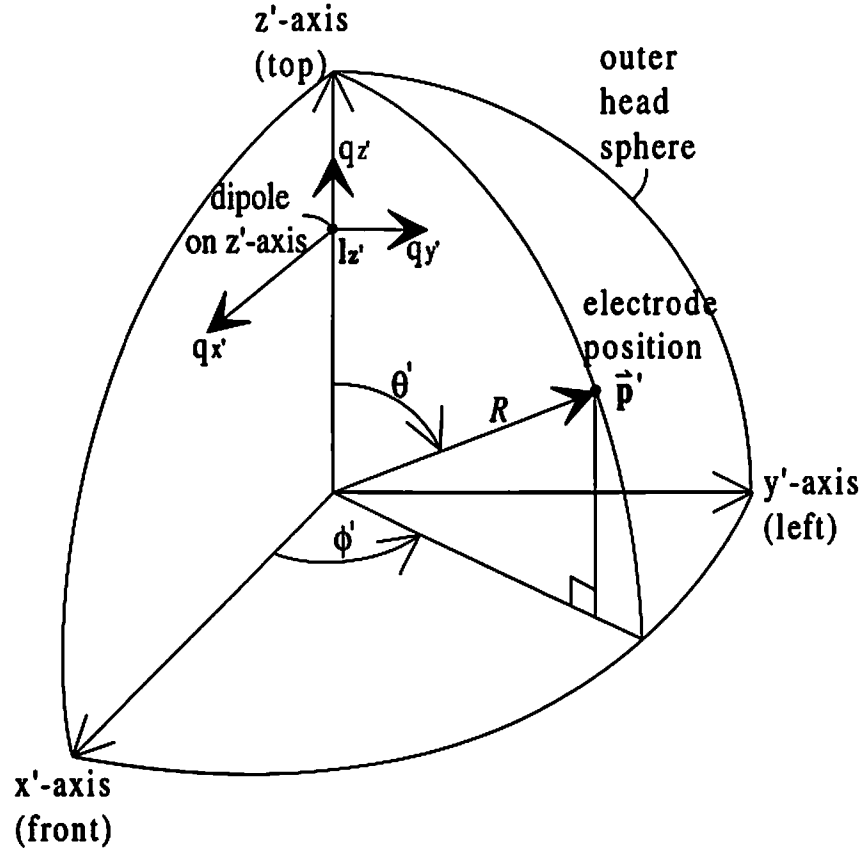
FIGURE 5. EEG Coordinate system for dipole on z-axis in a spherical head model. The EEG model generalizes to an arbitrary dipole location using standard coordinate transformations.

and γ_1, γ_2, γ_3, γ_4 are the conductivities of brain, cerebrospinal fluid, skull, and scalp, respectively, and b, c, d are the inner sphere radii normalized to the outer head sphere radius. Fig. 6 shows the four spheres with their respective radii and conductivities. Overlaid on the spheres are the sensor locations for the 37 channel pattern (one of the sensor arrays analyzed in this dissertation).

The formula for this EEG model explicitly shows that the voltage has a nonlinear dependence on the dipole and electrode locations and a linear dependence on the dipole moment. The conductivities and radii shown were taken from (Cuffin and Cohen 1979). We note that the relatively thin skull thickness, 4 mm in this case, gives favorable values
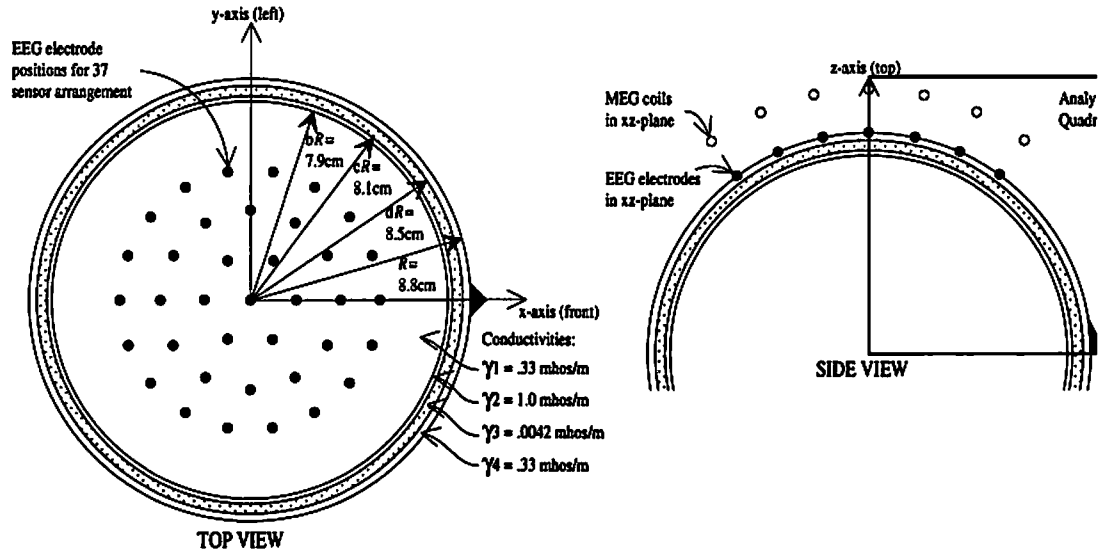
FIGURE 6. Four concentric sphere model of head (Cuffin and Cohen 1979). The radii and conductivities are shown for the inner brain sphere, the cerebrospinal fluid layer, the skull layer (shaded), and the scalp layer. The EEG electrodes are located on the surface of the scalp at a radius of 8.8 cm; MEG coils are radially oriented 10.5 cm from the head center. For the 37-sensor case, the sensors are positioned in rings of 1, 6, 12, and 18 sensors each, separated by 12 degrees as measured from the z axis. The left figure shows the sensors as viewed from above. The right figure is the side view and shows the EEG electrodes and the MEG coils that lie in the xz-plane (y=0) for the 37-sensor arrangements. The analysis quadrant shows where the CRLB bounds are computed relative to the head spheres and sensors.

for dipole localization; thicker skulls will produce higher error bounds. For example, (Stok 1987), uses a skull thickness of 6 mm.

3.4 Thunderstorm Model

In this section, we review the basic thunderstorm model. In the simple form examined in this dissertation, the model is very similar in form to the simple current dipole model of MEG and EEG research.

The contour map presently generated at KSC is implicitly based on a point charge model, albeit 31 charges in a fixed pattern about the Cape. These contour patterns generated are still subject to quite a degree of interpretation, and the patterns vary significantly in the presence of minor fluctuations. In this section, we introduce a much

28

simpler and more readily interpreted model. The thunderstorm model used in this study is intentionally simplistic, so that the processing methods used to solve the model are not lost in the complexity of the parameters. Success with simple models will allow careful building of more sophisticated and hopefully more accurate models.

The model used here is the point charge model. Any complex distribution of static charges can be simplified to a point charge if viewed from a distance relatively large compared to the diameter of the charge distribution (Feynman 1962). We assume a point charge source of intensity Q coulombs located at position (x_q, y_q, z_q). The observer position is on the ground at position $(x, y, 0)$. We use the sign convention that a positive electric field indicates that a positive charge would move upwards (i.e., the negative of the potential gradient). In weather related terms, our sign convention is "fair weather negative." Representing the earth as a perfect ground plane, the electric field at the surface has only a nonzero vertical component:

$$E = \frac{-Qz_q}{2\pi\varepsilon \left((x-x_q)^2 + (y-y_q)^2 + z_q^2 \right)^{3/2}}$$
(EQ 19)

where ε is the permittivity of the medium, here assumed to be free space.

The above formula is for a single charge and a single sensor. The extension to multiple charges and sensors follow directly that of the MEG formulation. We can thus arrange our data into a spatiotemporal matrix as:

$$E = [e(t_1), ..., e(t_n)] = G[q(t_1), ..., q(t_n)] = GQ .$$
(EQ 20)

Thus the vector e represents the electric field signal at a single time instance due to p sources. Over a fixed interval of time, we acquire n such vectors of data. We observe that this data is changing as a function of time, and we therefore need a time dependent parameter. The sampling interval of 60 samples/second is relatively fast compared to the ground speed of the thunderstorm, and we will process the data in relatively short time

segments. During these intervals, we can approximate the position of the storm as relatively fixed in space and assume that only the intensity Q is changing as a function of time.

Chapter 4

Least Squares Solution

In this chapter, we show how a least squares error is generated by implicitly or explicitly projecting the measurements onto the orthogonal complement of the subspace formed from the appropriate forward model. We use the dipole in a sphere model as an illustration, where the nonlinear parameters are the locations of the dipoles and possibly the fixed orientation. The cost function is shown to be a function of these nonlinear parameters only, thus reducing the number of parameters to be searched. The nonlinear parameters are iteratively adjusted to minimize this error through standard nonlinear minimization techniques. The optimal nonlinear parameter set is then used to perform a linear least squares fit for the linear parameters. We present approaches for efficiently calculating these cost functions, then conclude with a three dipole simulation example.

4.1 Error Function

4.1.1 Separation of Linear Parameters

Consider the general model of p_r rotating dipoles and p_f fixed dipoles for our data, $B = H(l, M) \, S$, where $H(l, M)$ is $m \times r$, S is $r \times n$, and $r = 2 \, p_r + p_f$. $H(l, M)$ has $3p$ unknown location parameters and p_f unknown constrained moment parameters. We collect n time samples from each of m SQUID biomagnetometers and form a spatio-temporal matrix of data $F = [f(1), \ldots, f(n)]$. We model this data as $F - B = N$, where N

represents the error between the measurements and our model. We define our measure of fit as the square of the Frobenius norm,

$$J_{LS} = \sum_{i=1}^{m} \sum_{j=1}^{n} \{f_i(j) - b_i(j)\}^2 = \|F - B\|_F^2$$

$$= \|F - H(l, M)S\|_F^2$$

(EQ 21)

The goal is to find the set $\{l, M, S\}$ that minimizes this error.

The simple approach is to use this cost function directly in an iterative minimization algorithm, which would search for all five parameters for each one of p dipoles at each point of n time instances, for an overall total of $5pn$ parameters (Romani and Leoni 1984). Thus a three dipole model would require searching a fifteen parameter space at every time instance. This same cost function, however, can be viewed as a projection minimization that can greatly reduce the computational cost, yet incorporates the information of all the time slices.

Given l and M (hence, H), a solution for the matrix S that will minimize J_{LS} is

$$S = H^\dagger F,$$

(EQ 22)

where $H^\dagger$ is the well-known pseudoinverse solution (for full column rank H),

$$H^\dagger = (H^T H)^{-1} H^T,$$

(EQ 23)

or the more general Moore-Penrose pseudoinverse (minimum norm) solution,

$$H^\dagger = V \Sigma^+ U^T,$$

(EQ 24)

where $H = U \Sigma V^T$ is a singular value decomposition (SVD) and Σ^+ is the diagonal matrix Σ with its nonzero elements inverted (Golub and van Loan 1983). This minimization for S will hold for all sets $\{l, M\}$, including the optimal set $\{l, M\}^*$ that minimizes the cost function J_{LS}.

We can replace S with this pseudoinverse solution before solving for $\{l, M\}$. The cost function can be equivalently expressed as

$$J_{LS} = \| F - HS \|^2 = \| F - H(H^\dagger F) \|^2 = \| (I - HH^\dagger) F \|^2 = \left\| P_H^\perp F \right\|^2. \qquad \text{(EQ 25)}$$

The matrix $P_H^\perp$ and its orthogonal complement P_H are *projection* matrices: P_H projects data onto the column space of the matrix H, and $P_H^\perp$ is the orthogonal complement projection, that is, the projection of the data onto the left null space of H. Thus, the squared error can be explicitly computed as the projection of the data matrix, F, onto the left null space.

We have used the separation of the unknown parameters into linear and non-linear components and have factored out the linear moments. While this method has often been used by other MEG researchers (Scherg 1989, Maier *et al.* 1987, Achim *et al.* 1988, Demunck 1990), the mathematical details have not always been stated or explained explicitly; references (Golub and Pereyra 1973, Guttman and Pereyra 1973) give a full mathematical justification for this approach. The benefit is that J_{LS} is now an explicit function of only the parameters in H. An iterative minimization routine need only explicitly consider this reduced subset of parameters, which can considerably reduce the convergence time.

This cost function can be minimized directly by a non gradient-based method, such as the Nelder-Meade simplex, used by many researchers because of its simplicity and apparent robustness to local minima (Achim *et al.* 1988). Alternatively, gradient-based methods are typically faster, but require either analytical or numerical partial derivatives of the projection matrix. Simple analytic expressions of the partials of the projection matrix are derived in (Golub and Pereyra 1973, Guttman and Pereyra 1973), and these expressions, in turn, require only partials of the gain matrix H. In practice, however, any slight change in the head or source model requires a recalculation of the

partials, and the simplex method or other non gradient methods are therefore usually preferred for their simplicity (Maier *et al.* 1987, Achim *et al.* 1988).

The computational complexity of the least-squares estimation problem is highly dependent on the number of nonlinear parameters that must be estimated. In the instantaneous state dipole model, the location of each dipole must be computed independently for each time slice n. In comparison, the number of nonlinear parameters in the rotating dipole model drops dramatically. For p dipoles and n time slices, in both cases we have $2pn$ linear parameters, but the gain matrix G is a function of only $3p$ location parameters for the rotating dipole model, rather than $3pn$ for the instantaneous dipole model. Thus the rotating dipole model requires an iterative search of only the $3p$ non-linear location parameters, followed by a simple $2pn$ linear fit for the moment parameters. For the fixed dipole model, the dimensionality of the search space in the iterative minimization algorithm is increased relative to the rotating dipole model from $3p$ parameters (locations only) to $4p$ parameters (locations and constrained unit orientations). Only the pn parameters of the time-series magnitude and polarity of the moments in the matrix S can be calculated using a simple linear fit.

An approximate approach to the fixed dipole model is to group the model as $B = G(M S)$, which is effectively identical to the rotating dipole model $B = G Q$. Once Q is found, we form a second equation, $M S = Q$, from Equation (10), and solve for M and S. The advantage of this approach is that $M S = Q$ can be solved efficiently using the SVD. Each set of two rows of Q represents the time series for the two tangential components of one dipole. If the dipole is truly fixed in orientation, then this $2 \times n$ matrix partition is of rank one. An SVD of this partition of the matrix will give the best rank one fit, and a simple analysis of the singular values will confirm the quality of this fit. If the rank one fit from the SVD is perfect, then the solution is optimal; however, in general this approximate approach is not guaranteed to give the same result as that which would be obtained

34

by solving $B = A\ S$. The appeal lies in keeping only $3p$ unconstrained parameters instead of $4p$ constrained parameters in the iterative search space. An example of this method is shown in Section 4.2. One possible extension of this approach may be to embed this two-step process into each iterative error calculation, rather than solving $M\ S = Q$ only once at the end of the iterations.

4.1.2 Error Function Computation

The greatest computational burden in fitting the multiple dipole model occurs in the iterative nonlinear minimization routine, which must repeatedly form the nonlinear gain matrix H, then solve the inverse matrix problem for cost function J_{LS} for different sets of parameters. By using the SVD and the QR decomposition (Golub and van Loan 1983), we can significantly reduce the number of multiplications required. This analysis also leads naturally into Chapter 5, where we present an alternative method of solving the least-squares problem using these same decompositions.

If the number of time samples, n, is greater than the number of sensors, m, then the use of an SVD of F gives an efficient form for calculating the above error function. Decomposing as $F = U\ \Sigma\ V^T$, the least-squares cost function can be rewritten as

$$J_{LS} = \left\| P_H^{\perp} F \right\|_F^2 = \left\| P_H^{\perp} U \Sigma V^T \right\|_F^2 = \left\| P_H^{\perp} U \Sigma \right\|_F^2 = \left\| P_H^{\perp} W \right\|_F^2 , \qquad \text{(EQ 26)}$$

where we are able to drop the term V^T because orthogonal matrices preserve the F-norm. Since F is $m \times n$, then the diagonal matrix Σ of singular values has at most m nonzero terms. Therefore $W = U\Sigma$ is only $m \times m$, as opposed to the larger $m \times n$ data matrix F.

Greater savings occur if the number of non-zero singular terms, r, is less than m, i.e., F is not of full row rank, because then W would have correspondingly fewer columns, r. With noise considerations, the singular values are almost always strictly greater than zero, so we can amend r to be the number of singular terms "significantly"

greater than zero. The corresponding r components in the decomposition are the *principal components* that "adequately" describe the data, where the user must decide what is adequate and what is significant. Using these significant components reduces the computational cost but results in a suboptimal least-squares solution. Chapter 5 more fully exploits this possible decomposition. A two-stage approach would be to use this reduced r set for the coarse fit, then return to the full m set of components for the complete fit.

If an SVD is used to calculate the pseudoinverse of H, then a further reduction in the number of multiplications can occur. Denoting the decomposition as

$H = \begin{bmatrix} U_r \bar{U}_r \end{bmatrix} \Sigma V^T$, where H is $m \times r$, then let U_r contain the columns corresponding to the r non-zero singular values, and let $\bar{U}_r$ correspond to the m-r *zero* singular values, where r is the rank of H. Then $P_H^\perp = \bar{U}_r \bar{U}_r^T$, and the cost function can be calculated as

$$ J_{LS} = \left\| P_H^\perp W \right\|_F^2 = \left\| \bar{U}_r^T W \right\|_F^2 = \| W \|_F^2 - \left\| P_H W \right\|_F^2 = \| W \|_F^2 - \left\| U_r^T W \right\|_F^2 \quad \text{(EQ 27)} $$

where the second form follows from the well-known equality for the Frobenius norm

$$ \| W \|_F^2 = \left\| P_H W \right\|_F^2 + \left\| P_H^\perp W \right\|_F^2. $$

The selection between the two forms depends on the rank r and the decomposition method used, since either projection matrix may also be efficiently computed by using the QR decomposition of the gain matrix H. The choice of SVD or QR decomposition is application dependent. In general, the calculation of an SVD is more expensive, because it calculates the two eigenvector spaces U and V by iteratively converging to a solution. However, "economy" SVD versions (Dongarra 1979, Mathworks 1990) can be run in which only the principal component eigenvectors are calculated, i.e., those in U_r above, resulting in considerable savings if the rank r of H is small relative to m. By comparison, QR decomposition is noniterative, and it outperforms a full SVD calculation. If the rank of H is large, then QR decomposition generally outperforms even the

36

economy SVD. Either method of decomposing H will outperform the undecomposed projection matrix, $P_H = H\,H^\dagger$. These decomposition approaches also have better numerical properties than inverting $(H^T H)$ or solving via Gaussian elimination (Golub and van Loan 1983).

4.2 MEG Simulation

We conclude this chapter by presenting the results of simulations in which the spatio-temporal models described are applied to a set of simulated MEG data. Data were simulated for the case of three dipoles, all three with fixed locations, two with fixed moment orientations and the third with a rotating orientation. The data were computed for an array of 37 closely spaced sensors radially oriented and positioned on the surface of an imaginary sphere of radius 12 cm.

Because the head model was assumed to be a spherically symmetric conductor and the sensors were arranged radially outside of the sphere, then only the fields due to the primary tangential dipole currents were computed, as discussed in Chapter 3. However, rather than compute the parameters in a spherical or rotated coordinate system, we employ a Cartesian coordinate system and solve for the three constrained moment parameters per dipole, using the pseudoinverse form of Equation (24). A total of 100 time samples were generated and corrupted by additive white Gaussian noise with an SNR of 10dB. SNR is computed as the ratio of the average magnetic field measurement power to the variance of the noise. The resulting simulated MEG data are shown in Fig. 7.

The parameters for this data were estimated using two of the models discussed: a) fixed location but unconstrained orientation; and b) fixed location and orientation. For the "rotating" model, the locations of the three dipoles were estimated using a Nelder-Meade simplex search to minimize J_{LS} in Equation (25) over the dipole location param-
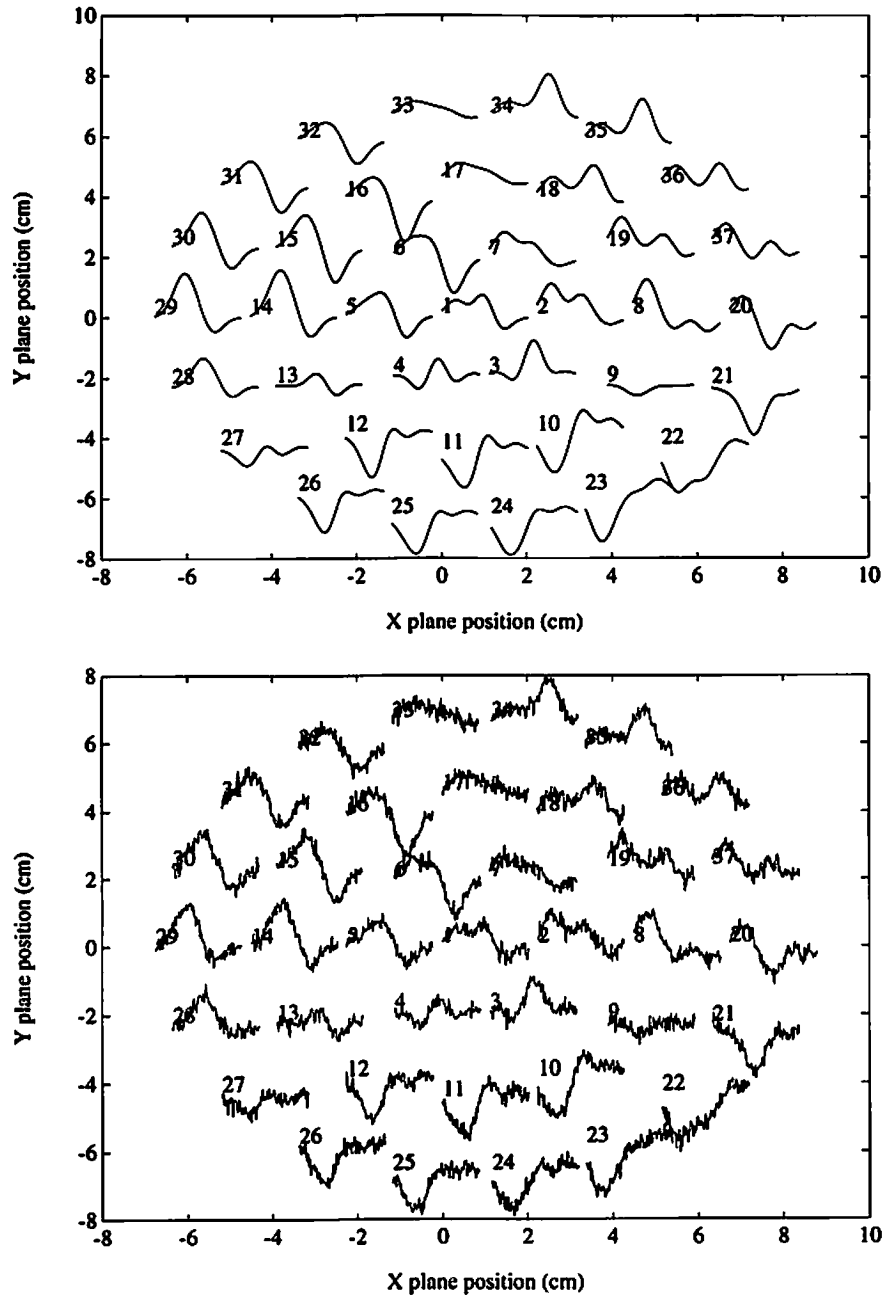
FIGURE 7. Simulated MEG data for 37 radially oriented sensors, 100 time samples from each. Sensors are positioned on an imaginary sphere of radius 12 cm, centered on the origin, with Sensor 1 located 12 cm above the(x,y) plane at (x,y,z) position $(0,0,12)$. Three dipoles were simulated about 3 cm radially below the sensors numbered 9, 13, and 17. Zero-mean Gaussian noise with a standard deviation equal to one-tenth the peak was added, for an SNR of approximately 10 dB. Each numbered trace represents the time response for the corresponding sensor, with the plots arranged in their approximate spatial position in the (x,y) plane.

38

eters; Equation (22) was then used to find the moment time series. The true and esti-mated locations are listed in Table 1 and the estimated time series are shown in Fig. 8 overlaid with the original simulated time series.

TABLE 1. Estimated Locations and Moments. The locations were found using a Nelder-Meade simplex algorithm for the rotating dipole model. The number of dipoles, 3, was assumed known, and the simplex algorithm searched for the best 9 location parameters that fit the data in a least-squares sense. Once the locations were optimized, the time series were found via a simple linear least-squares fit. The time series for the second and third dipoles were decomposed into a rank 1 model, from which the fixed moment orientations were found

	Dipole 1			Dipole 2			Dipole 3		
	True and Estimated Locations (cm)								
	l_x	l_y	l_z	l_x	l_y	l_z	l_x	l_y	l_z
True	2.800	-1.700	8.300	-2.900	-1.600	8.300	0.000	3.300	8.400
Estimated	2.817	-1.691	8.335	-2.910	-1.594	8.225	-0.056	3.320	8.358
	True and Estimated Moments (from SVD)								
	m_x	m_y	m_z	m_x	m_y	m_z	m_x	m_y	m_z
True	(N/A, rotating)			0.770	0.525	0.369	0.516	-0.797	0.313
Estimated				0.770	0.518	0.373	0.507	-0.800	0.320

For the fixed orientation and location model, rather than iteratively search for dipole locations *and* orientations, we used the two-step approximate method discussed in Section 4.1.1. In this method, we use the results of the rotating model above, which searched the nine parameter location space only. The identified time series were then fit to a rank one model (per dipole) via an SVD, resulting in the time series displayed in Fig. 8. The true and identified moments for the two fixed dipoles are displayed in Table 1. Because the third dipole actually had a rotating moment, then the SVD of its time series properly revealed a poor rank one fit.
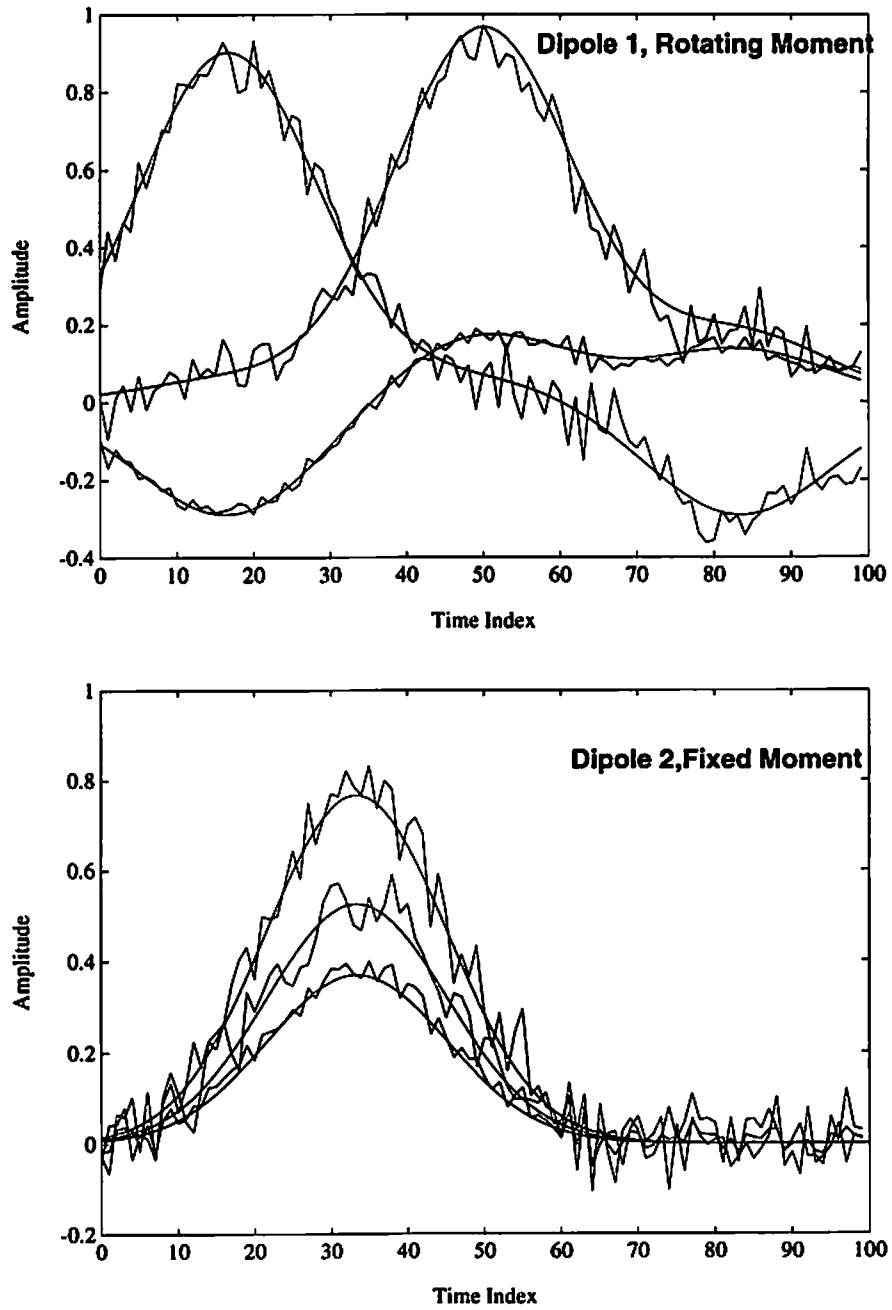
FIGURE 8. Estimated moment time series for three dipoles. Three dipoles of tangential orientation (no radial component) were given overlapping time series and projected into Cartesian coordinates, one time series per coordinate per dipole. The dipole model for the unconstrained moment orientation was then used in a simplex algorithm to find the locations.

40
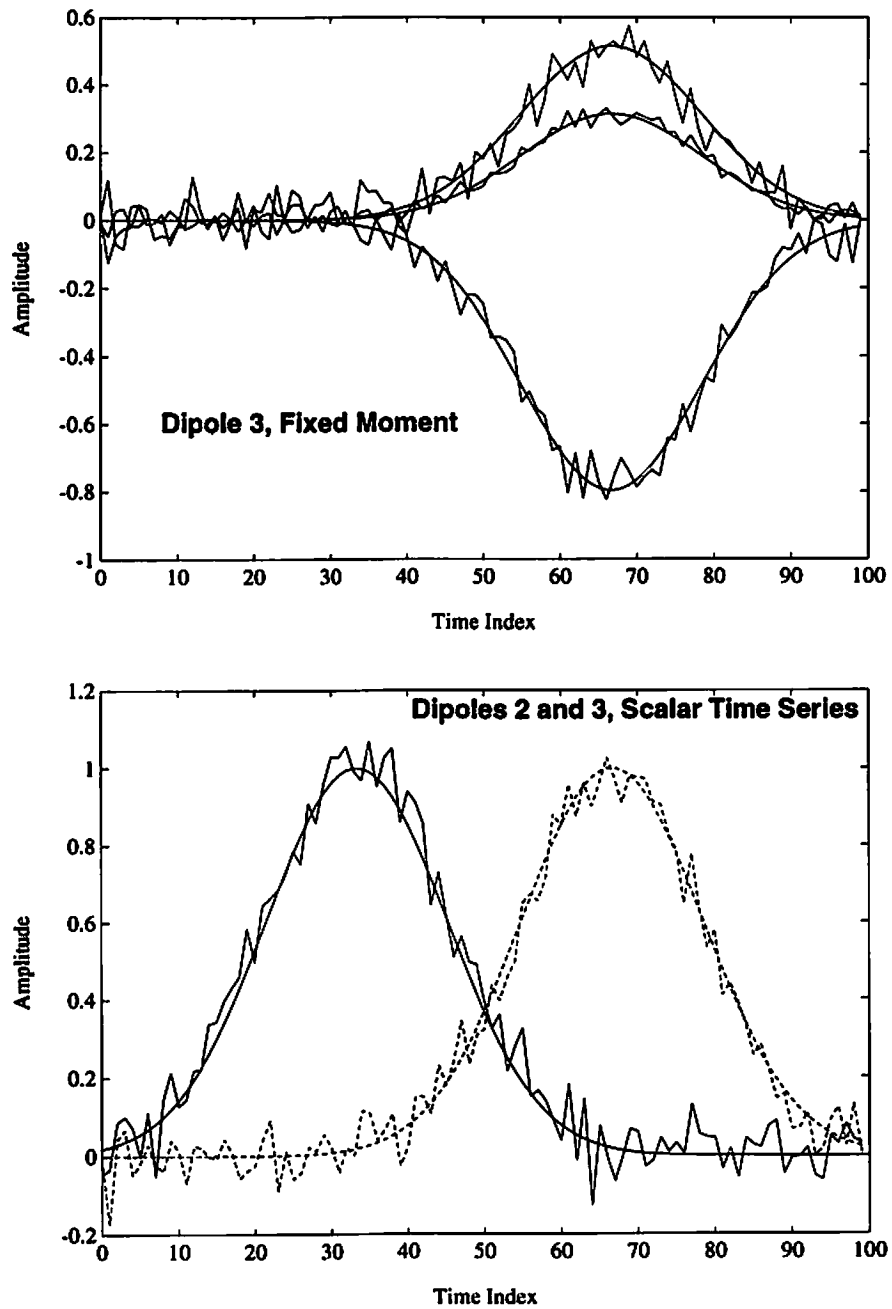
(Fig. 8 continued) The nine time series were found with a simple least-squares fit and plotted for each of the three components of the three dipoles in figures (a) to (c). An SVD was then performed on the second and third dipole time series ((b) and (c)) to approximate the dipole model for constrained orientations, and the resulting dipole moment magnitude and polarity is plotted in (d).

41

Chapter 5

MUSIC

In this chapter we introduce a new MEG inverse algorithm. Although it is generally suboptimal in a least-squares sense, this algorithm has the strong advantage of "scanning" quickly with a *one* dipole search, rather than the p-dipole search necessary in a complete fit. In Section 5.2.4, we discuss how this algorithm is analogous to the statistically derived MUSIC direction-finding algorithm for polarized sources (Schmidt 1986). Section 5.4.2 examines the related method of PCA dipole fitting, but shows where this method differs and why it generally fails. We first develop the algorithm for the rotating dipole, then extend it to include the fixed dipole model. We then consider the general hybrid case of both fixed and rotating dipoles.

5.1 Order Selection

Perhaps one of the greatest problems in MEG analysis is determining the number of dipoles: if too few are selected for any of the models, then the calculated dipoles are biased by the missing dipoles; if too many dipoles are specified, then spurious dipoles are introduced, which may be indiscernible from the true dipoles. Since the computational cost and numerical sensitivity of most iterative minimizations increases dramatically with the number of parameters, then too many dipoles also adds needless computational burden.

Other authors have shown that examination of the spatial surface topography can be misleading if time series are overlapping and/or dipoles are placed such that one maximum potential cancels another (Achim *et al.* 1988, Nunez 1986). As an alternative,

analysis of the dimensionality or rank of the data matrix F is often made in an attempt to determine the true number of dipoles. In general, for p dipoles, the rank of the model data matrix B will be limited by

$$\text{Rank}(B) = \min(\text{Rank}(H), \text{Rank}(S)) \leq 2p .\tag{EQ 28}$$

The upper limit comes from either H or S, since each dipole moment component in S has a corresponding column in H, with at most two moment components per dipole. For the lower limit, the problems usually arise in S, where the matrix is of full row rank only if all time series are linearly independent. If all dipoles are rotating, then S is at most rank p; however, if all dipoles are fixed in orientation, then S is at most rank p. If any combination of the spatially distinct dipoles have linearly dependent time series (perfectly correlated), then the rank of S drops accordingly.

For the general model with p_r rotating and p_f fixed dipoles, the rank of H is $r = 2pr + pf$. As we will show, we do not explicitly need to know p_r and p_f, if the time series are sufficiently independent and the SNR sufficiently large.

5.2 Dipole Models

5.2.1 Rotating Dipole Model

We consider first the case where all dipoles rotate, that is $H(l, M) = G(l) M = G(l)$. From Equation (25), we express the least-squares cost function as

$$J_{LS} = \| F - G\,Q \|^2 = \| P_G^{\perp}\,F \|^2 \tag{EQ 29}$$

where G is $m \times 2p$, Q is $2p \times n$, and M is the identity matrix, since all dipoles are assumed rotating. We can interpret the least-squares problem as trying to find the gain matrix G whose orthogonal subspace projector $P_G^{\perp}$ minimizes J_{LS}. Since G is of rank $2p$, then the orthogonal complement projector $P_G^{\perp}$ is of rank $m - 2p$.

43

In the method developed here, we first find the best orthogonal projector $P^\perp$, regardless of the gain matrix, and then find the gain matrix G that best fits this projector. The first step in this method is to minimize over all possible orthogonal projectors of rank $m - 2p$, for which we form the first cost function,

$$J_1 = \| P^\perp F \|^2 . \tag{EQ 30}$$

Minimizing J_1 over all $P^\perp$ is equivalent to finding the best rank $2p$ projections of F. From (Golub and van Loan 1989, Corollary 2.3), the best rank $2p$ approximation of F is formed from the first $2p$ components of the SVD. Hence, we decompose F as

$F = U\Sigma V^T = \begin{bmatrix} U_{2p} \tilde{U}_{2p} \end{bmatrix} \Sigma V^T$, where U_{2p} contains the $2p$ left singular vectors associated with the $2p$ largest singular values, and $\tilde{U}_{2p}$ contains the remaining m-$2p$ left singular vectors. The best rank $2p$ approximation of F is given then by $F_{2p} = \begin{bmatrix} U_{2p} U_{2p}^T \end{bmatrix} F$. The best orthogonal projector is therefore

$$P^\perp = \tilde{U}_{2p} \tilde{U}_{2p}^T \tag{EQ 31}$$

Once we have formed this best orthogonal projector $P^\perp$, then the second step is to find the gain matrix G most orthogonal to this projector. Orthogonality between $P^\perp$ and $G = [G_1, \dots, G_p]$ implies $P^\perp$ is orthogonal to each G_p, where G_p is the $m \times 2$ gain matrix for a single dipole. Since the pth matrix depends only on the location of the pth dipole, our scanning function for rotating dipoles, $J_r(p)$, is derived from this orthogonality,

$$J_r(p) = \frac{\left\| P^\perp G_p \right\|_F^2}{\left\| G_p \right\|_F^2} = \left\| \tilde{U}_{2p}^T \bar{G}_p \right\|_F^2 \tag{EQ 32}$$

where $\bar{G}_p = G_p / \left\| G_p \right\|_F^2$ is the normalized gain matrix. Normalization is necessary so that a small value for $J_r(p)$ is an indication of closeness to orthogonality and is not simply due to a relatively small gain.

If $P^\perp$ is a reasonable approximation to the optimal $P_G^\perp$, and a G exists such that $\|P^\perp G\|_F^2 \approx 0$, then each of the G_p submatrices will be orthogonal to $P^\perp$, and $J_r(p) \approx 0$ when evaluated for each correct location (the conditions under which these approximations hold true will be discussed in Section 5.2.4. Our scanning method therefore is to search over all possible *one*-dipole locations and at each location evaluate $J_r(p)$, looking for minima. The explicit steps will be presented in Section 5.3. The general approach is to evaluate $J_r(p)$ over a fine three-dimensional grid, plot its *inverse*, and look for p sharp "spikes".

Provided the gain matrices are linearly independent over the scanning space, the scanning function will not display more than p spikes, since the existence of more, for instance $p + 1$ spikes, would suggest there are $m + 2$ orthogonal column vectors in an m-dimensional space, which is not possible. We may however find fewer than p spikes. Each evaluation of $J_r(p)$ actually represents the projection of the column vectors for *two* tangential components in G_p. If the dipole is *fixed* in orientation, then only a linear combination of the two vectors may be orthogonal, and $J_r(p)$ would not necessarily be a minimum at the dipole location. The next section extends this scanning method to accommodate these fixed orientation dipoles.

5.2.2 Fixed Orientation Dipoles

We now assume all dipoles are fixed, such that our model for the fixed orientation dipole, as shown in Equation (11), is $B = [G(l) \, M] \, S = A(l, M) \, S$, where S is the scalar time series and M is the matrix of fixed unit orientation moments. The gain matrix G is still $m \times 2p$, but M is $2p \times p$ and S is $p \times n$, where p is the number of dipoles. Thus, $A(l, M)$ is an $m \times p$ matrix and the full least-squares cost function is

$$J_{LS} = \min_A \|P_A^\perp F\|_F^2, \text{ where } P_A^\perp \text{ is an orthogonal projector onto an } m\text{-}p \text{ subspace, rather}$$

than an m-$2p$ subspace as for $P_G^\perp$. We otherwise proceed identically as above, arriving at an analogous cost function for a fixed dipole,

$$J_f(p) = \frac{\left\| \tilde{U}_p^T A_p \right\|_2^2}{\left\| A_p \right\|_2^2} = \left\| \tilde{U}_p^T \bar{A}_p \right\|_2^2 \qquad \text{(EQ 33)}$$

where $\bar{A}_p = A_p / \left\| A_p \right\|_2^2$ is the normalized gain matrix for fixed dipoles, $\tilde{U}_p$ now contains the m-p left singular vectors associated with the m-p smallest singular values, and we note that for the vector A the L_2 norm is equivalent to the Froebinius norm.

Note that $J_f(p)$ is now a function of four parameters. If $J_f(p)$ were evaluated in the same manner as the rotating dipole scanning function, then not only would we need to scan over all possible locations l_p, but at each location we would also have to scan over all possible constrained unit orientations m, thus extending our scan from three dimensions to four dimensions. However, we now show that we can instead continue to search over only the three-dimensional locations l_p and at each location implicitly select the *best* orientation m which minimizes our cost function. We achieve this by using the separability of $A_p = G_p m_p$ and applying the constraint $m_p^T m = 1$, since m_p is, by our definition, a unit moment orientation vector.

For a given three-dimensional location l_p, $G_p(l_p)$ is completely specified, so we seek to minimize the cost function $J_f(p)$ with respect to m_p,

$$J_f(p) = \frac{\left\| \tilde{U}_p^T A_p \right\|_2^2}{\left\| A_p \right\|_2^2} \qquad \text{(EQ 34)}$$

$$= \frac{\left\| \tilde{U}_p^T G_p m_p \right\|_2^2}{\left\| G_p m_p \right\|_2^2} \qquad \text{(EQ 35)}$$

$$= \frac{m_p^T G_p^T P^\perp G_p m_p}{m_p^T G_p^T G_p m_p} \qquad \text{(EQ 36)}$$

subject to $m_p^T m = 1$.

From Equation (36) we recognize that minimizing this problem is equivalent to finding the minimum *generalized eigenvalue* (e.g., (Strang 1980), Page 277, (Golub and van Loan 1989), Page 470) of the expression

$$G_p^T P^\perp G_p m_p = \lambda G_p^T G_p m_p \qquad \text{(EQ 37)}$$

If we denote the SVD of G_p as $G_p = U_{Gp} \Sigma_{Gp} V_{Gp}^T$, where U_{Gp} contains only the principal eigenvectors associated with the non-zero singular values, then the generalized eigenvalue problem can be expressed as

$$\left[V_{Gp} \Sigma_{Gp} U_{Gp}^T \right] P^\perp \left[U_{Gp} \Sigma_{Gp} V_{Gp}^T \right] m_p = \lambda \left[V_{Gp} \Sigma_{Gp} U_{Gp}^T \right] \left[U_{Gp} \Sigma_{Gp} V_{Gp}^T \right] m_p . \qquad \text{(EQ 38)}$$

By pre-multiplying both sides by $\Sigma_{Gp}^{-1} V_{Gp}^T$, we can simplify to

$$U_{Gp}^T P^\perp U_{Gp} \left[\Sigma_{Gp} V_{Gp}^T m_p \right] = \lambda \left[\Sigma_{Gp} V_{Gp}^T \right] m_p \qquad \text{(EQ 39)}$$

so that we can now solve the equivalent simpler minimum eigenvalue problem,

$$J_f(p) = \lambda_{\min} \{ U_{Gp}^T P^\perp U_{Gp} \} \qquad \text{(EQ 40)}$$

where $\lambda_{\min} \{ \ \}$ denotes the minimum eigenvalue of the bracketed term.

Thus we need not explicitly scan for or calculate the best moment orientation that minimizes $J_f(p)$, but rather calculate just the eigenvalue associated with this moment. Consequently, the fixed dipole scanning procedure is the same as for the rotating model, except that at each location in our 3-D scanning grid we calculate the smallest eigenvalue of the bracketed term. For the fixed p-dipole model we expect to find p locations where $J_f(p) \approx 0$. The optimal moment orientation at each minimum of $J_f(p)$ is found indirectly as the eigenvector associated with minimum eigenvector.

Note that calculating this cost function requires finding the smallest eigenvalue of only a 2×2 matrix. Also note that depending on the dimension p of the orthogonal projector, this small 2×2 matrix may be more efficiently formed as

$$U_{Gp}^T (I - U_p U_p^T) U_{Gp} = I - (U_p^T U_{Gp})^T (U_p^T U_{Gp}), \qquad \text{(EQ 41)}$$

where U_p again represents the p left singular vectors associated with the p largest singular values of F. Thus, this cost function may be calculated with relatively little computational burden.

5.2.3 Fixed and Rotating Dipoles

In the mixed case, we have p_r rotating dipoles and p_f fixed dipoles for a total of $p = p_r + p_f$ dipoles. Our general model is therefore

$$B = HS = \begin{bmatrix} G_{\phi 1} & G_{\theta 1} \end{bmatrix} \cdots \begin{bmatrix} G_{\phi pr} & G_{\theta pr} \end{bmatrix} A_1 \cdots A_{pf} \begin{bmatrix} \begin{bmatrix} q_{\phi 1} & q_{\theta 1} \end{bmatrix}^T \\ \cdots \\ \begin{bmatrix} q_{\phi pr} & q_{\theta pr} \end{bmatrix}^T \\ s_1^T \\ \cdots \\ s_{pf}^T \end{bmatrix} \qquad \text{(EQ 42)}$$

We have two related scanning functions for rotating and fixed dipoles, $J_r(p)$ and $J_f(p)$. Examining $J_r(p)$, we see that

$$J_r(p) = \left\| P^\perp \tilde{G}_p \right\|_F^2 = \frac{\left\| P^\perp U_{Gp} \Sigma_{Gp} \right\|_F^2}{\left\| \Sigma_{Gp} \right\|_F^2} \qquad \text{(EQ 43)}$$

$$= \frac{\sigma_1^2 \left\| P^\perp U_{Gp} e_1 \right\|_2^2 + \sigma_2^2 \left\| P^\perp U_{Gp} e_2 \right\|_2^2}{\sigma_1^2 + \sigma_2^2} \qquad \text{(EQ 44)}$$

48

where σ_1 and σ_2 are the two non-zero singular values associated with G_p. The vectors $e_1 = [1, 0]^T$ and $e_2 = [0, 1]^T$ form an orthogonal unit moment orientation pair that spans the row space of G_p. By comparison, $J_f(p)$ can be viewed as

$$J_f(p) = \lambda_{\min}\{ U_{Gp}^T P^\perp U_{Gp}\}$$
$$= \left\| P^\perp U_{Gp} m_p^* \right\|$$

(EQ 45)

where m_p^* is the optimal m_p that minimizes $J_f(p)$ over all unit moment orientations at that location. Comparing m_p^* with e_1 and e_2 above, we can describe the rotating dipole scanning function as a weighted average measure of how *all* dimensions of G_p project onto the noise subspace, while the fixed dipole function is a measure of how *one* optimal dimension of G_p projects. *Thus when $J_r(p) \approx 0$, then $J_f(p) \approx 0$.*

The rank of H is $r = 2p_r + p_f$ and is the crucial piece of information for this model. We otherwise proceed as for the *fixed* dipole model. At each location, we calculate the hybrid scanning function

$$J_h(p) = \lambda_{\min}\{ U_{Gp}^T \tilde{U}_r \tilde{U}_r^T U_{Gp}\}$$

(EQ 46)

where $\tilde{U}_r$ now contains the m-r left singular vectors associated with the m-r smallest singular values, as compared to m-$2p$ and m-p vectors for the two previous models. If at a location p we have a *fixed* dipole, then $G_p m_p$ represents a linear combination of the vectors in G_p that is orthogonal to the noise subspace projector $(\tilde{U}_r \tilde{U}_r^T)$, and we obtain $J_h(p) \approx 0$. Correspondingly, if at a location p we have a *rotating* dipole, then G_p is already orthogonal to the noise subspace projector, regardless of the fixed orientation m_p we attempt to assign, and we still obtain $J_h(p) \approx 0$. *Thus we can use the fixed dipole scanning method for both rotating and fixed dipoles.* We summarize the complete steps in the following section, where we show that this same algorithm can be derived under the proper statistical conditions.

5.2.4 Signal and Noise Subspaces

In the previous section we examined the rotating, fixed, and hybrid models separately. In this section we proceed directly to the general hybrid model $B = H(l, M) S$ and assume that the hybrid gain matrix may represent any mix of fixed or rotating dipoles. We state the assumptions necessary for proving some of the MUSIC assertions.

- [AH] (Gain Matrix Assumption) The $m \times r$ hybrid gain matrix H, $m > r$, is of full column rank r for p dipoles. In other words, the gain columns of the dipole components cannot be combined to simulate the gain columns of a third dipole component. For p_r rotating and p_f fixed, $p = p_r + p_f$ and $r = 2p_r + p_f$.

- [AS] (Asynchronous Assumption) The moment time series for different dipole components are asynchronous or linearly independent, i.e., the time series of one component is not simply a scalar multiple of the time series from another component, nor can any combination of time series form another time series. Thus the time series matrix S is also of full rank r.

- [AW] (Noise Whiteness) The additive noise is considered temporally and spatially zero-mean white noise with variance σ^2, such that the expectation of the outer product of the $m \times n$ noise matrix is $E\{N(n) N(n)^T\} = \sigma^2 I$, where n is the number of time slices. This requirement may be eased by prewhitening of the data, if the noise statistics are known.

The key assumption is that spatially distinct dipoles have linearly independent time series over the measured time segment; however, no constraint is imposed on whether or not the dipole moment is rotating, i.e., the method will work for either fixed or rotating dipoles.

Our model for noiseless data with m sensors, n time slices, and r elemental dipole components is $B = H S$, where H is $m \times r$, $m > r$, and S is $r \times n$, $r < n$. Consider the model for the noisy data under the assumption AW of zero mean white noise, $F = H S + N$. The spatial autocorrelation of the data is then

$$R_F \equiv E\{F(n) \, F(n)^T\} = E\{[HS(n) + N(n)][HS(n) + N(n)]^T\} = HR_SH^T + \sigma^2 I \quad \text{(EQ 47)}$$

where $E\{ \ \}$ is the expectation operator, and $R_S = E\{S(n) \, S(n)^T\}$; by assumption AS, this correlation matrix R_S is of full rank. The square symmetric matrix R_F may be written in terms of its eigendecomposition as

$$R_f = \Phi\Lambda\Phi^T = [\Phi_s \Phi_o] \begin{bmatrix} \Lambda_s & \\ & \Lambda_o \end{bmatrix} [\Phi_s \Phi_o]^T \quad \text{(EQ 48)}$$

where we define Λ_s as the diagonal matrix containing the r largest eigenvalues and Φ_s as the matrix containing the corresponding eigenvectors. By our assumptions, it is well known that the eigenvalue equal to the variance of the noise, $\lambda = \sigma^2$, repeats with multiplicity $m - r$ (Schmidt 1986). Accordingly, $\Lambda_o = \sigma^2 I$, and Φ_o is the matrix containing the corresponding $m - r$ eigenvectors.

Comparing Equations (47) and (48) and using assumptions AH and AS, it is straightforward to show that the space spanned by Φ_s is identical to that spanned by $H R_S H^T$; therefore, Φ_s is said to span the *signal* subspace. The space spanned by Φ_o is the orthogonal complement of the signal subspace and is referred to as the *orthogonal* or *noise* subspace. Based on these observations, it can be shown that the quantity

$$\lambda_{min}\{U_{Gp}^T \Phi_o \Phi_o^T U_{Gp}\} \quad \text{(EQ 49)}$$

is zero for any matrix $G_p = U_{Gp}\Sigma_{Gp}V_{Gp}^T$ corresponding to a true dipole location (Schmidt 1986). Thus we can determine the dipole locations exactly using Equation (49) provided R_F, and hence Φ_o, is known exactly.

In practice, MUSIC approximates R_F by $\hat{R}_F = (1/n) FF^T$. Estimates of the signal and noise subspaces, $\hat{\Phi}_s$ and $\hat{\Phi}_o$, are formed using an eigendecomposition of $\hat{R}_F$. Using this approximation for Φ_o, Equation (49) is now equivalent to Equation (40), which was derived using a deterministic suboptimal least-squares approach. Thus the scanning method presented in this chapter is also equivalent to the MUSIC algorithm for "polarized sources", as defined in (Schmidt 1986), when the assumptions presented here hold true.

5.3 Summary of the MUSIC Algorithm

Summarizing the MUSIC algorithm,

1. Given the $m \times n$ data matrix F for m sensors and n time samples, perform the eigendecomposition of the estimate $\hat{R}_F = (1/n) FF^T = \hat{\Phi}\hat{\Lambda}\hat{\Phi}^T$. Order the eigenvalues, such that $\lambda_1 \geq \lambda_2 \geq \dots \geq \lambda_m$. Equivalently, perform the SVD of F, where the eigenvalues are the square of the singular values.

2. Select the separation point $1 \leq r < m$ between the signal and noise subspace eigenvalues. By assumptions AH and AS, $r = 2p_r + p_f$, where p_r is the number of rotating dipoles and p_f is the number of fixed dipoles; therefore, r is the number of elemental dipoles. While theoretically $\lambda_{min} = \sigma^2$ repeats with multiplicity $(m-r)$, in practice there is some spread among the smaller eigenvalues, depending on the number of time slices n used to estimate R_F. If the signals are of sufficient strength and sufficiently uncorrelated during the time interval, then a distinct drop in the magnitude of eigenvalues will occur between λ_r and λ_{r+1}. (A more detailed treatment of the order determination problem is given recently by Chen *et al.* (1991).) Form the estimated matrices $\hat{\Phi}_s$ and $\hat{\Phi}_o$ from the corresponding signal and noise eigenvectors.

3. Over a fine grid of three-dimensional locations $\{(x, y, z)_p\}$, calculate the corresponding $m \times 2$ gain matrix G_p for each location, obtain the principal left eigenvectors U_{Gp} of G_p, using an SVD such that $G_p = U_{Gp}\Sigma_{Gp}V_{Gp}^T$, and evaluate

$J_h(p) = \lambda_{min}\{U_{Gp}^T\hat{\Phi}_o\hat{\Phi}_o^T U_{Gp}\}$, i.e., the minimum eigenvalue of the bracketed expression. Form two-dimensional slices through the three-dimensional space, e.g., (x, y) planes for constant z, and plot the function $Z\{(x, y, z)_p\} = 1/J_h(p)$ as contours, images, or oblique mesh plots.

4. At each sharp "spike" (minimum of J_h), check to see if the entire subspace of G_p is orthogonal to the noise subspace (both eigenvalues of $\{U_{Gp}^T\hat{\Phi}_o\hat{\Phi}_o^T U_{Gp}\}$ are approximately zero), indicating that the dipole is rotating. Alternatively, if memory storage is not an issue, then at each point when evaluating $J_h(p)$ we can also calculate the rotating cost function $J_r(p) = \left\| \hat{\Phi}_o^T U_{Gp}\Sigma_{Gp} \right\|_F^2 / \left\| \Sigma_{Gp} \right\|_F^2$. Locations where $J_r(p) \approx J_h(p) \approx 0$ indicate rotating dipoles. If the dipole is indeed fixed (only $J_h(p) \approx 0$), we estimate its orientation by calculating the eigenvector associated with λ_{min}. We repeat this analysis until we find p_r rotating dipoles and p_f fixed dipoles such that $r = 2p_r + p_f$. We can refine the estimate of the locations by either using a finer grid in these areas, or by using these estimates as the initialization point for a p-dipole least-squares search.

5. Form the hybrid gain matrix $H(l, M)$ and solve for the time series, $S = H^\dagger F$.

Note that we do not explicitly need to know the number of rotating versus fixed dipoles, p_r versus p_f; instead, we need only $r = 2p_r + p_f$. The values of p_r and p_f are then found by the MUSIC algorithm. We also note that Step 4 indicates the possibility of detecting rotating dipoles by examining not only $J_r(p)$, but by also examining the other eigenvalues of $\{U_{Gp}^T\hat{\Phi}_o\hat{\Phi}_o^T U_{Gp}\}$ found in the calculation of $J_f(p)$; however, we have not studied differences in bias and variance among these various measures of fit.

5.4 Comparison to Other Dipole Fitting Methods

5.4.1 Least Squares Scanning

It should be emphasized that the MUSIC scanning procedure is quite different from fitting the full data with a single dipole. The appeal of the one-dipole model is the relative simplicity with which we can form G_p. An alternative to the MUSIC approach would be to simply fit a one-dipole model at each point in a scanning grid, i.e., compute the function

$$J_{\text{LSS}}(p) = \left\| P_{G_p}^{\perp} F \right\|_F^2 \qquad \text{(EQ 50)}$$

"Least-squares scanning" is then the evaluation of this function as the single dipole is scanned through the head region. The dipoles are assumed to lie at the locations corresponding to the local minima of J_{LSS}. Since we are fitting a one-dipole model, this method will naturally work when there is a single source. However this method generally fails, for example when there are multiple sources that are closely spaced or that generate fields of greatly differing intensities.

Least-squares scanning is equivalent to the beamsteering approach of conventional direction-finding and suffers from the same problems of poor resolution and inter-source interference. The MUSIC approach itself was first proposed in the direction-finding arena to overcome these problems (Schmidt 1986).

5.4.2 PCA Dipole Fitting

The MUSIC algorithm fits a one dipole model to a subspace derived from the data. Principal Components Analysis (PCA) dipole fitting is a related method often examined in MEG analysis, usually with poor results (Maier *et al.* 1987, Achim *et al.* 1988, Mocks and Verleger 1986, Wood and McCarthy 1984). Although PCA dipole fit-

ting also scans a one dipole space derived from a similar decomposition, the subspace framework presented here allows us to examine this method and show where it fails.

PCA dipole fitting begins with the identical step of decomposing the data matrix F into its orthogonal components, $F = U\Sigma V^T$, then selecting the signal subspace. As described by Maier *et al.* (1987) and analyzed by Achim *et al.* (1988), the columns of U are the spatial distribution of the principal components, and the columns of V are the corresponding time functions. The matrix $W = U\Sigma'$ describes the "factor loadings," where Σ' contains only the r principal singular terms; this definition of W is consistent with our definition in Section 4.1.2.

The PCA method fits a series of r single dipole models to the principal components as follows. The pth dipole location and moment are chosen as a least squares fit to a linear combination of the factor loadings,

$$\min_{l_p, q_p} \left\| G_p(l_p)q_p - Wc_p \right\| \tag{EQ 51}$$

where $G_p(l_p)$ is the gain matrix for a dipole at location l_p and q_p is the dipole moment. In (Achim *et al.* 1988), Achim *et al.* chose the individual terms of c_p to be $c_{pp} = 1$ and $c_{ip} = 0$ for $i \neq p$. In this case a single dipole is fit to each of the columns of W. Alternative choices of the rotation factors c_{ip}, such as Varimax, are discussed and analyzed in (Mocks and Verleger 1986, Wood and McCarthy 1984) and elsewhere.

The error in Equation (51) can be written as

$$J_{\text{PCA}}(p) = \left\| Wc_p - G_p q \right\|_2^2 = \left\| Wc_p - G_p (G_p^\dagger Wc_p) \right\|_2^2 = \left\| P_{G_p}^\perp Wc_p \right\|_2^2 \tag{EQ 52}$$

where $P_{G_p}^\perp$ represents the orthogonal projection for a *single* dipole. The limitations of PCA dipole fitting are now apparent. PCA dipole fitting will succeed only if the coefficients in c_p are correctly selected, such that Wc_p lies in the two-dimensional subspace spanned by G_p. However, this requires that we know the dipole location before we begin.

55

As an example of the inaccuracy of PCA, Achim *et al.* (1988) show a case in which PCA

severely mislocates one of three dipoles in a *noiseless* simulation.

Chapter 6

Applications of MUSIC

6.1 MEG

6.1.1 Simulation

In this chapter, we present results using the MUSIC algorithm for both simulated data and experimental somatosensory data. We begin by using the same simulation model and data as in Figure 7 on page 38, where at each of 37 sensor locations we simulate 100 time samples. Since by design we have two fixed dipoles and one rotating, then our data model has a rank of four for three dipoles. We perform an SVD of the simulated noisy data matrix F and plot the singular values, of which the first ten are shown in Fig. 9.

The abrupt drop between values 4 and 5 give a clear indication in this simulation that the number of elemental dipoles is 4. We form the noise subspace estimate $\hat{\Phi}_n$ from the eigenvectors associated with singular values 5 to 37. We form the gain matrix at each voxel in the region $x = -5$ to 5 cm, $y = -5$ to 5 cm, and $z = 6$ to 9.5 cm, at 0.5 cm intervals. The minimum eigenvalue at each position using Equation (40) is found, then the inverses of these values are formed into two-dimensional images for fixed z.

The results are shown in Fig. 10. The cost function shows three distinct peaks in Fig. 10(a) between $z = 8$ and $z = 9$ cm. The true locations, given in Table 1 on page 39, are just below the plane $z = 8.5$ cm and agree well with the positions shown in the figure. Fig. 10(b) shows the inverse of the second eigenvalue found in the evaluation of Equation (40). The figure shows a distinct peak for the single rotating dipole in this sim-
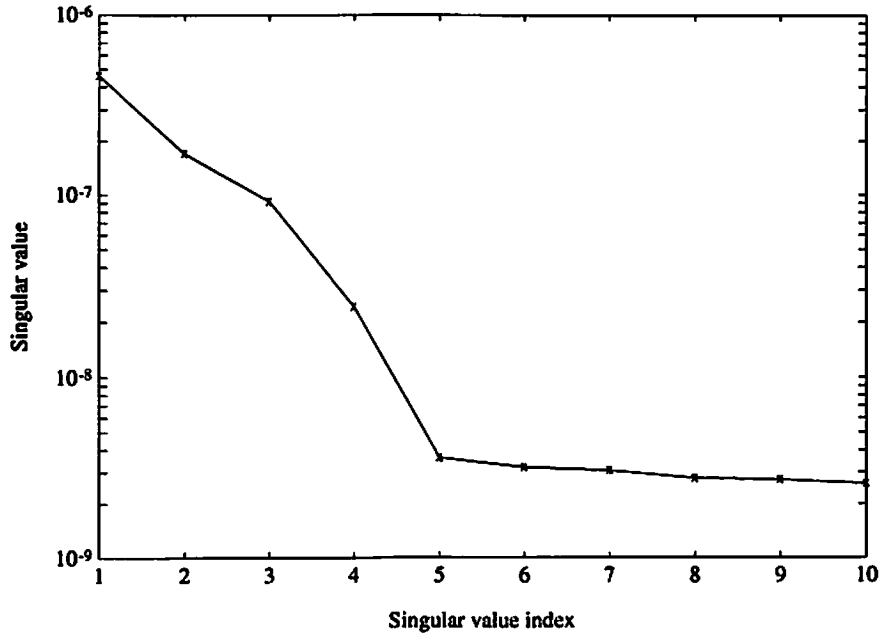
FIGURE 9. Singular values for simulated noisy data matrix F. For clarity, only the first 10 of 37 singular values are plotted. The abrupt drop between singular values 4 and 5 gives a clear indication in this simulation that the number of elemental dipoles is 4. The noise singular values corresponding to indices 5 and upward are seen to be approximately equal.

ulation. We could refine our estimates by either scanning more finely around the $z = 8.5$ plane or by using these scanning estimates as an initialization point for a full three-dipole least-squares fit.

6.1.2 Phantom Example

A seven-sensor, 2nd-order gradiometer system was placed in six different positions about a glass sphere of radius 9 cm, for a total of 42 measurement locations. Four dipole sources were placed inside the sphere, which was filled with a conducting solution. The sources were coaxial cables, with the inner conductor extending 1 mm beyond its coaxial sheath. The sources were located within the sphere using a probe position indicator.

58
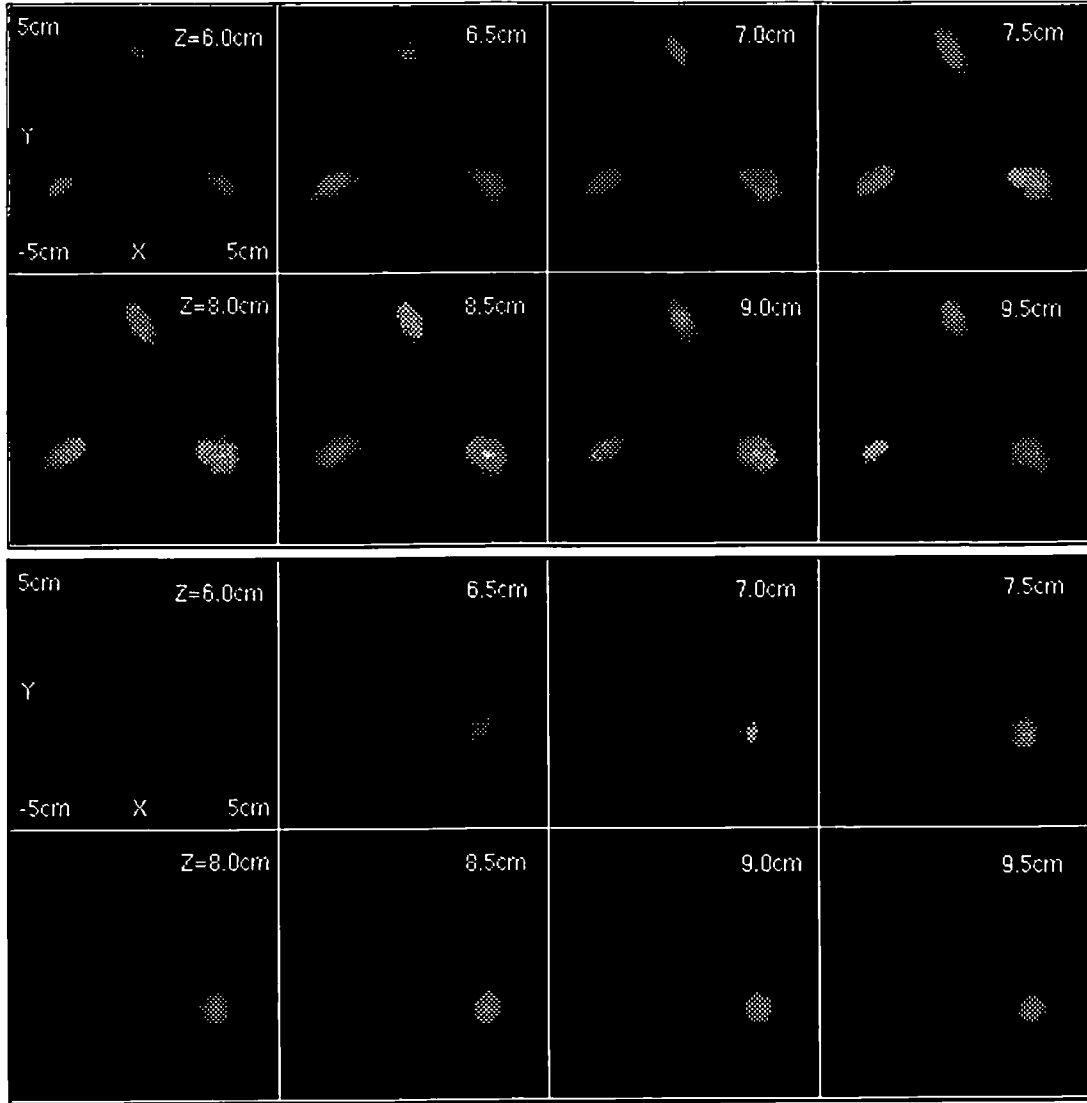
FIGURE 10. Simulation Results. Each subimage is a two-dimensional slice in the (x,y) plane for $z = 6$ cm to 9.5 cm. Each (x,y) slice was formed at 0.5 cm intervals, from -5 to 5 cm in both the x and y directions. The simulation data are identical to the least-squares example, where the SNR is approximately 10 dB. The top set of images is from the fixed dipole function, $J_f(p)$, Equation (34). Here we have encoded the image as white to represent the minima in the cost function. The lower set of images, also from the fixed dipole model, shows the second (non-minimum) eigenvalue; a minimum in the second eigenvalue indicates the presence of a rotating dipole, as discussed in the text. The single minimum here correctly identifies the one rotating dipole. The true locations, given in Table 1, are approximately in the $z = 8.3$ cm plane, with good agreement in the positions indicated here.

59

Fig. 11 displays the average absolute response recorded over all sensors, where we see the overlap between the source responses. Each source produced an approximately 30 ms wide monopulse, with each source firing about 8 ms after the previous, such that the fourth source was activated before the first source had completed its response.

Phantom Data, Four Sources, 8 ms delay, 30 ms duration
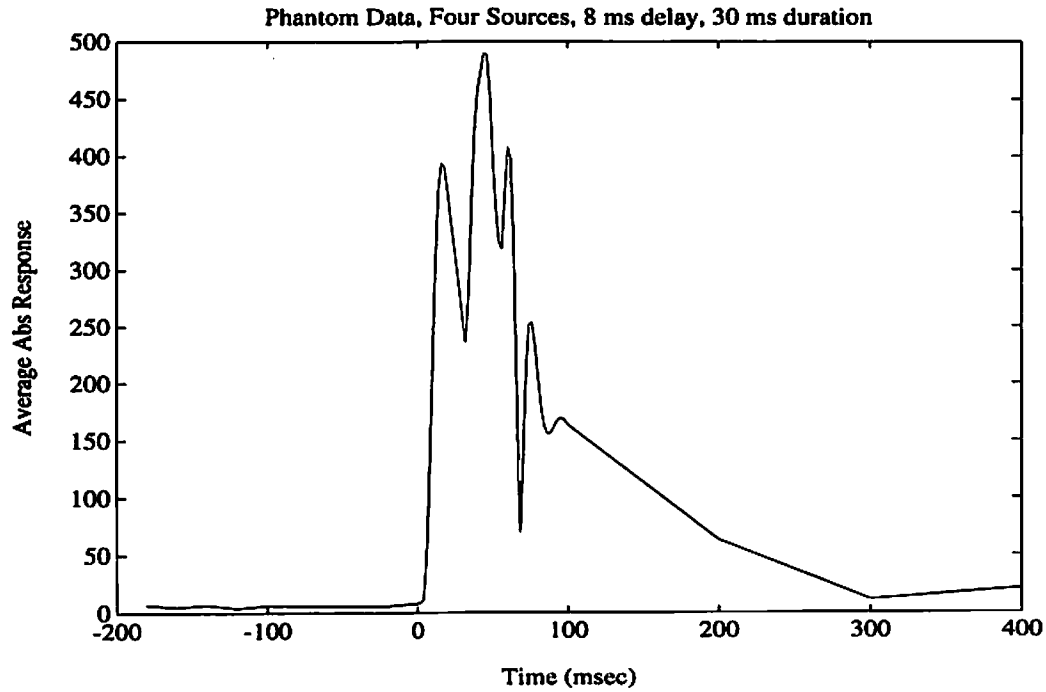
FIGURE 11. Average of the absolute response across all sensors for the phantom experiment.

Using the MUSIC algorithm, the data set was scanned over a 20 cm source cube at a 0.5 cm sample interval to establish the overall quality of the data and to confirm the absence of ambiguous head regions (strong local minima). These 5 mm scans were then used to select the 1 mm scan region. The results of the 1 mm scans were examined by converting the three dimensional metric information into two dimensional slices. From these slices the "peaks" (points where the metric approached zero) were identified. The true locations of the sources and the identified locations are given in Table 2.

60

In Fig. 12 we show two axial slices from the one millimeter MUSIC scans. Both slices span the x-axis horizontally from -2 to 2 cm and the y-axis vertically from -2 to 2 cm. Figure (a) is for $z = 6.5$ cm, and Figure (b) is for $z = 7.8$ cm. The locations of the peaks are given in Table 2. Sources 2 and 4 were well resolved, as indicated by the narrow peaks in both figures and the good agreement with the true locations in Table 2. The other source that was identified had a much broader peak that spans the region near Sources 1 and 3, indicating that these two closely spaced sources may not be resolvable by this array configuration. Indeed, the three sources identified explain 99 percent of the data variance.

TABLE 2. Coordinates of located sources (centimeters) for the true, MUSIC, three ("LS 3") and four ("LS 4") dipole least-squares fit. The "Error" is distance to the true location, and the "Variance %" is the percent variance explained by the locations. Dipole (3) was not distinguishable as a separate source in the MUSIC run.

Source		True	MUSIC	LS 3	LS 4
	x	0.16	0.2	0.3	0.3
Dipole 1	y	-0.82	-1.0	-1.0	-0.6
	z	5.90	5.9	5.8	6.1
Error			0.2	0.2	0.3
	x	0.88	0.9	0.5	0.6
Dipole 2	y	-0.28	-0.4	-0.3	-0.4
	z	6.30	6.5	5.9	6.2
Error			0.2	0.6	0.3
	x	-0.15			0.3
Dipole 3	y	-0.30			-0.6
	z	5.20			6.1
Error					1.1
	x	0.27	0.3	0.3	0.3
Dipole 4	y	0.81	0.8	1.0	1.1
	z	7.75	7.8	8.4	8.4
Error			0.1	0.7	0.7
	Variance %	99.4	98.9	99.4	99.7
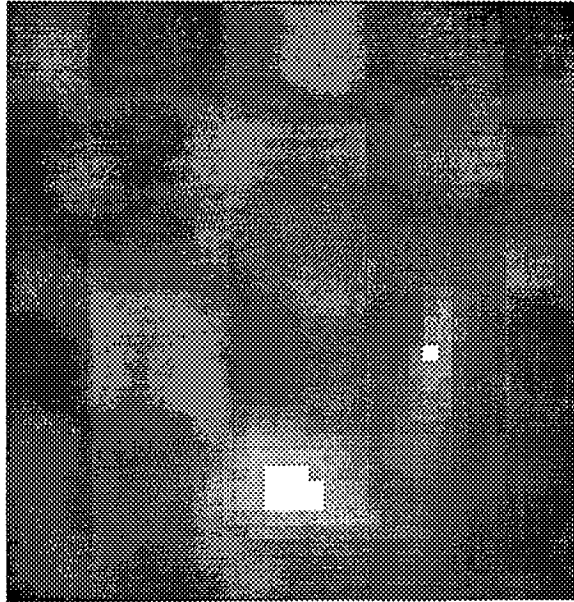
z = 6.5 cm
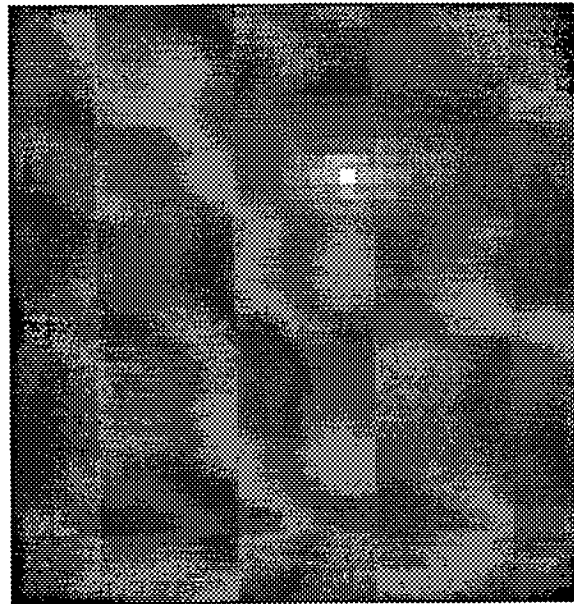
z = 7.8 cm

FIGURE 12. One millimeter MUSIC axial slices of phantom data in the x-y plane. Each image spans -2 to 2 cm on the x-axis horizontally and -2 to 2 cm on the y-axis vertically. Table 2 gives the locations of the peaks.

The true locations were then used as the initialization point for a nonlinear least squares localization algorithm. Both a three dipole and a four dipole model were fit to all of the data. The moment orientation was not constrained. As shown in Table 2, the least-squares solutions were just slightly better able to explain the variance of the entire data set, but at an increased error in the location over that of the MUSIC results. We see that the MUSIC results are quite good for this data set. Repetitions of this experiment should be conducted to determine the variance of these results.

6.1.3 Somatosensory Example

For the somatosensory experiment, the data were generated by vibrotactile stimulation (using a piezoelectric speaker element) of the right thumb, the right ring finger, and then both digits simultaneously. The intent was that the evoked field pattern for "both digits" might reflect a summation of the fields evoked by the stimulation of thumb and ring finger alone. The data were collected during eleven placements of a seven-sensor, 2nd-order gradiometer system, at each placement averaging 300 trials. The data were digitized for 300 milliseconds (100 pre-stimulus and 200 post-stimulus) at 1 kHz and were filtered on line between 1 Hz to 100 Hz. Fig. 13 displays the average absolute time response across all sensors for the three experiments, "ring", "thumb", and "both". Since piezoelectric stimulation creates a large stimulus artifact, the data were partitioned into a prestimulus interval up to 0 msec and a poststimulus interval after 24 msec.

Fig. 14 plots the first ten singular values from the decomposition of the spatio-temporal data matrices. The upper three curves are from the SVD of the poststimulus data matrices, and the lower three correspond to the prestimulus. The shape of the post-stimulus curves and the merging of the prestimulus curves leads us to select the first six eigenvectors as our signal subspace. (For subspace orders five and four, we also obtained results similar to those presented below.) Fig. 15 displays the results of a five millimeter

63
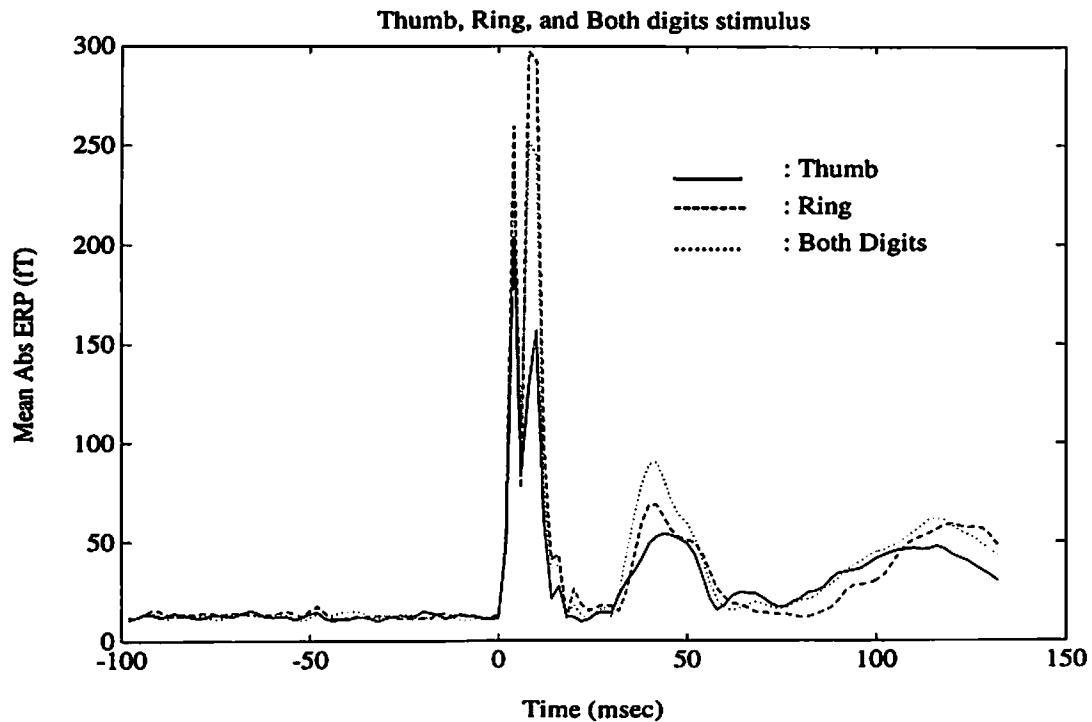
FIGURE 13. Average Absolute Evoked Field. The data were rectified across all sensor locations and averaged to give an indication of the temporal activity.

grid MUSIC scan for the "both digits" stimulation, using the first six principal components of the poststimulus interval. Each subimage represents an axial slice of the head in five millimeter increments along the z-axis, with the left ear at the top of the image and the nose at the right. The head coordinate system used was the x-axis through the nose, the y-axis through the left ear, and the z-axis up through the top of the head.

One millimeter scans were then centered on the observed peaks seen in the five millimeter scans. Fig. 16, Fig. 17, and Fig. 18 display axial scans in one millimeter increments, from $x = -2$ to 2 cm, $y = 3$ to 7 cm, and $z = 6.1$ to 8 cm. We see a clear shift in the response among the three data sets in both the y and z coordinates. Fig. 19 summarizes the results from the $z = 7.3$ centimeter slice, where we have overlaid contour plots with full gray scale images. Here we clearly see the distinct separation between the peaks for the thumb and the ring finger stimulation. The response due to the "both digits"
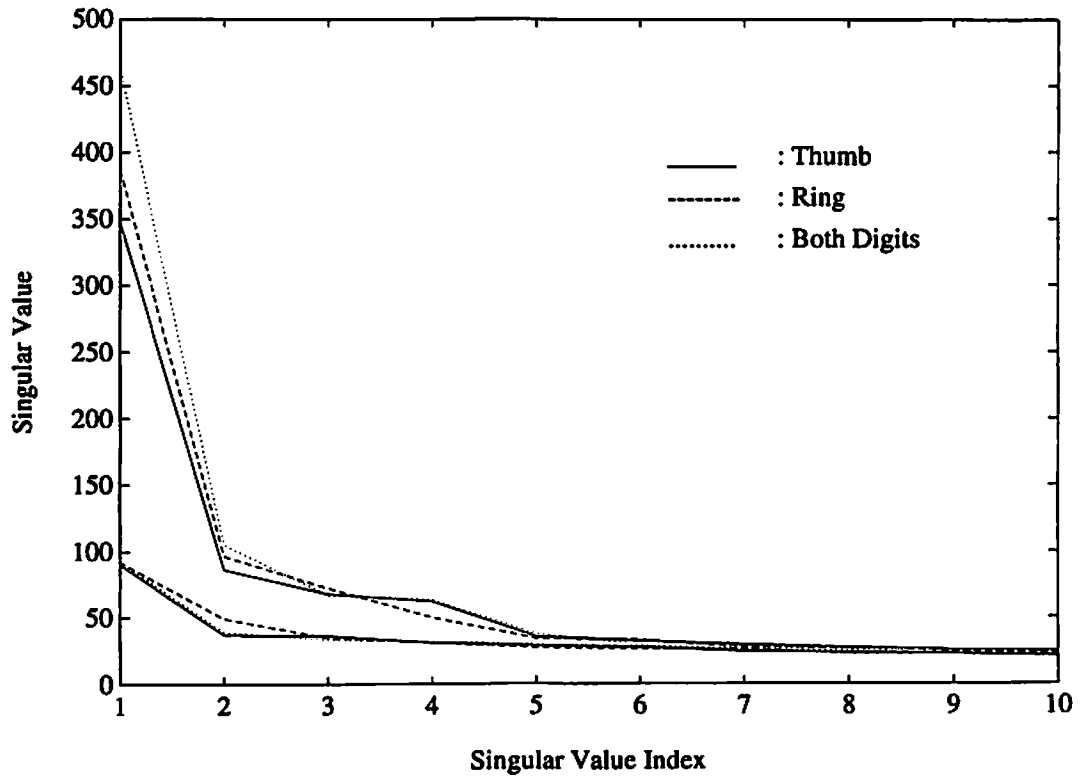
FIGURE 14. Singular Values of Somatosensory Data Matrices. The top set of curves correspond to the three sets of poststimulus data (data after 24 msec), and the bottom set corresponds to the prestimulus data. We selected order six as our signal subspace; similar results were obtained for orders five and four.

stimulation actually peaks in the z=6.9 cm plane, but we see in this z=7.3 cm plane the indications of a possible summation of the response from the two somatosensory centers. A more thorough analysis would include discussions of noise correlation, order selection, and physiological interpretation, but we defer such analysis, since the emphasis here is simply to illustrate the utility of MUSIC analysis with real data.

6.2 Thunderstorm Localization

6.2.1 Simulation

Fig. 20 displays the simulated positions of two "storms" for ten different sequential instances. The point charges were each positioned at an altitude of 4 km and given a
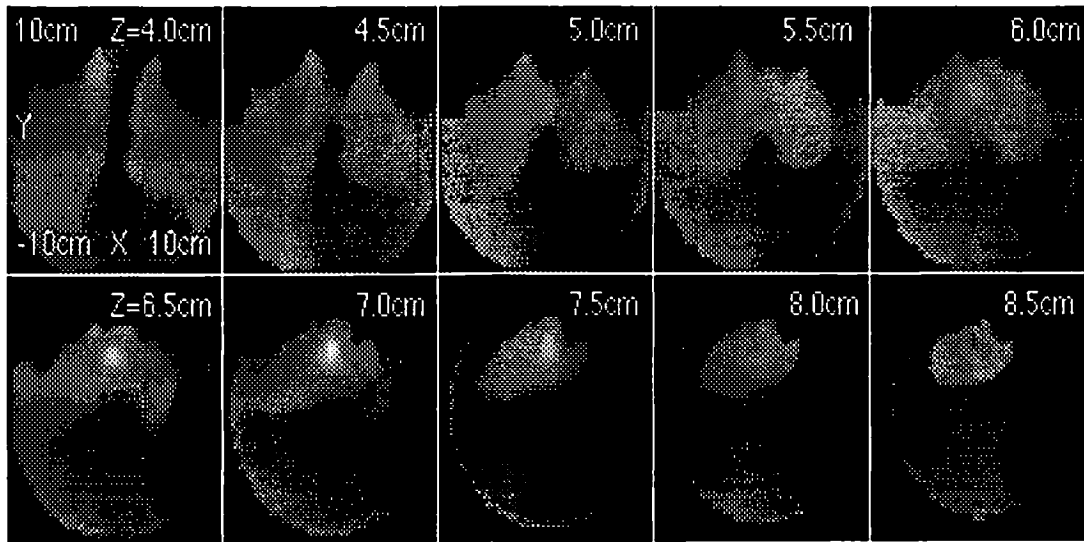
FIGURE 15. Axial scans of the "both digits" stimulation case. Each subimage is a two-dimensional slice in the *(x,y)* plane for *x* = -10 to 10 cm, *y* = −10 to 10 cm, and *z* = 4 to 8.5 cm. The scanning grid increment is 0.5 cm in all directions. Based on these results, a 1 mm scanning grid was then formed around the indicated minima.
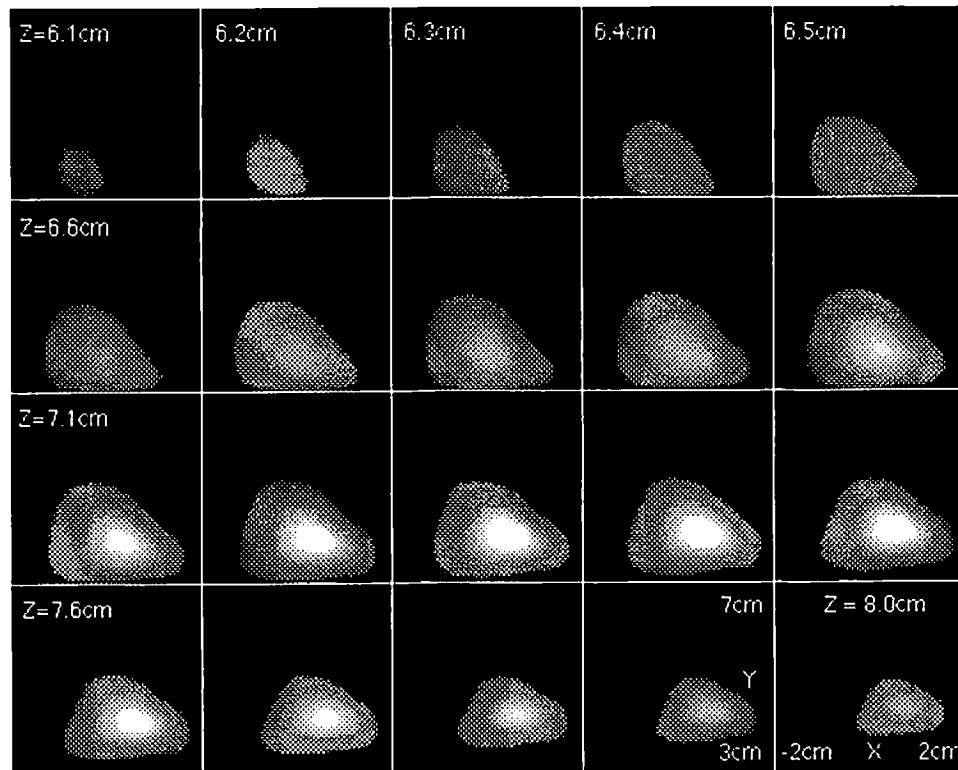
FIGURE 16. One millimeter axial scans of Ring Data. Each subimage is a two-dimensional slice in the *(x,y)* plane for *x* = −2 to 2 cm, *y* = 3 to 7 cm, and *z* = 6.1 to 8 cm. The scanning increment is 0.1 cm in all directions.
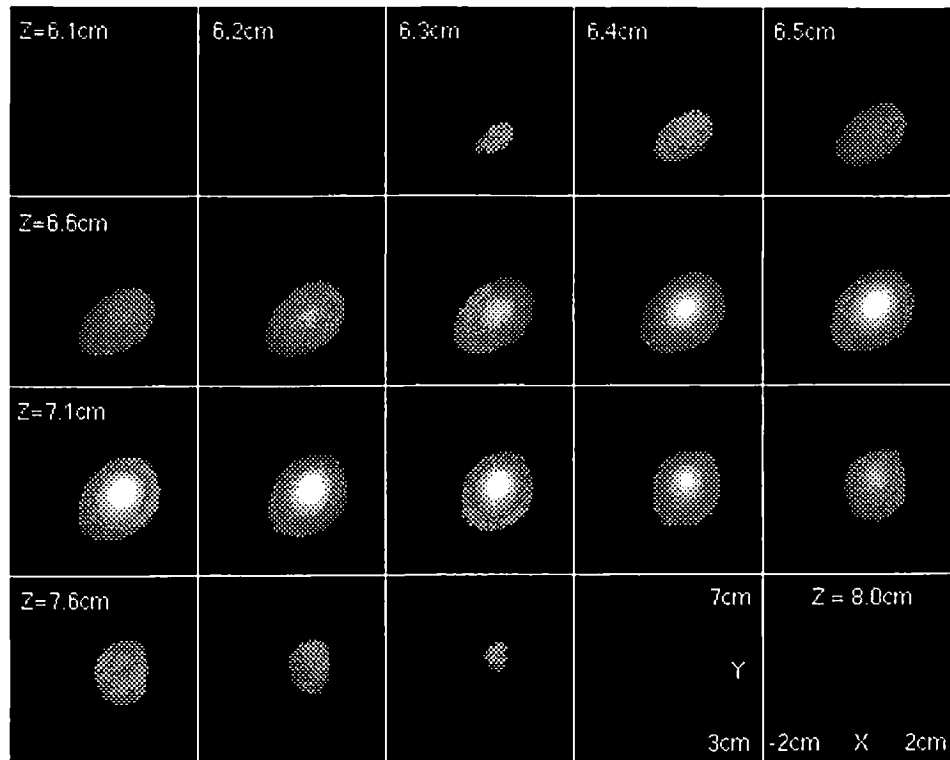
FIGURE 17. One millimeter axial scans of Thumb Data.
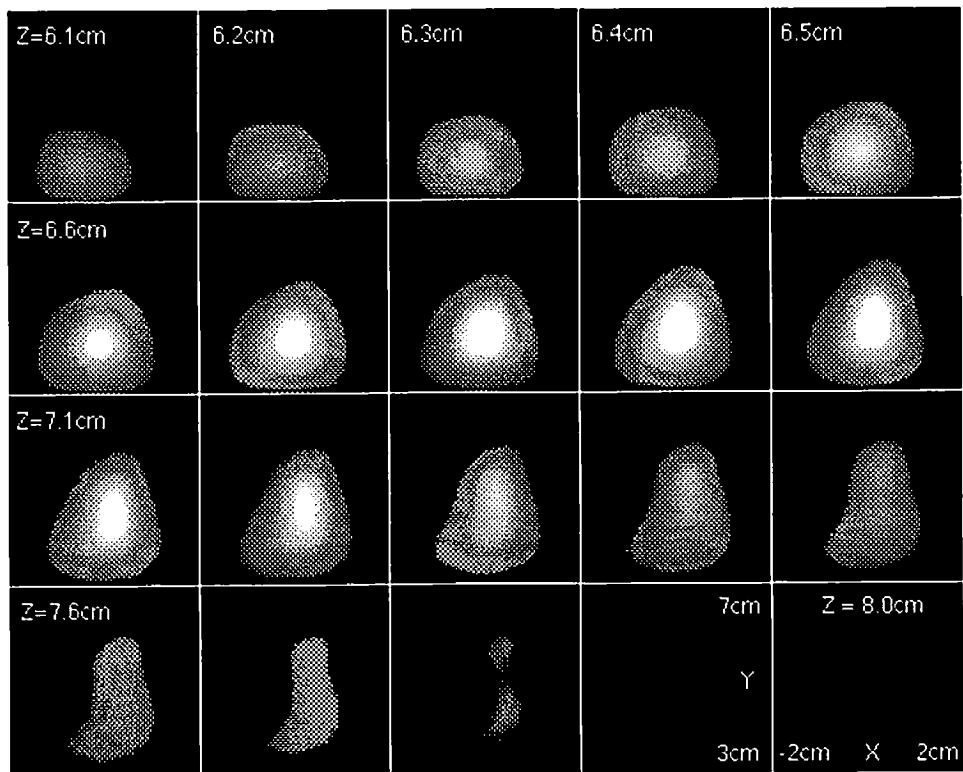
FIGURE 18. One millimeter axial scans of Both Digits Data.

67
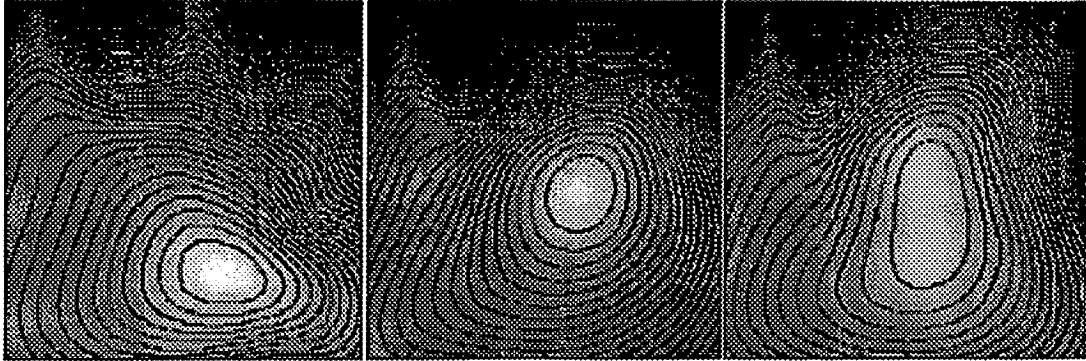
FIGURE 19. Comparisons of the one millimeter scans at z = 7.3 cm. The (x,y) dimensions remain x = −2 to 2 cm and y = 3 to 7 cm. Contour plots of the axial slices are overlayed with a gray scale image of the data. On the left is the "ring" data, in the middle is the "thumb" data, and on the right is the "both digits" data.

nominal charge of 10 coulombs. Random noise uniform over +/- 0.5 coulombs was added to each charge for ten samples at each time position. Thus 100 total time samples were simulated for the charges as they moved across the cape. The bottom figure in Fig. 20 displays the total simulated fields measured across the KSC sensors. We thus have one charge passing from west to east over the Vertical Assembly Building while the second charge moves roughly from north to south over the Cape Canaveral Air Force Station. The intent is to show (a) the sharpened resolution as the storm cells move from outside the array into the center of several sensors, and (b) the relative ease with which MUSIC tracks two simultaneous charges.

Fig. 21 shows the overlay of all 31 simulated time sequences across the cape. The abrupt transitions correspond to the jump from one storm position of ten samples to the next position, i.e., we did not smoothly move the storms from position to position. These jumps serve as our discontinuity or incoherence in trying to fit our model to the data, effectively serving here as our lightning strikes. Since the quasi-static charge model requires a stationary source, we can visually see how this simulated data should be partitioned into ten even segments of time; however, we need a more objective measure of dividing this stream of data.
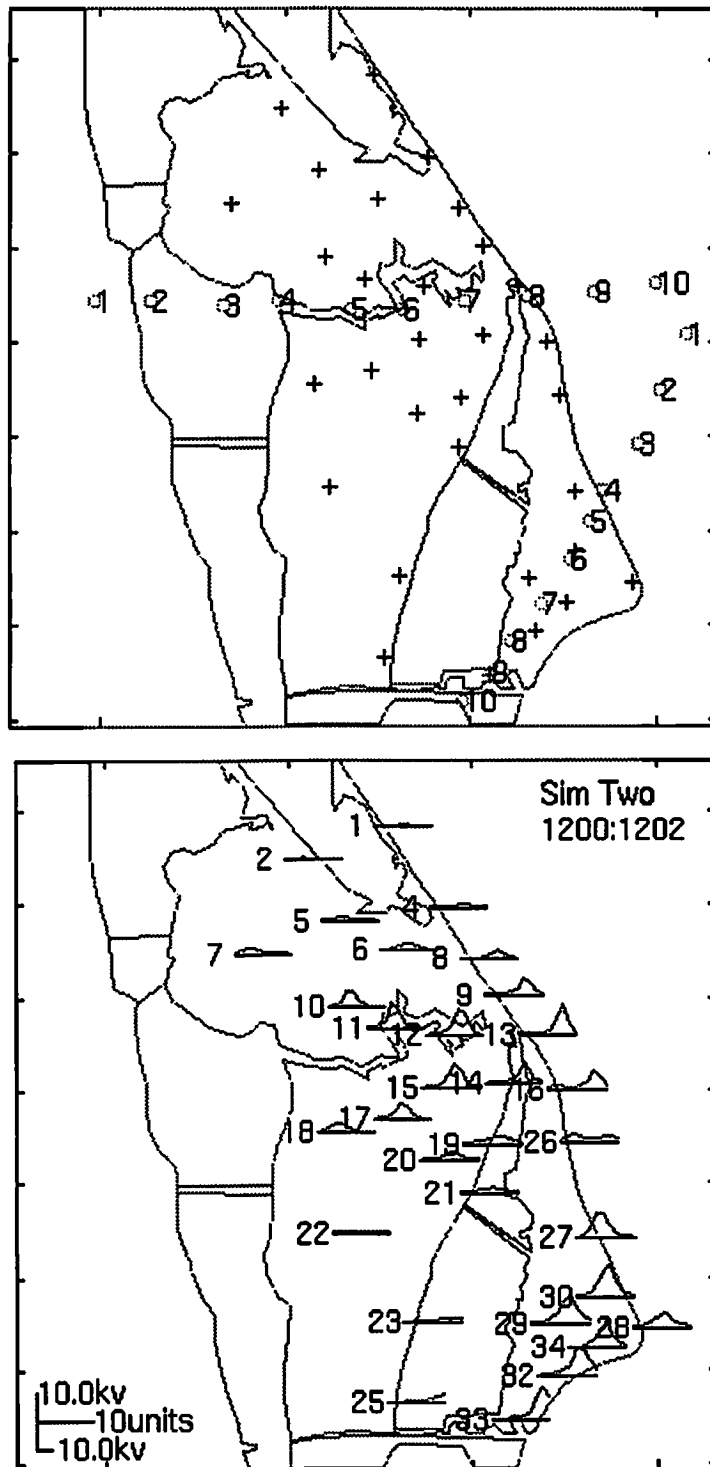
FIGURE 20. Two simulated charges. The top figure shows the position of the two charges for ten different time segments. The bottom figure shows the simulated field intensity recorded at each sensor as the two "storms" pass through the Cape.
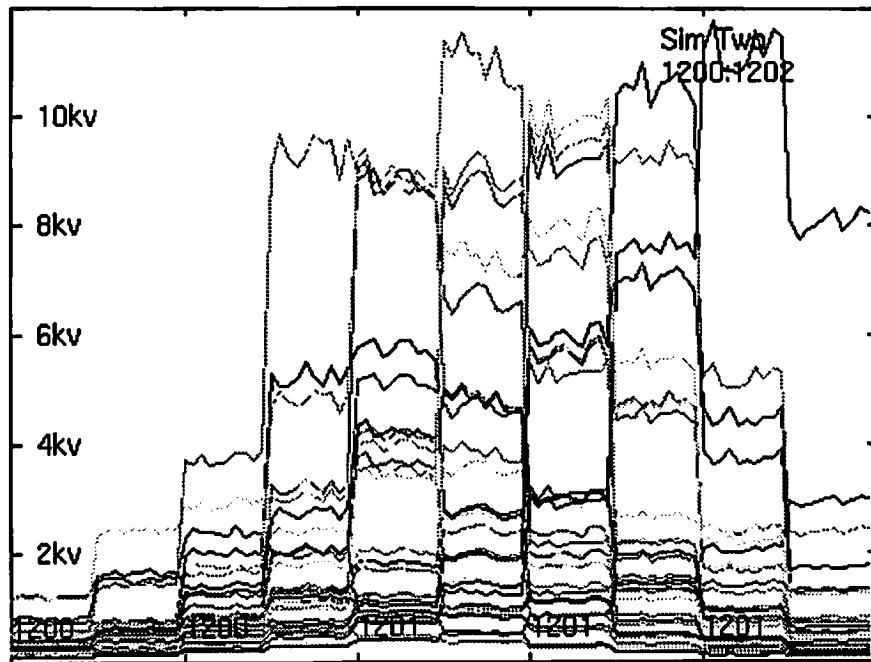
FIGURE 21. Overlay of simulations. All of the simulated fields recorded at each sensor are overlaid here. The visibly abrupt changes indicate where we have shifted the "storm cells" up to the next time segment, for ten time segments total.

Section 9.3.1 presents the results of apply time-eigenanalysis to this same simulation to show how the data could be parsed. Here we simply assume we know how to partition the time data into its proper segments. Fig. 22 is the MUSIC scan of the first time segment of simulation presented in Fig. 20. In this position, both charges are just outside of the KSC array, one charge to the west, the other offshore. The top figure is the MUSIC scan at 4 km in altitude, where we have colored the MUSIC intersections from "poor" to "perfect" as dark red to white, respectively. We see in this image perfect peaking at the correct position "1", as confirmed in Fig. 20. We also note the relatively broad smearing around these peaks, to be expected from the Cramer-Rao results. The bottom figure in Fig. 22 illustrates the vertical smearing of the MUSIC spectrum as well. The results of ten MUSIC scans, each at increasing 1 km increments, are stacked on top of one another, but we have only tagged with a "*" those regions of the slices whose inter-

section was greater than 85%. Effectively we are viewing a large distorted three-dimensional ellipsoid in space, whose center represents the source location.

We contrast the smearing of these position 1 results with the precision of the results in Fig. 23, which presents the MUSIC results for position 6. In this position, both storm cells are well situated within a cluster of sensors. The top figure is again the MUSIC scan at 4 km, and here we note the tightness of the peak. The bottom figure is the view again from the southwest of all ten MUSIC scans for each corresponding 1 km of altitude, where only those regions greater than 85% tagged with a "*." In contrast with the position 1 results, here we see excellently localized peaks in both the horizontal and vertical directions. This well-focused MUSIC sphere corresponds directly with the excellent Cramer-Rao results predicted for these regions of the cape.

We ran the MUSIC spectrum for the other eight simulated positions as well, obtaining comparable results, then plotted them in a manner identical to Fig. 22 and Fig. 23. These ten images were then arranged in a sequence and played as a "cine" or movie loop on the computer. The result is a very effective demonstration of the ability of the MUSIC scans to reinterpret the KSC array of field mill data into a visually informative and insightful sequence of graphical images. One area of further research is to integrate this visual modality of the mill data into the other graphical weather presentations, such as weather RADAR, LDAR, and the lightning detection network. Effective integration will allow the weather forecaster to more readily assess and incorporate the unique field mill information into the overall weather operations.

6.2.2 Intense Lightning Example

Fig. 24 displays 360 seconds of thunderstorm data, parsed down from 600 seconds of data that contained several lightning strikes. The parsing was done using time-eigenanalysis as a guide, described in Chapter 9. We selected two time segments, one
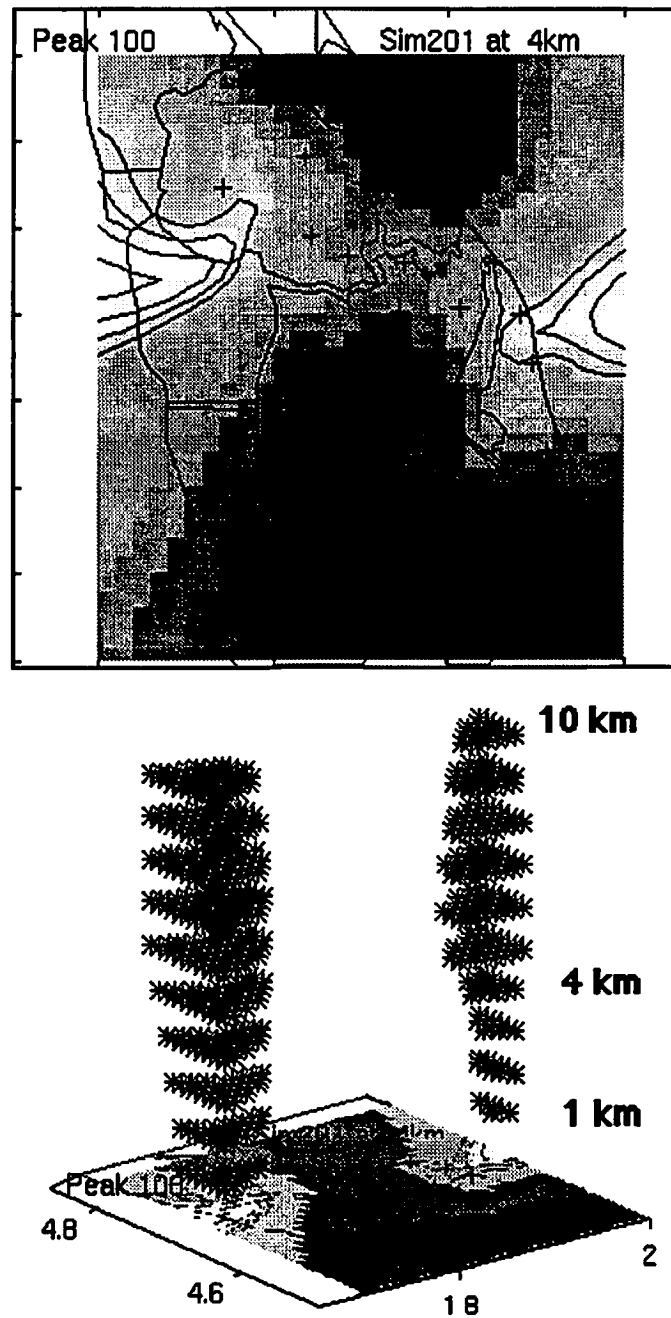
FIGURE 22. MUSIC Simulation I. The time segment is the first in the simulation, when the "storm cells" are just outside of the KSC array. The top figure is the view from above the Cape, and the bottom view is the view from the southwest. The analysis was done on 1 km planes, and any voxels greater thatn 85% were simply tagged to form a stack of images as seen here. We observe how the MUSIC spectrum smears away from the array, consistent with the Cramer-Rao analysis.
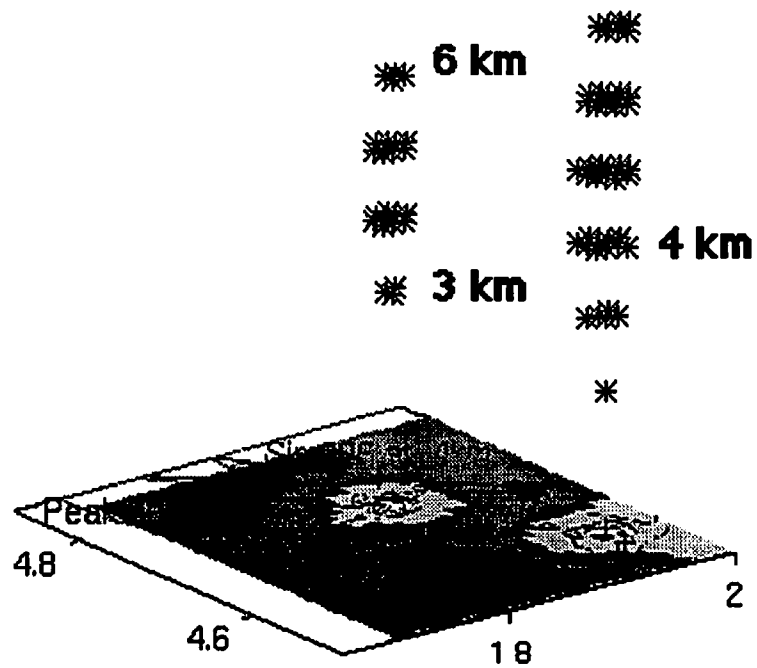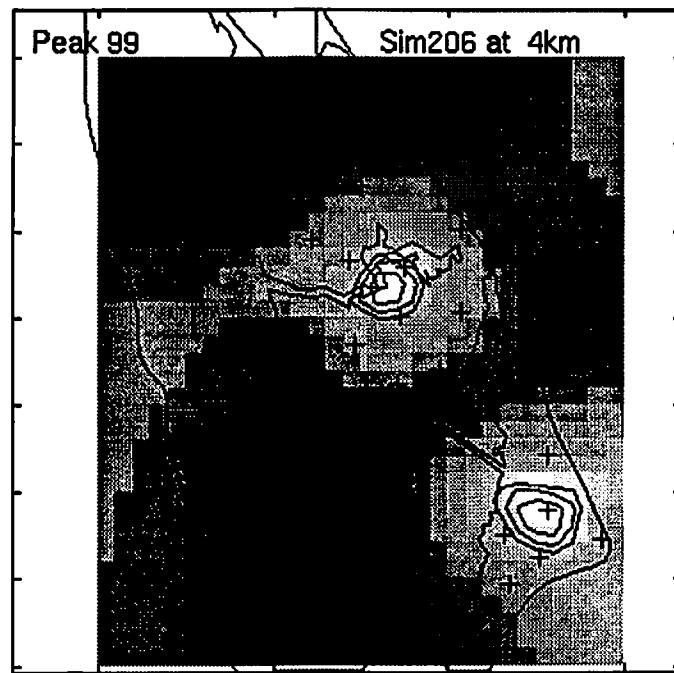
FIGURE 23. MUSIC Simulation II. The time segment is the sixth in the simulation, well situated within the KSC array. In contrast with Fig. 22, we note the tightness of the MUSIC peak inside of the KSC array, again consistent with the CRLB analysis.
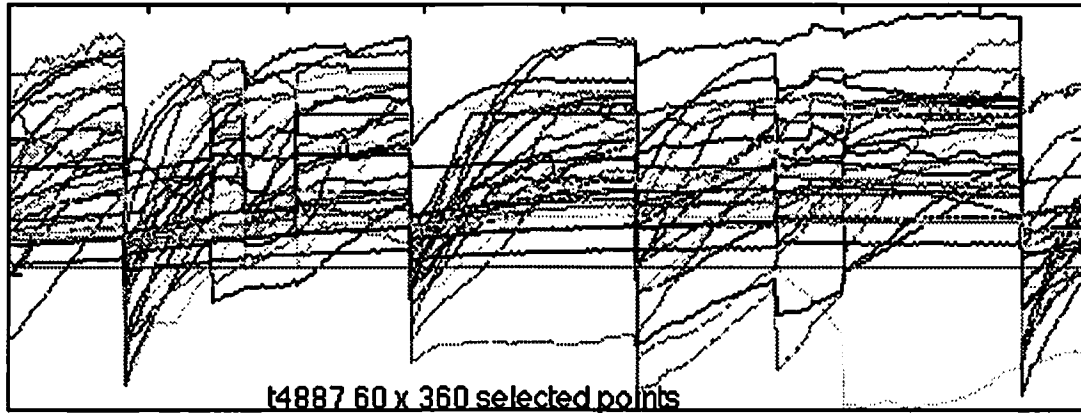
FIGURE 24. Using the time-eigenspectrum techniques discussed in Section 9.3, we parsed 600 seconds into the 360 seconds shown here. We then divided this segment into six even segments of 60 seconds for MUSIC processing.

with residual lightning activity still evident, the other a much more static region between strikes.

The top figure in Fig. 25 is from the second time segment, time data 61 to 120, and the bottom figure is from the fourth time segment, time data 181 to 240. Segment two contained many low similarity regions in its time-eigenspectrum, and the MUSIC spectrum is correspondingly broad and somewhat poor. Segment four contained a very stable low rank time-eigenspectrum, and we see a corresponding well defined peak. The peak aligns with the intuitive interpretation of the storm center, obtained by examining the field levels manually. We also note the same broadening of the peak of the solution outside of the array, as was seen in the simulation data presented in Fig. 22.

Fig. 26 more closely shows the peak seen in the right of Fig. 25. We again tag all MUSIC results above 85% for the 1 km planes, and view this stack from the southwest. Here we see the stack peaking at a minimum of 10 km, which would appear to be unrealistically high; however, further examination leads us to believe that the coronal damping of the fields are the cause of this vertical error. Further research effort will investigate if we can incorporate coronal damping into the model to allow more accurate vertical positioning
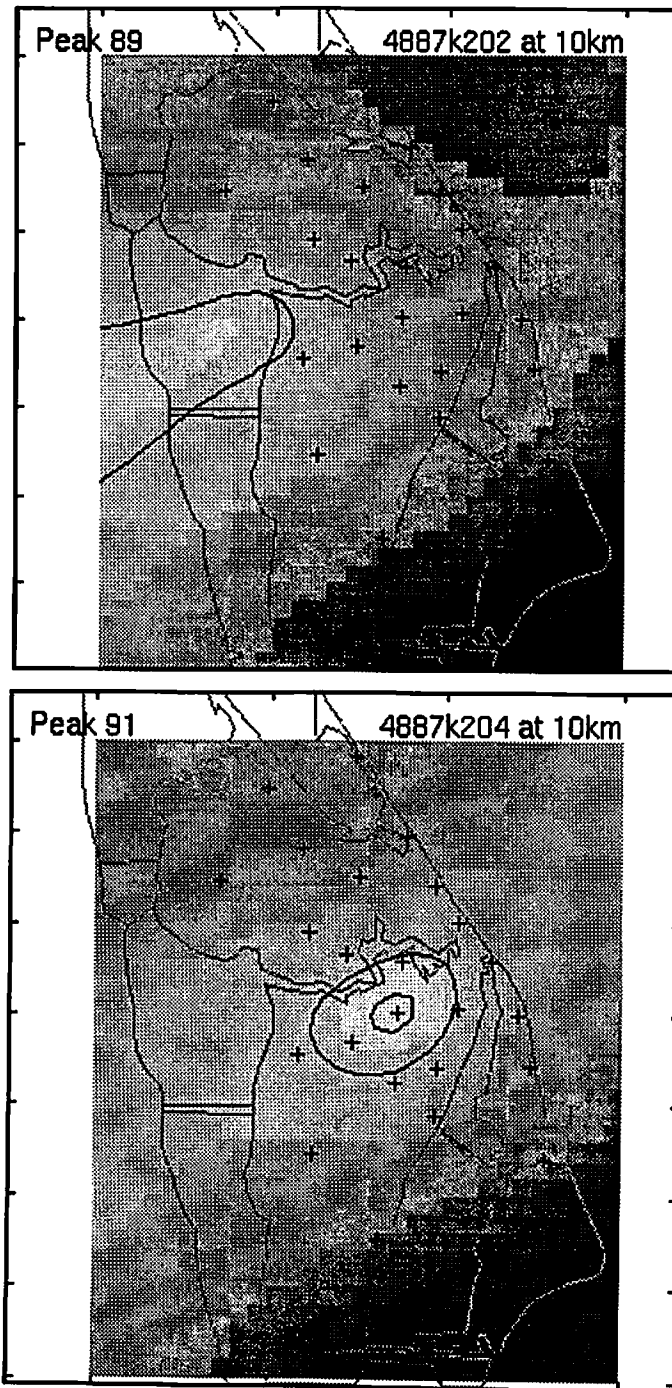
FIGURE 25. MUSIC Thunderstorm example. The top figure is from the second time segment, time data 61 to 120, and the bottom figure is from the fourth time segment, 181 to 240. Segment two still contained residual lightning activity, and its MUSIC spectrum appears correspondingly broad and poor. Segment four contained a very stable low-rank region of data, and we see a corresponding well defined peak. The peak aligns with the intuitive interpretation of the storm center, obtained by examining the fields manually.

10,000 meters

8,000

6,000

4.8

4.6

2
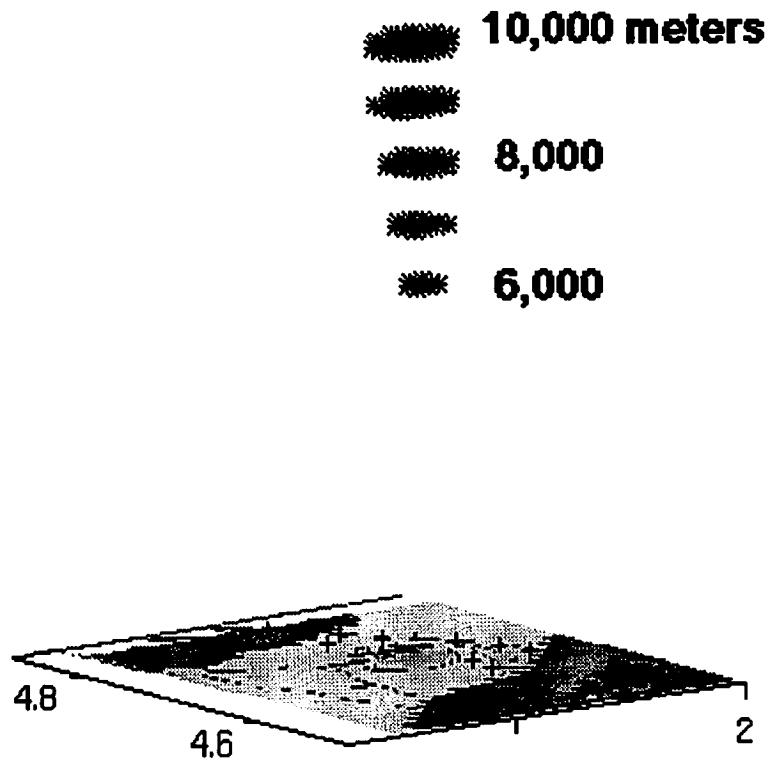
FIGURE 26. MUSIC Example detail. Tilting the fourth segment into a southwest view, we see that the MUSIC scan is peaking above 10 km, although it is well defined in the horizontal plane. The error in locating the storm vertically is believed due to the coronal damping of the fields.

We repeated this MUSIC analysis for the other four 60 second segments and again formed a cine loop for presentation and analysis. The loop shows peaks over a range roughly between the two presented here. The overall result is a quite consistent localization of the source in the same region of the cape, even with data not ideally quasi-static.

For an additional example, in Section 9.3.3 on page 136 we examine an End-of-Storm-Oscillation (EOSO) for its time-eigenspectrum, then produce MUSIC images of two regions in the EOSO.

Chapter 7

Cramer-Rao Lower Bound

7.1 Background

The simplest head model in use is a set of homogeneous spherical shells, for which the MEG model is straightforward and the EEG model is still tractable, but with more parameter assumptions. Although a dipole comprises six parameters, the focus of most research has been on the accuracy of determining the three location parameters. Early studies compared the relative localizing ability of EEG and MEG (Cuffin and Cohen 1979, Cohen and Cuffin 1983). In (Stok 1987), several of the model parameters were varied to determine which had the greatest impact on accuracy. In (Cuffin 1990 and Cuffin 1991), the head shape and sphere models were examined for their accuracy impacts. In (Cuffin 1986), variations of noise and measurement errors were explored for several array configurations. In (Kaufman *et al.* 1991), the dipole source is expanded to a larger spatial extent to test the dipole assumption in cortical folds for both EEG and MEG models. In (Achim *et al.* 1991, Baumgartner *et al.* 1991), the spatiotemporal model was examined to determine its effectiveness in improving location accuracies.

The accuracies found and the conclusions drawn by these studies vary widely. Direct analysis of the localization error is complicated by the nonlinearity of the location parameters, the sensitivity to the moment orientation, the moment intensity, the background noise power, the orientation and spatial extent of the sensors, and the absolute position of the dipole. Consequently, most of these studies and comparisons were restricted to specialized dipole locations or sensor positions. The error results were generally established by experimental data or by Monte Carlo analysis. More recently,

dipoles implanted in patients have been used in an attempt to determine localization errors in MEG (Balish *et al.* 1991) and to compare localization errors between EEG and MEG (Cohen *et al.* 1990). The results of (Cohen *et al.* 1990) have particularly lead to recent controversy, with the study criticized on methodological grounds in (Hari *et al.* 1991, Williamson 1991). In (Therapeutics and Technology Assessment 1992) and (Anogianakis *et al.* 1992), the call is for a careful consideration of the absolute accuracies of either modality under conditions that are fair to both modalities. As noted in (Cohen and Cuffin 1983) and repeated in (Anogianakis *et al.* 1992), EEG and MEG provide complementary data, and the use of both modalities can contribute to overall improved accuracy.

Our analysis of dipole localization error for MEG and EEG is based on the well-known Cramer-Rao Lower Bound (CRLB). The CRLB provides a lower bound on the variance of *any* unbiased estimator of the location and other model parameters. By deriving a closed-form expression for the bound, we can compute it efficiently for a much wider range of conditions than can studies based on Monte-Carlo simulations or experimental data. The bounds are useful only if they are relatively tight (i.e. if they are not overly optimistic compared with the true localization error variances) and if the estimators employed have relatively small biases. To demonstrate the usefulness of the bounds, we present a Monte Carlo simulation which indicates that the CRLBs, in most cases, give reasonably accurate predictions of actual localization error variances.

We note that there are important limitations to this analysis, primarily due to the fact that the CRLB holds only under the assumption that the model is correct. The bounds give no insight into the effect of modeling error on localization accuracy. Nevertheless, in many of the cases shown, the CRLB gives surprisingly large lower bounds, even under fairly optimistic assumptions. Since modeling errors tend to degrade, rather than improve, performance, these results indicate that the accuracy of dipole localization

based on single time epochs is often limited by the inherent ill-posed nature of the problem. The models used here are some of the simplest in use. In general, more complicated models would be more prone to modeling errors and could have more parameters to estimate. Consequently, the bounds presented here may pose fundamental limits on EEG and MEG localization performance.

In this research, we present the Cramer-Rao lower bound for the general spatiotemporal model for an arbitrary number of sensors, an arbitrary number of time instances, and an arbitrary number of dipoles with arbitrary moments. We then present the formulas for the dipoles in a four shell sphere model for both the EEG and MEG case. These formulas are used in the subsequent sections to examine the lower bound on errors for several different array and dipole configurations. The localization error bounds are computed for one and two dipoles located in a plane in the upper hemisphere of the head. For each location, a search is performed over all possible dipole orientations to determine the best and worst results and the average localization error bounds. Graphical error contours are displayed for a quadrant in the upper-head hemisphere, providing rapid assessment and comparison of the two modalities.

Our emphasis is to present optimistic operating conditions with perfect models, many sensors, and low noise power, so that we may establish if the corresponding lower bounds indicate the potential for good dipole resolution. The use of identical sensor patterns allows, in each case, a cautious, but direct comparison of the differences in MEG and EEG source localization ability.

7.2 CRLB solution

The Cramer-Rao lower bound (CRLB) (e.g., Sorenson 1985) is an important result in estimation theory that establishes a lower bound on the variance of any unbiased estimator of a set of unknown parameters. Determining the bound requires a joint prob-

79

ability density function for the data. While the existence of an unbiased estimator that attains the bound is not guaranteed, we can use the bound to establish fundamental lower limits on the accuracy with which the parameters may be estimated. In applying the CRLB to dipole localization, we can use this result to determine, under certain modeling assumptions, minimum mean squared localization errors for dipolar sources. To demonstrate that these bounds are meaningful in this application, we need to show that (a) the estimators we use are effectively unbiased, and (b) the bounds are relatively tight, i.e., that the lower bound on the variance is close to the true attainable variance with a given estimator. To investigate the utility of the CRLB, we performed Monte Carlo studies using nonlinear least-squares for localization. The results of this study are reported in Section 7.3.

7.2.1 Derivation

Consider a set of data F, which we model as $F = G(\underline{l})Q + N$, where N is the unknown noise and $G(\underline{l})Q$ is the noiseless deterministic data. We assume that the locations $\underline{l}$ and the orientations and magnitudes Q of the dipole moments are unknown. We also assume that the noise N is zero-mean, spatially and temporally white, and normally distributed, and that it has an unknown variance v. For convenience, we group these parameters into one vector ψ,

$$\psi = \left[v, \underline{q}(1)^T, ..., \underline{q}(n)^T, \underline{l}_1^T, ..., \underline{l}_p^T \right]^T , \qquad \text{(EQ 53)}$$

where each moment vector at each time instance j is the concatenation of the individual moments for each dipole, as

$$\underline{q}(j)^T = \left[\vec{q}_1^T(j), ..., \vec{q}_p^T(j) \right] . \qquad \text{(EQ 54)}$$

Cramer-Rao Inequality Theorem: *Let $\hat{\psi}$ be any unbiased estimate of the deterministic parameters in $F = G(\underline{l})Q + N$. Then the covariance matrix C of the errors*

80

between the actual and estimated parameters is bounded from below by the inverse of **J**, *as*

$$\mathbf{C} = \mathbf{E} \{ (\psi - \hat{\psi}) (\psi - \hat{\psi})^T \} \geq \mathbf{J}^{-1} \qquad \text{(EQ 55)}$$

where **J** *is the Fisher Information Matrix*

$$\mathbf{J} = \mathbf{E} \{ \left[\frac{\partial}{\partial \psi} \log \ p(F| \psi) \right] \left[\frac{\partial}{\partial \psi} \log \ p(F| \psi) \right]^T \} . \qquad \text{(EQ 56)}$$

$\mathbf{E}\{ \ \}$ denotes the expected value or mean of the enclosed term, and $p(F| \psi)$ denotes the probability density function for the data with parameters ψ.

See (Sorenson 1985) for a proof of this result. The inequality in (55) states that the difference matrix $(\mathbf{C} - \mathbf{J}^{-1})$ is positive semi-definite, and as a consequence, the variance of each parameter ψ_i is individually bounded by the corresponding diagonal element in $\mathbf{J}^{-1}$. Under the assumption that the noise is spatially and temporally white and normally distributed, an closed form expression for (55) is possible. We derive below the Fisher Information Matrix and the corresponding Cramer-Rao lower bound for the general spatio-temporal model. We derive this result for the case of m sensors, n time instances, and p dipoles, in a general form that is applicable to both EEG and MEG data.

We define some notation and develop the bound to parallel the work of (Stoica and Nehorai 1989). We define **D** as the partials of the gain matrix G:

$$\vec{l}_k \equiv [l_{xk}, l_{yk}, l_{zk}]$$

$$d(l_{xk}) \equiv \frac{\partial}{\partial l_{xk}} G \ (\vec{l}_k)$$

$$d(\vec{l}_k) \equiv [d \ (l_{xk}), d \ (l_{yk}), d \ (l_{zk})]$$

$$\mathbf{D} \equiv \left[d(\vec{l}_1), \ ..., d(\vec{l}_k), \ ..., d(\vec{l}_p) \right] \qquad \text{(EQ 57)}$$

where l_{xk} refers to the x-axis component of the kth dipole location, and, similarly, for the other subscripts. Arrange the p moments at the jth time slice, $\underline{q}(j)$, into a block diagonal matrix,

$$X(j) \equiv \begin{bmatrix} I_3 \otimes \vec{q}_1(j) & & 0 \\ & \cdots & \\ 0 & & I_3 \otimes \vec{q}_p(j) \end{bmatrix},$$

(EQ 58)

where I_3 is a 3 x 3 identity matrix and " $\otimes$ " denotes the Kronecker product. (The Kronecker product of a (p x q) matrix $A = \{a_{ij}\}$ and an (m x n) matrix $B = \{b_{ij}\}$ is the (pm x qn) matrix, $\{a_{ij}B\}$, denoted by $A \otimes B$.)

With our parameters and their partials thus redefined into the matrices G, D, and X, we group these together into two more matrices before deriving the Fisher Information Matrix. This notation also simplifies the expressions for inverting the FIM to obtain the lower bounds:

$$\Gamma \equiv \sum_{j=1}^{n} [(DX(j))^T (DX(j))]$$

$$\Delta(j) \equiv G^T D X(j)$$

(EQ 59)

$$\underline{\Delta} \equiv [\Delta(1)^T, ..., \Delta(n)^T]^T$$

Thus, for m sensors, n time slices, additive zero-mean white noise with a variance v, and the dipole moments and locations grouped as defined above, the Fisher Information Matrix is (Stoica and Nehorai 1989)

$$J = \frac{1}{v} \begin{bmatrix} \dfrac{mn}{2v} & 0 & 0 \\ 0 & I_n \otimes G^T G & \underline{\Delta} \\ 0 & \underline{\Delta}^T & \Gamma \end{bmatrix}.$$

(EQ 60)

The three diagonal elements represent the information content of the scalar noise variance, the set moment parameters, and the set of location parameters, respectively. The off-diagonal terms represent the cross-information between the various parameters. With this partitioning and with the use of standard matrix inversion formulas (Sorenson 1985), we can readily invert this matrix analytically. We are particularly interested in the diagonal elements, since the Cramer-Rao lower bound for the ith parameter ψ_i is simply the ith diagonal element of J^{-1} (Sorenson 1985).

The off-diagonal zero elements in J make the lower bound for the scalar noise variance particularly easy to calculate:

$$CRLB(v) = \frac{2v^2}{mn} .$$ (EQ 61)

where CRLB( ) denotes the Cramer-Rao lower bound on the error covariance matrix of the enclosed vector. The lower bound covariance matrix for all p locations in $\underline{l}$ is found in the lower 3p x 3p portion of matrix J^{-1},

$$CRLB(\underline{l}) = v\left[\Gamma - \underline{\Delta}^T\left[I_n \otimes (G^T G)^{-1}\right]\underline{\Delta}\right]^{-1} .$$ (EQ 62)

Simplifying using (59),

$$= v\left[\sum_{j=1}^{n} (DX(j))^T (DX(j)) - \right.$$

$$\left[(DX(1))^T G \ldots (DX(n))^T G\right] \left[I_n \otimes (G^T G)^{-1}\right]\begin{bmatrix} G^T DX(1) \\ \ldots \\ G^T DX(n) \end{bmatrix}\right]^{-1},$$ (EQ 63)

$$= v\left[\sum_{j=1}^{n} (DX(j))^T I (DX(j)) - \sum_{j=1}^{n} (DX(j))^T G (G^T G)^{-1} G^T DX(j)\right]^{-1},$$ (EQ 64)

$$= v \left[\sum_{j=1}^{n} (DX(j))^T \left[I - G (G^T G)^{-1} G^T \right] (DX(j)) \right]^{-1} , \qquad \text{(EQ 65)}$$

$$= v \left[\sum_{j=1}^{n} (DX(j))^T P_G^{\perp} (DX(j)) \right]^{-1} , \qquad \text{(EQ 66)}$$

where $P_G^{\perp} = (I - GG^{\dagger}) = (I - P_G)$ is the orthogonal complement of the projection matrix for G, and $G^{\dagger}$ is the full rank pseudoinverse of G, $G^{\dagger} = (G^T G)^{-1} G^T$.

The lower bounds for the moment series at each time slice j can be readily expressed in terms of the lower bound for the location. If we define $\gamma \equiv CRLB(l)/v$, then the lower bound covariance matrix for *each* moment time slice j, j = 1,...,n is

$$CRLB(\underline{q}(j)) = v \left[(G^T G)^{-1} + G^{\dagger} DX(j) \gamma (G^{\dagger} DX(j))^T \right] . \qquad \text{(EQ 67)}$$

These formulas depend on inverting $G^T G$, and therefore a brief discussion about its rank is important. In the EEG and MEG cases studied in this research, we assumed that the dipole lay in the tangential plane, i.e., that the radial component was assumed known and equal to zero. Since G comprises submatrices G_i for each dipole, then each G_i must be appropriately expressed as a 2 x 2 matrix, before attempting the inverse of $G^T G$. If $G^T G$ becomes singular for a particular selection of dipoles, then the inverse is undefined, and we cannot calculate the variance. The reduced rank Moore-Penrose pseudoinverse is inappropriate here.

The Fisher Information Matrix and its inverse provide insight into how each parameter affects the estimate of the other parameters. Repeating (60), for m sensors, n time slices, and variance v, the Fisher Information Matrix is

$$J = \frac{1}{v}\begin{bmatrix} \begin{bmatrix} \dfrac{mn}{2v} \end{bmatrix} & 0 & 0 \\[2mm] 0 & \begin{bmatrix} I_n \otimes G^T G & \underline{\Delta} \\ \underline{\Delta}^T & \Gamma \end{bmatrix} \\ 0 & \end{bmatrix} \cdot \qquad\qquad \text{(EQ 68)}$$

The upper-left diagonal term in J, $(mn)/(2v)$, represents the information for the estimate of the noise power. The other entries in the first column and first row represent the cross-information between the noise power and the other parameters of our model, namely the moments and locations of the dipoles; these off-diagonal elements are zero. The CRLB requires that this matrix be inverted, and these zeros allow us to partition the matrix into two separate submatrices and invert them separately. Thus, the noise variance submatrix cannot affect the parameters in the other submatrix. Of course, the other lower bounds depend on the noise variance (there is a scalar noise variance term leading the matrix), but whether or not we assume that we know the noise variance is irrelevant, because the submatrix inversion to calculate the moment and location lower bounds is the same whether we *estimate* the noise variance or *assume* it.

In contrast, the lower bounds on either the set of moment parameters or the set of location parameters depend on whether we estimate both sets of parameters or assume one set known. We represent the information for the moments and the locations in the lower right submatrix in (68). The cross-information between the moments and the locations is represented by the off-diagonal term $\underline{\Delta}$. If we assumed perfect knowledge of the moments, then the CRLB of the locations would reduce to the first bracketed term in (62). Similarly, if the locations are perfectly known, the CRLB for the moments would

reduce to the first bracketed term in (67). In the general dipole localization problem, we know neither the moment nor the location, and the second term in each of these CRLB equations shows that we cannot simply ignore the cross-information term $\underline{A}$. This cross coupling will always increase the error lower bounds, except in the rather specialized case of $P_G^\perp D = D$, i.e., where the partials matrix is completely orthogonal to the gain matrix. Thus, consideration of the estimation of both the moment and the location is critical to better lower bound accuracy.

7.2.2 Location Error Lower Bounds

Equations (61), (66), and (67) above are for the general multiple dipole spatiotemporal model. They express the lower bound for the variance, the dipole location, and the dipole moment. Our approach in this research is to focus on the variance of the dipole location error, since much MEG and EEG work emphasizes the ability or inability of the different modalities to locate the source of neural activity. To gain insight into the utility of the formulas and establish some basic lower bounds, we simplify the studies to the single time slice case and to the case of multiple dipole sources of equal scalar intensity Q. In this case, the scalar Q factors out and can be grouped with the variance of the noise. Equation (66) reduces to

$$\text{CRLB}(l) = v\left[(DX(1))^T P_G^\perp (DX(1)) \right]^{-1}. \qquad \text{(EQ 69)}$$

If we assume all dipoles to be of equal intensity Q, then $X(1)$ can be factored as $Q\hat{X}$, where $\hat{X}$ comprises just the orientations of all the dipoles, and we have dropped the single time index for convenience. Thus (69) can be factored as

$$\text{CRLB}(l) = \frac{v}{Q^2}\left[(D\hat{X})^T P_G^\perp (D\hat{X}) \right]^{-1}. \qquad \text{(EQ 70)}$$

86

Broadly speaking, D represents the matrix of partial derivatives of the gain transformation with respect to the locations, $\hat{X}$ represents the moment orientations scaled to unity, and $P_G^\perp$ is a projection operator onto the orthogonal complement of the column space of the gain matrix G. Equation (70) illustrates how the dipole intensity and the noise variance can be lumped into a single scalar ratio of the two values, v/Q^2, and that the moment orientation can be isolated into a single term $\hat{X}$. We can therefore easily scale our results for any desired noise power and moment intensity levels.

7.2.3 Best, Average, and Worst Dipole Orientation

For one dipole, the lower bound error analysis for EEG generates a 7 by 7 covariance matrix: one dimension for the noise variance, three dimensions for the moment, and three dimensions for the location. In the case of MEG, we only have two dimensions of the moment we can estimate, but in either case we always have three dimensions assigned to the location. If we use Cartesian coordinates for our location parameters, then the difference vector between our estimate of the location and the true location can be written as

$$\text{Location Error Vector} = [\ (x - \hat{x}),\ (y - \hat{y}),\ (z - \hat{z})\ ]\quad . \tag{EQ 71}$$

The corresponding 3 by 3 submatrix bounding the error covariance for these parameters would be

$$\text{CRLB}(\hat{l}) = \begin{bmatrix} \sigma_{xx}^2 & \sigma_{xy}^2 & \sigma_{xz}^2 \\ \sigma_{xy}^2 & \sigma_{yy}^2 & \sigma_{yz}^2 \\ \sigma_{xz}^2 & \sigma_{yz}^2 & \sigma_{zz}^2 \end{bmatrix}. \tag{EQ 72}$$

Independent of our choice of coordinate systems, this bounding matrix can be represented by an error ellipsoid. The major axes of the ellipsoid are found as the eigen-

vectors of the bounding matrix. The lengths of the axes are determined from the corresponding eigenvalues. The eccentricity of the ellipsoid indicates the directional bias that the error vectors will exhibit. Indeed, the minor axes of the ellipsoid represent the "preferred directions" discussed in (Cohen and Cuffin 1983). If we consider the errors in any direction to be equally important, then we can ignore this directional bias and, instead, focus on the scalar length of this error vector. The lower bound on the expected squared value of this length is the sum of the eigenvalues, or equivalently, the trace (sum of the diagonal elements) of the bounding matrix. Hence, at a given location $\vec{l}$ and for a given moment $\vec{q}$, we can define our scalar localization error bound in Cartesian coordinates as

$$\text{RMS Location Error:} \quad \sigma_l(\vec{l}, \vec{q}) = (\sigma_{xx}^2 + \sigma_{yy}^2 + \sigma_{zz}^2)^{\frac{1}{2}} \qquad \text{(EQ 73)}$$

which, physically interpreted, is the lower bound on the root mean square (RMS) length of the three-dimensional error vector given by (71).

We emphasize in (73) the dependency of this calculation on the moment of the dipole; different moment directions at the same location will generate, in general, different error ellipsoids. Since radial sources represent "silent sources" for MEG data, we have largely restricted our examination to sources lying in the tangential plane for both MEG and EEG data. This restriction also simplifies our analysis of the RMS location error, because the moment orientation can now be parameterized by the single parameter θ describing the angle the moment makes in the tangential plane.

For a given point $\vec{l}$, we can "scan" over all possible θ, observing the RMS location error. Fig. 27 presents such a scan for two different cases. We see a strong dependency on the dipole orientation for one situation and relatively little dependency for the other. We retain three values from these curves: the best (lowest) RMS error, the worst,

Error vs. Dipole Moment Angle
127 electrode arrays, Dipole at: x = 5cm, y = 0, z = 5cm

Angle of Tangential Dipole (deg.)
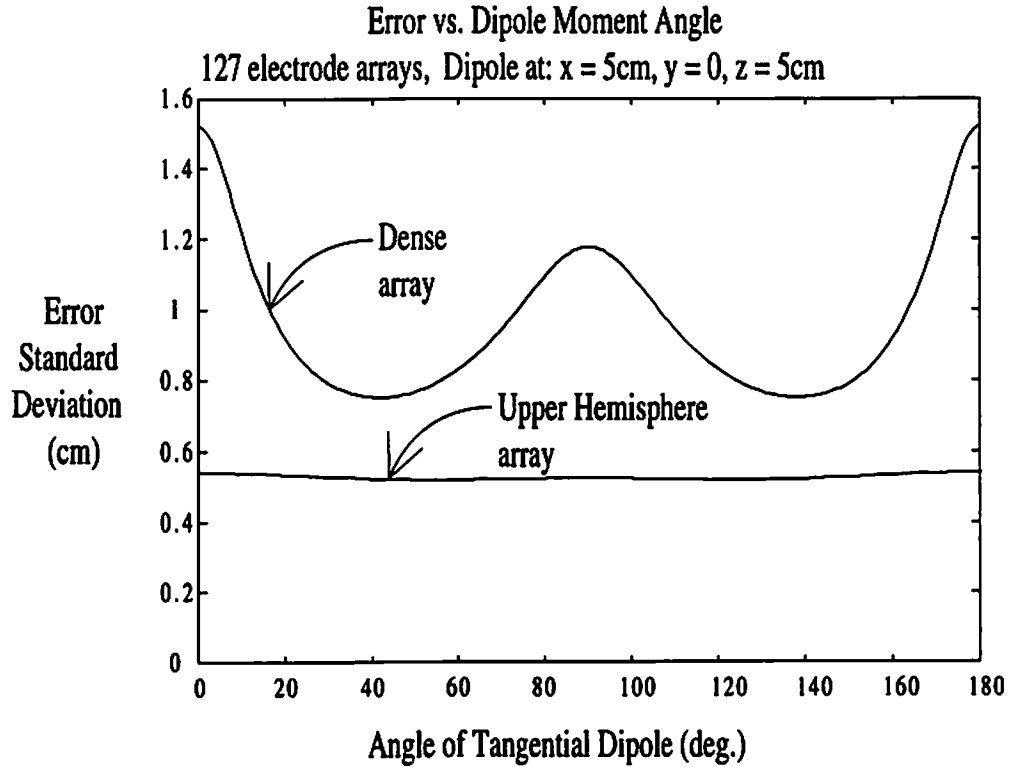
FIGURE 27. RMS Location error as a function of moment orientation angle. The moment direction was restricted to the tangential plane, because radial moments represent blind sources for MEG sensors. For each θ, the RMS location error is calculated using (70). This figure shows a comparison between two different sensor arrays for the same dipole location. The upper curve is for the dense 127-sensor pattern (see Fig. 31 for description), which is relatively more sensitive to the moment orientation, versus the lower curve for the 127 upper-hemisphere pattern (Fig. 29), which is insensitive to moment orientation. We retain three values from the curves: the best (lowest) error, the worst, and the average over all θ.

and the average over all angles. We illustrate in the examples to follow the sensitivity of some sensor patterns to dipole orientation.

For two dipoles, we extend the above approach. Since two dipoles represent six location parameters, we have a six-dimensional bounding matrix that represents all of the correlations between the parameters. If we focus on the error vectors that extend from the true locations to the estimated locations, we can still interpret the sum of the first three diagonal terms as the lower bound on the mean square error for the localization of the first dipole. The complexity is that each RMS error length depends on both

89

dipole moments and *both* locations. We can express these RMS values using the six

diagonal terms of the bounding matrix, expressed here in Cartesian coordinates as

$$\sigma_{\vec{l}_1}(\vec{l}_1, \vec{q}_1, \vec{l}_2, \vec{q}_2) = (\sigma^2_{x1x1} + \sigma^2_{y1y1} + \sigma^2_{z1z1})^{\frac{1}{2}}$$

$$\sigma_{\vec{l}_2}(\vec{l}_1, \vec{q}_1, \vec{l}_2, \vec{q}_2) = (\sigma^2_{x2x2} + \sigma^2_{y2y2} + \sigma^2_{z2z2})^{\frac{1}{2}}$$

(EQ 74)

If we again restrict the moments of both dipoles so that they lie only in the tan-

gential plane, we can parameterize these scalars as functions of angles for each moment.

For a given pair of dipole locations, $(\vec{l}_1, \vec{l}_2)$, we scan over all possible combinations of

θ_1 and θ_2 and again find the best, worst, and average RMS lengths for each dipole. In

general, the best orientation occurs when the two moments are arranged orthogonally,

such that the peak intensities of the dipoles are well separated in the field array. The

worst arrangement is for both dipoles to be aligned in the same direction, such that their

intensity peaks coincide and lie poorly across the array.

7.3 Monte Carlo Comparison

All of the results presented in this research represent the lower bound on the vari-

ance of the estimated location parameters for any unbiased estimator. In this section, we

present the results of a Monte Carlo simulation based on a standard least-squares esti-

mator for a 37 sensor MEG instrument. The full CRLB analysis assumptions are pre-

sented in Chapter 8 and the specific details of the 37 sensor arrangement are presented

in Section 8.1.4. We present the Monte Carlo results both to confirm the formulas and

to demonstrate the closeness of the CRLBs to the actual RMS error results from our

Monte Carlo study.

For each point on a 5 mm grid in a selected region of the upper positive quadrant of the x-z plane, we positioned a dipole in the best moment orientation as found by our CRLB analysis. We synthesized the single dipole forward model across the array using the same dipole intensity as in the analysis. For each grid point, we ran 5000 realizations of zero mean white Gaussian noise at the sensors, using a random number generator with the same standard deviation as that used in the analysis. For each noise realization, we estimated the dipole location parameters using the Nelder-Meade nonlinear least-squares approach described in (Mosher *et al.* 1992). We initiated the search within a 10 mm region around the true location to enhance the possibility of finding the global minimum and to avoid converging, instead, into a local minimum.

From these trials, we calculated the mean and RMS location error at each grid point. The mean location error for 95% of these grid points was less than 0.07 mm. This indicates that the nonlinear least-squares estimator is effectively unbiased for this single dipole case. The RMS location errors were observed to be greater than or equal to the CRLBs, within normal experimental variation. We then continued the Monte Carlo analysis for a larger region in the upper head quadrant, restricting our repetitions to 100 trials per grid point. Fig. 28 presents the RMS location errors and the corresponding CRLB results. In all regions where the anticipated standard deviation is less than a few centimeters, we see excellent agreement between the Monte Carlo and CRLB results. The overall result is a confirmation of both the MEG CRLB formulas and evidence that the least-squares estimator comes very close to meeting the CRLB.

At a 5 mm spacing, the MEG Monte Carlo simulations here required many days of computation on a Sun SPARCstation 2 computer, because each of the error trials could require many hundreds of calls to the generating function, and because at each point in the grid, we perform 100 or 5000 trials. The equivalent EEG model would require an order of magnitude greater processing time, because of the greater complexity

Best std.dev.(cm),tang dipole 4 sphere, 37 MEG sensors

Monte Carlo RMS vector length(cm), tang dipole 4 sphere, 37 MEG sensors
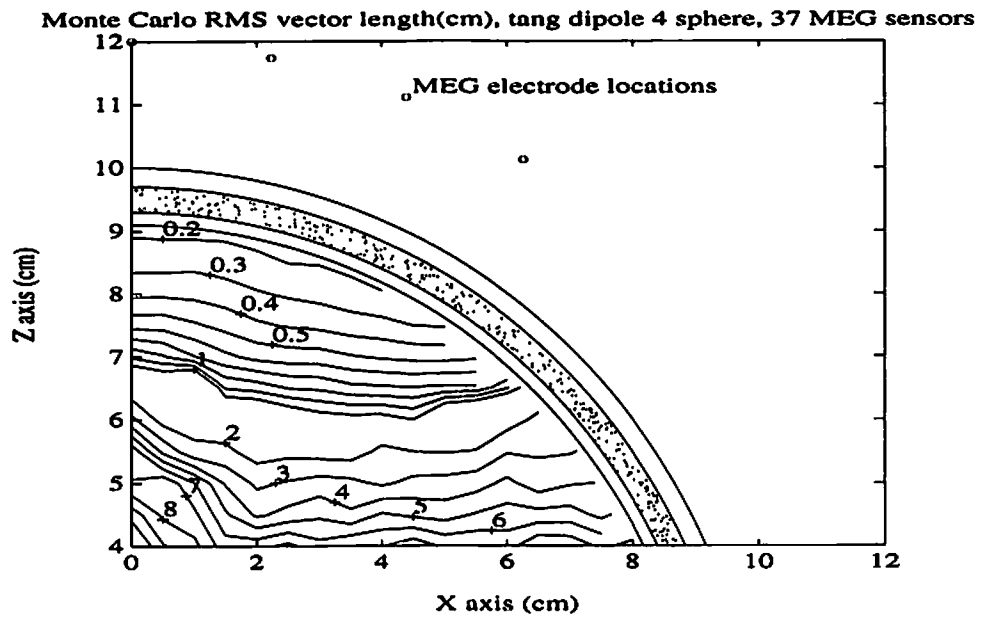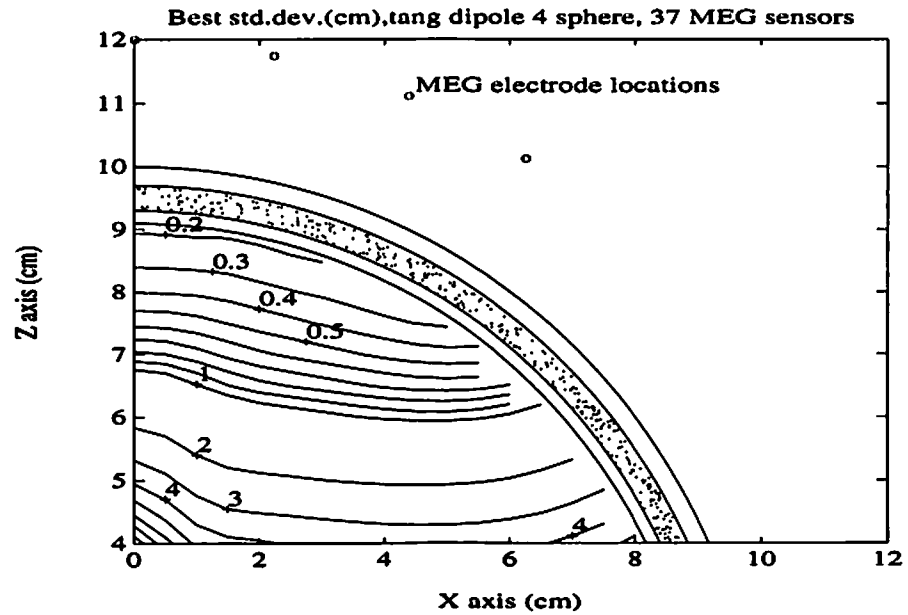
FIGURE 28. Monte Carlo simulation and comparison. The top figure shows the computed CRLBs for a single dipole in a 37-channel MEG system. The bottom figure is the result of a 100-trial Monte Carlo simulation at each point in a 5 mm grid, using the same dipole intensity and noise variance as was used in the CRLB analysis. The dipole was oriented in the "best" direction, as found from the CRLB analysis. In deep regions, the signal received at the array is much weaker than the additive noise, and the Monte Carlo runs experienced difficulty converging. In the shallow head regions, the signal at the array is improved, and we see excellent agreement between analysis and simulation.

92

of its gain transfer function. This computational burden for a single Monte Carlo study, with a single dipole orientation, underscores the utility of the CRLB calculations in more rapidly assessing many sensor arrangements and all dipole orientations.

Chapter 8

Applications of CRLB

8.1 MEG and EEG

8.1.1 Parameter Assumptions

Analysis Region

The formulas presented in Chapter 3 for the dipole in a four concentric sphere model are the general formulas for arbitrary sphere radii, tissue and skull conductivities, sensor and dipole locations, and dipole intensities and orientations. The CRLB formulas presented also apply for the general spatiotemporal model. Here, we restrict our numerical analysis to a few relatively simple cases of symmetric array patterns and one or two dipoles. The CRLB formulas require that the partial derivatives of the gain matrix with respect to the unknown location parameters also be calculated. The tedious calculations for the EEG model were carried out by hand by Michael E. Spencer, and verified using Maple V, a symbolic algebra computer program. The MEG partials were straightforward.

Figure 6 on page 28 displays one of the array patterns used here with relation to the spherical model. The other patterns were similarly symmetric about the z-axis, which runs through the center of the array. Because of this high degree of symmetry, we restrict our analysis region to the positive x-z plane. The error results in this plane can then be inferred by symmetry for the entire upper hemisphere. As this analysis plane is rotated about the z-axis, differences will arise because of the finite spacing of the sensors; however, these differences are not anticipated to be great.

Dipole Orientation

One of our goals in this study was to allow careful and cautious comparisons between EEG and MEG data. For the simple dipole in a sphere model used here, the radially oriented dipole generates no external magnetic field, so EEG holds an obvious advantage. We therefore restricted the orientation of the dipole to lie in the tangential plane for both the EEG and MEG data for most of the following error analyses. This restriction also simplified the parameterization of the dipole orientation to the single parameter θ, the angle the moment makes in the tangential plane. We note that this is not unduly restrictive, since all of the results presented here scale with dipole intensity Q. In the case of MEG data, a dipole with a radial component and an intensity Q would simply project into the tangential plane as a dipole with intensity $Q \cos\phi$, where ϕ is the angle made by the dipole with respect to the tangential plane. All of the standard deviations for the MEG data presented here could then be appropriately scaled to include any desired radial component. For comparison we also present some EEG results in which we place no restriction on the dipole moment orientation; the results are similar to those from the tangential dipole study.

Dipole Intensity

The bounds presented in (70) could be normalized to the ratio v/Q^2, but these units of sensor noise variance v to dipole intensity Q are nonintuitive and give the user no relative feel for the absolute localization error. We therefore attempt to establish some realistic values for the dipole intensity, and in the next subsection, the noise variance. We note that this ratio can be viewed as a signal-to-noise ratio, defined here as SNR(dipole) = Q/σ, where σ is the standard deviation. By fixing the dipole intensity at Q, then moving this dipole about the upper hemisphere, the actual signal intensity received by the sensor array will vary, roughly, as the inverse function of the squared distance to the

array. Hence, if we consider a second definition, SNR(array), to be a function of the signal at the array (either an average across all sensors or at the peak field among all sensors), then we observe that SNR(array) will drop as the dipole is moved deeper. Maintaining the SNR(array) as a constant over all dipole locations requires deeper dipoles to have correspondingly stronger intensities.

Variations of SNR(array) are common definitions in other studies, including (Cuffin and Cohen 1979, Cuffin 1986, Mosher *et al.* 1990, Oshiro *et al.* 1992), in which it is therefore not necessary to assign explicit units of amps to the dipole current. In such studies, all of the calculations are carried out in "relative units," where the signal at the array is set to one unit and the noise standard deviation is set to some ratio of this unit, for instance, 10 percent. We argue that the alternative SNR(dipole) is the preferred definition when the intent is to study the location error for a dipole or sets of dipoles arbitrarily located in the head. For SNR(array), adjusting the dipole intensity as a function of location will lead to distorted comparisons between different array configurations, because dipole intensity implicitly becomes a function of sensor location, and, in this study, a function of sensor type (EEG or MEG). Deeper dipoles may also be assigned unrealistically high currents simply to keep the SNR(array) constant. A fixed dipole intensity at a physically plausible current leads to a more informative accuracy analysis and to more direct comparisons between configurations.

In (Cohen and Cuffin 1983), a relatively strong dipole was estimated to have a dipole intensity of 2.1 μA-cm (21 nA-m). In (Cohen *et al.* 1990), an implanted dipole of 16 mm length was stimulated with 4 μA current, for an equivalent 64 nA-m current dipole. We wished to establish a baseline dipole intensity of the proper order of magnitude that was readily scaled to other intensities, and that appeared physically plausible. We selected 10 nA-m as our dipole intensity. With this selection, we can present accu-

racy bounds in units of meters, but we emphasize, however, that all of the examples presented can easily be rescaled to any other choice of dipole intensity.

Noise Variance

The selection of a standard deviation for the noise is not immediately obvious, in part because of the widespread practice of averaging experimental data. In theory, we could average the trials until the noise is reduced to any arbitrary low value. In this EEG/MEG comparison, the noise standard deviation is in units of either volts or teslas, respectively; thus we cannot easily set a standard deviation general to both sensor types as we did with the dipole intensity.

A dipole of intensity 10 nA-m near the cerebral spinal fluid layer can generate a field that peaks roughly at 350 fT in MEG sensors, or at 4 μV in nearby EEG sensors, for the sensor patterns and model examined in this chapter. In research such as that of (Cuffin 1986), the standard deviation is expressed as a percentage of the peak, approximately 10 percent. This definition roughly translates into similar SNRs examined in (Westerkamp and Aunon 1987, Stok 1987, Achim *et al.* 1991). We therefore, somewhat arbitrarily, set the MEG noise standard deviation to 35 fT and the EEG noise standard deviation to 0.4 μV, to reflect this 10:1 ratio. We compare with (Balish *et al.* 1991), who had a stated noise level of 50 fT after averaging 200 trials. We note the difficulty in extracting absolute noise levels from other reports for comparison because of the widespread practice of normalizing the noise standard deviation into the field levels. As with the dipole intensity, we emphasize that all of the examples presented can easily be rescaled to any other choice of noise variance.

Sensor Assumptions

In all cases, the EEG sensors are assumed to be affixed directly to the 88 mm scalp sphere, and they acquire an absolute voltage potential referenced to "infinity." In reality, EEG measurements are acquired as differential measurements with reference to a common local sensor or adjacent sensors. Here, however, we ignore this common use of a "switching" matrix. We also ignore the physical diameters of the sensors and assume that they make a point voltage measurement.

The MEG coils are placed 105 mm from the head center, representing a 17 mm offset from the scalp surface. This distance was chosen to represent the Dewar wall thickness of the larger sensor arrays and the air gap, both of which prevent the placement of the coils closer to the subject's scalp. Although these coils are often 20 mm in diameter, we also assume that they make a point magnetic field measurement and that they are oriented in the radial direction. (Jeffs *et al.* 1987) showed that this practice is a reasonable approximation by comparing point models with integrations across the coil diameters. Since most MEG sensors are arranged in a first or second order gradiometer configuration to control external field noise, we ran a CRLB comparison between a perfect point measurement and a perfect first order gradiometer, with a coil baseline separation of 50 mm. Our CRLB results for a 37 channel comparison showed that the only differences were minor, in the deep regions of the upper hemisphere. Thus, to simplify the comparisons, we ignored any considerations of gradiometers for the MEG examples presented here.

Array Patterns

The sensor array patterns presented here are identically arranged in angular separation for both the EEG and the MEG cases, and they were designed to mimic possible MEG sensor patterns because MEG sensors are much larger than EEG probes. Although

98

EEG probes are much smaller, they, too, have practical limitations in placement, because gels may form salt bridges for electrodes spaced too closely. In the following examples, we present the error lower bounds for 127 sensors spread first over the entire upper hemisphere and then densely in one region. We then present, for comparison, the results for just 37 sensors arranged in an array pattern similar to that of commercially available 37 sensor MEG instruments. The 127 sensor dense pattern was chosen to cover the same spatial area as a 37 channel system. We also present, for comparison, the accuracy bounds of the standard EEG Ten-Twenty array pattern, which provides a wide spatial coverage, similar to the 127 upper hemisphere pattern presented, but at a much more sparse spatial sampling.

The overall emphasis is to show which accuracies are possible for the wide spatial coverage or the dense local coverage, or the accuracy achievable with an array pattern similar to that of existing technologies or practices. Direct comparisons among different EEG and different MEG patterns are warranted, since dipole intensity and noise were held constant; however, comparisons between EEG and MEG results must consider the differences in noise assumptions and the uncertainties in model parameters. While our MEG model is relatively simple, the equivalent simple EEG model depends on many more assumptions of conductivities and sphere radii.

8.1.2 Upper Hemisphere 127 Sensor Pattern Results

We designed a simple pattern to cover the entire upper hemisphere without placing the sensors too close together. The first sensor is placed on the z-axis, then six sensors are placed evenly around a circle 15 degrees down from the z-axis. The next ring is 30 degrees from the z-axis, along which are twelve sensors evenly arranged. The pattern is repeated at 15 degree intervals for a total of 6 rings, with the rings containing 6, 12, 18, 24, 30, and 36 sensors, respectively, for a total of 127 sensors. The last ring lies com-

pletely in the x-y plane, such that the entire array provides full upper hemisphere spatial coverage. The MEG sensors are oriented radially.

This pattern was chosen as a natural extension of commercially available 7 and 37 channel MEG sensor arrays. The sensors are spaced roughly two centimeters apart, which is about the diameter of a single MEG coil. EEG and MEG instruments are now in the design phases with roughly 100 sensors. The analysis here for 127 sensors should represent the potential accuracy of these new instruments when they are used for whole head coverage.

One Tangential Dipole

In the first study, we calculated the lower bound for a single dipole located anywhere in the positive x-z plane (y = 0). The dipole was stepped along at 1 mm intervals within the brain sphere. At each location, the moment angle was stepped in 1 degree increments from 0 to 179 degrees, and at each angle the RMS lower bound was calculated using (70). The average RMS lower bound was calculated over all 180 degrees, and the best and worst angles were located. At these extrema, either a minimization or a maximization algorithm was initiated to refine the estimate of the best and the worst RMS errors, respectively. Three different bounds were retained for each location point in the grid, representing the best, average, and worst RMS errors.

In this case, the best, average, and worst bounds were similar. Fig. 29 shows the average RMS results for the EEG and MEG cases as contours representing lines of equal RMS error. For much of the upper head region, the error curves are approximately concentric. For this upper hemisphere sensor pattern, the RMS lower bounds are primarily a function of radial depth and are largely independent of orientation. Since dipole sources oriented radially produce no external magnetic field, we see an increasing MEG error as the dipole's location approaches the center. In contrast, the EEG error near the

100

center flattens out, because this inner region is approximately equally located from all sensors. Near the surface of the sphere, both modalities exhibit similar changes in error as a function of radial depth.

Two Tangential Dipoles

We now examine the rapid degradation in performance that occurs by introducing a second dipole. For simplicity in examining the effect of an additional dipole on the localization accuracy of the original dipole, we fixed the location of the second dipole on the z-axis at z=7.5 cm, directly under the center of the array. Both dipoles had equal intensity Q, so all results are directly scalable to any other arbitrary intensity. By the symmetry of the location of the additional dipole on the z-axis, we can restrict our analysis region to the positive x-z plane and infer the results for the remainder of the upper hemisphere.

As in the single dipole studies, the first dipole was stepped along on a 1 mm grid within the positive x-z plane. At each location point, the angles of *both* of the dipoles were stepped in 10 degree increments from 0 to 170 degrees, resulting in a grid of 18 by 18 different angle combinations. For each angle pair, the RMS error bounds for the first dipole were calculated using (70). The average errors were then calculated from this two-dimensional grid of error bounds, and the best and worst angle pairs were found. At these grid point extrema, a Nelder-Meade simplex minimization or maximization algorithm was initiated to refine the estimate of the best or worst RMS error bounds.

Fig. 30 presents the best and worst orientation results for the EEG and MEG cases. These cases, unlike that of the single dipole, have a strong dependency on dipole orientation. A wide range of error is possible between the best and worst orientation pairs. In comparison with the one dipole case above, we note that the results do not differ much along the x-axis, because the additional dipole on the z-axis is far enough away

FIGURE 29. 127 upper hemisphere sensor case for a single tangential dipole, EEG (top) and MEG (bottom) Cramer-Rao lower bounds. The 127 electrode pattern consists of an electrode on the z-axis and six concentric rings separated by 15 degrees, consisting of 6, 12, 18, 24, 30, and 36 electrodes per ring, respectively. The 127 MEG sensors are arranged in the same angular pattern, but they are located 10.5 cm from the head origin. The contour lines are labeled with the standard deviation of the error (in cm). Linear scaling factors of $(\sigma_V/Q) = 40$ V/(Am) and $(\sigma_B/Q) = 3.5 \times 10^{-6}$ T/Am for the EEG and MEG cases respectively are assumed. These factors correspond to a noise standard deviation of 0.4 microvolts (EEG) or 35 femtoteslas (MEG) and a dipole strength (both cases) of 10 nanoamp meters. The plots show the average of the error bound calculations for the dipole orientation stepped in one degree increments around a full circle. Both the EEG and MEG results show little sensitivity to moment orientation for this pattern and single dipole. We emphasize that the curves can be linearly scaled for arbitrary σ/Q.

that it has little effect. As we follow along the inner radial cerebrospinal fluid layer, we see that the second dipole can affect the accuracy of the first dipole as far as 4 cm away, rapidly doubling the standard deviation error. In general, in the best moment orientation pairs, the two dipoles were pointed in orthogonal directions, so their corresponding field intensities across the array were separated better than at any of the other angle combinations. The worst orientations occurred when both dipoles pointed in the same parallel direction, so that their fields had the greatest overlap.

This study has presented only a few of the endless possible combinations for two dipole intensities and positions. However, this one study shows the rapid degradation in accuracy that occurs when trying to localize two equal intensity dipoles that are relatively well situated within the array. We also see that localization error is not simply a function of the relative distance between the two dipoles, but rather a complex function of absolute dipole position and orientation. We contrast this with the results in (Oshiro *et al.* 1992). Through a limited Monte Carlo analysis (Oshiro *et al.* 1992) erroneously claimed to show that the error is a only function of the distance between dipoles and does not depend on the orientation. While this may be true in specific instances, it is clearly not true in general. By comparing the best and worst standard deviation curves presented here, we see that their conclusion applies only to limited regions of the sphere. In general, the relative orientation between the two dipoles is very important.

8.1.3 Dense 127 Sensor Pattern

The upper hemisphere pattern examined above exhibits some variations near the inner surface of the cerebrospinal fluid, primarily because of the somewhat coarse 2 cm spacing of the sensors. Here we examine the same 127 probes, concentrated in a much smaller region, to observe more directly the effects of spatial sampling. The array was constructed as described in Section 8.1.2, with six rings of sensors; however, the spacing
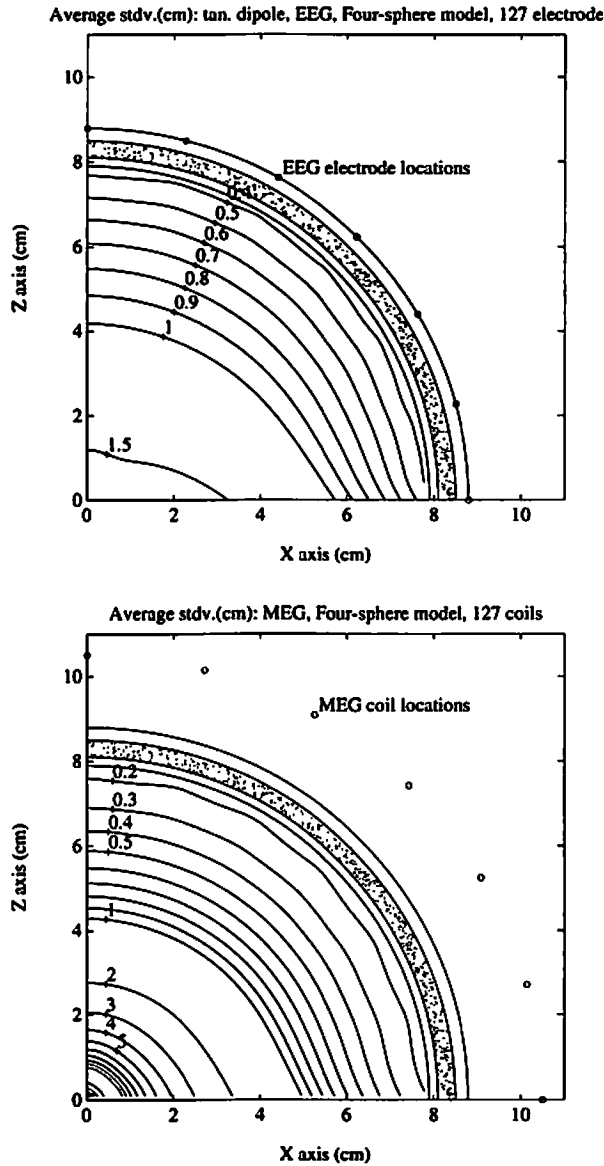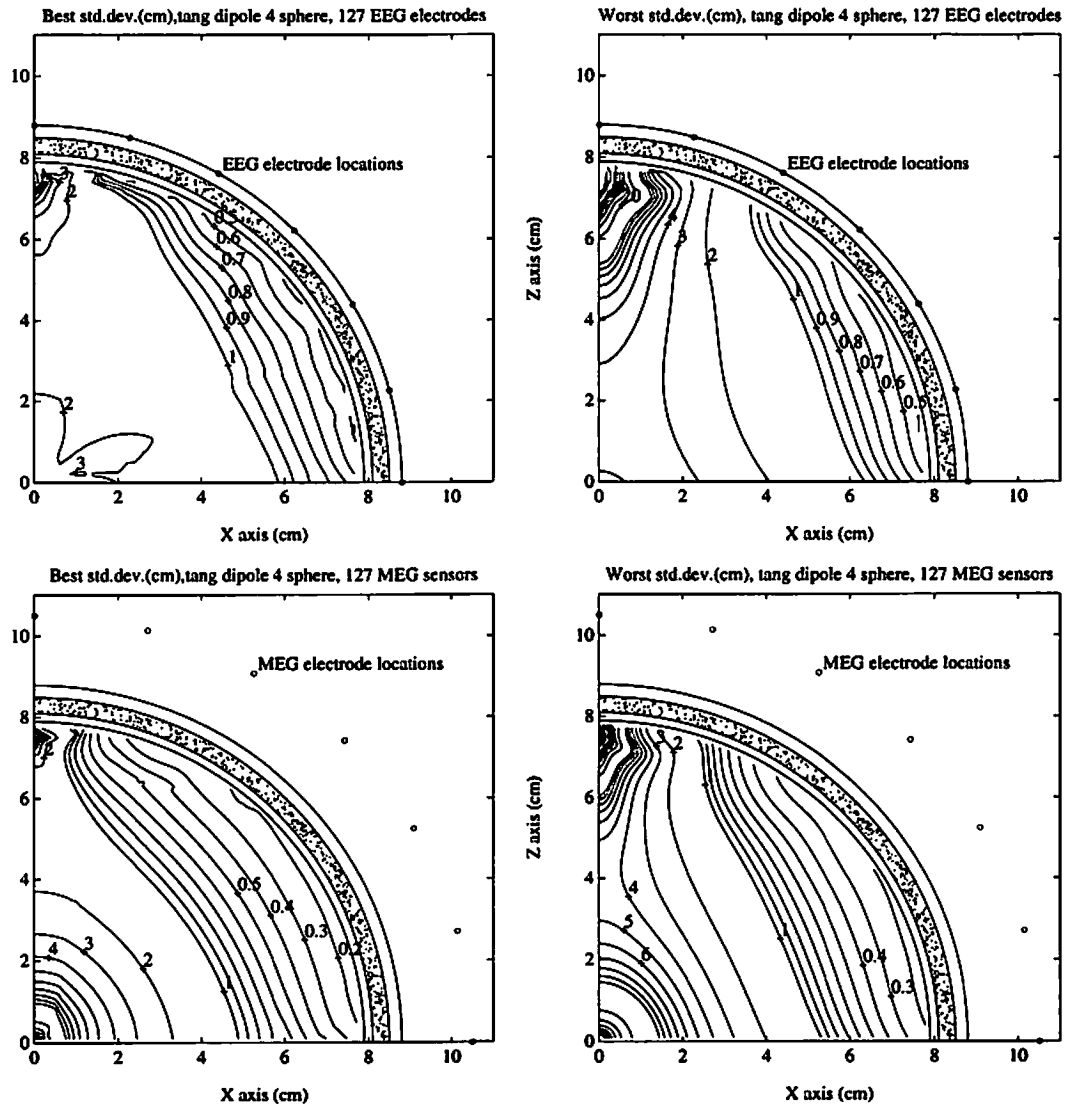
FIGURE 30. 127 upper hemisphere sensor case for two tangential dipoles, EEG (top) and MEG (bottom) Cramer-Rao lower bounds. The sensor pattern is identical to that of Fig. 29. The first dipole is at any given point in the positive x-z plane and the second is located on the z-axis at 7.5 cm. The contour level (in cm) is the RMS error bound of the first dipole because of the presence of the second dipole. Dipole intensity and noise levels are the same as in Fig. 29. The left-side figures show the CRLBs for the best possible orientation combination, and the right-side show the CRLBs for the worst.

between each of the circles and the z-axis was in 6 degree increments rather than 15 degrees. The MEG sensors were oriented radially. The result was an array that subtends a 72 degree angle, which is of approximately the same spatial coverage as that of commercially available 37 channel MEG instruments, but with a much denser spatial sampling. Here, the spacing is, in general, less than 1 cm between sensors, which would prove to be impossible for the larger MEG coils and daunting for the placement of surface EEG electrodes. Hence, this case might represent one of the densest patterns presently possible for either modality.

One Tangential Dipole

The analysis procedure here was identical to that of the 127 sensor upper hemisphere pattern. Fig. 31 displays the average RMS results for the EEG and MEG cases. Here we note the immediate impact of the limited spatial coverage on overall dipole accuracy, particularly on the increased sensitivity to moment orientation caused by the array edges. Directly under the array, where array edge effects are minimized, we see an overall factor of about two improvement in the variance, relative to the upper hemisphere array, because of the increased number of sensors in the proximity of the dipole. The error bound rises rapidly in the lower regions of the sphere because of the combined effects of the squared distance to the sensor array and the poor spatial coverage of the field peaks. This latter effect is most notable on the deeper dipoles located directly on the z-axis. By offsetting the deeper dipoles from the center of the array, we are able to position the peak of the field intensity such that it falls across the array, and achieve a slightly improved lower bound.

Comparing EEG and MEG results, we see that MEG suffers more rapidly in the lower regions as a function of the three effects of depth, proximity to the sphere center,

105

Average stdv.(cm): High density, EEG, 127 electrode

Average stdv.(cm): MEG, Four-sphere, 127 dense coils

FIGURE 31. Dense 127 sensor case for a single tangential dipole, EEG (top) and MEG (bottom) Cramer-Rao lower bounds. The array pattern is constructed as in Fig. 29 for the case of the 127 sensor upper hemisphere pattern, but is now separated by 6 degrees, instead of 15 degrees. Dipole intensity and noise levels are the same as in Fig. 29. The plots show the average RMS lower bound for all orientations. Increased sensitivity to moment orientation was noted near the edges of the array pattern. The increased sampling density gives better lower bounds than in Fig. 29, but only in a greatly reduced region of the head.

106

and poor spatial coverage. By comparison, EEG has a more gradually increasing error as a function of just the two effects of depth and coverage.

Two Tangential Dipoles

The analysis procedure here was identical to that of the two dipole study for the 127 upper hemisphere pattern. Fig. 32 presents the results of the two dipole study for the EEG and MEG cases. The lower bounds in the deep regions and regions outside of the array have risen sharply, compared with their one dipole counterparts. Compared with the two dipole 127 upper hemisphere pattern in Fig. 30, the increased sensor density in Fig. 32 allows the two dipoles to be placed somewhat closer together, but the edge of the array confines the region with low error bounds to a relatively small area.

8.1.4 Thirty-Seven Sensor Pattern Results

In this study, we arranged three rings of sensors, with each spaced in increments of 12 degrees from the z-axis and each containing 6, 12, and 18 sensors, respectively, for a total of 37 sensors, as displayed in Figure 6 on page 28. The MEG sensors were oriented radially. This pattern approximates that of commercially available 37-channel MEG instruments. We note that the upper hemisphere pattern for 127 sensors has a slightly coarser spatial sampling than this 37 channel pattern (15 degree spacing versus 12 degree), but the upper hemisphere pattern covers a much wider spatial area. The dense pattern with 127 sensors has the same spatial coverage as this 37 channel instrument at roughly twice the spatial sampling density (6 degree spacing versus 12 degree). Thus the 37 channel suffers in comparison with both poorer spatial coverage and spatial sampling.

Best std.dev.(cm),tang dipole 4 sphere, 127 EEG electrodes

Worst std.dev.(cm), tang dipole 4 sphere, 127 EEG electrodes

Best std.dev.(cm),tang dipole 4 sphere, 127 MEG sensors

Worst std.dev.(cm), tang dipole 4 sphere, 127 MEG sensors
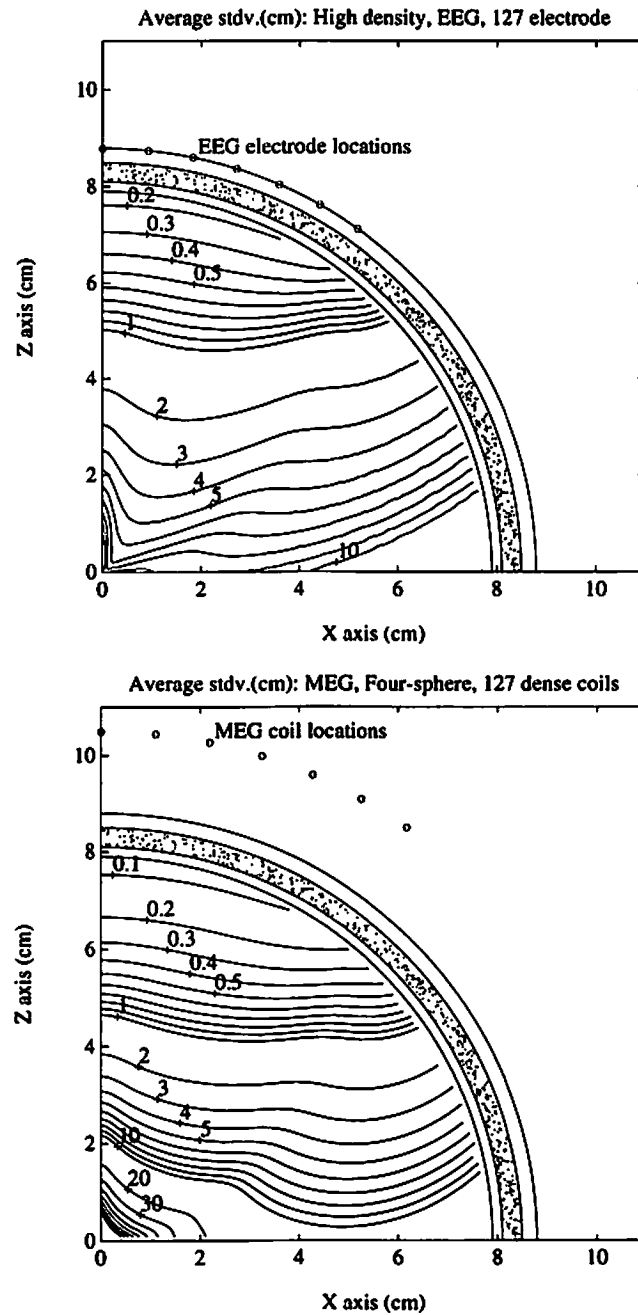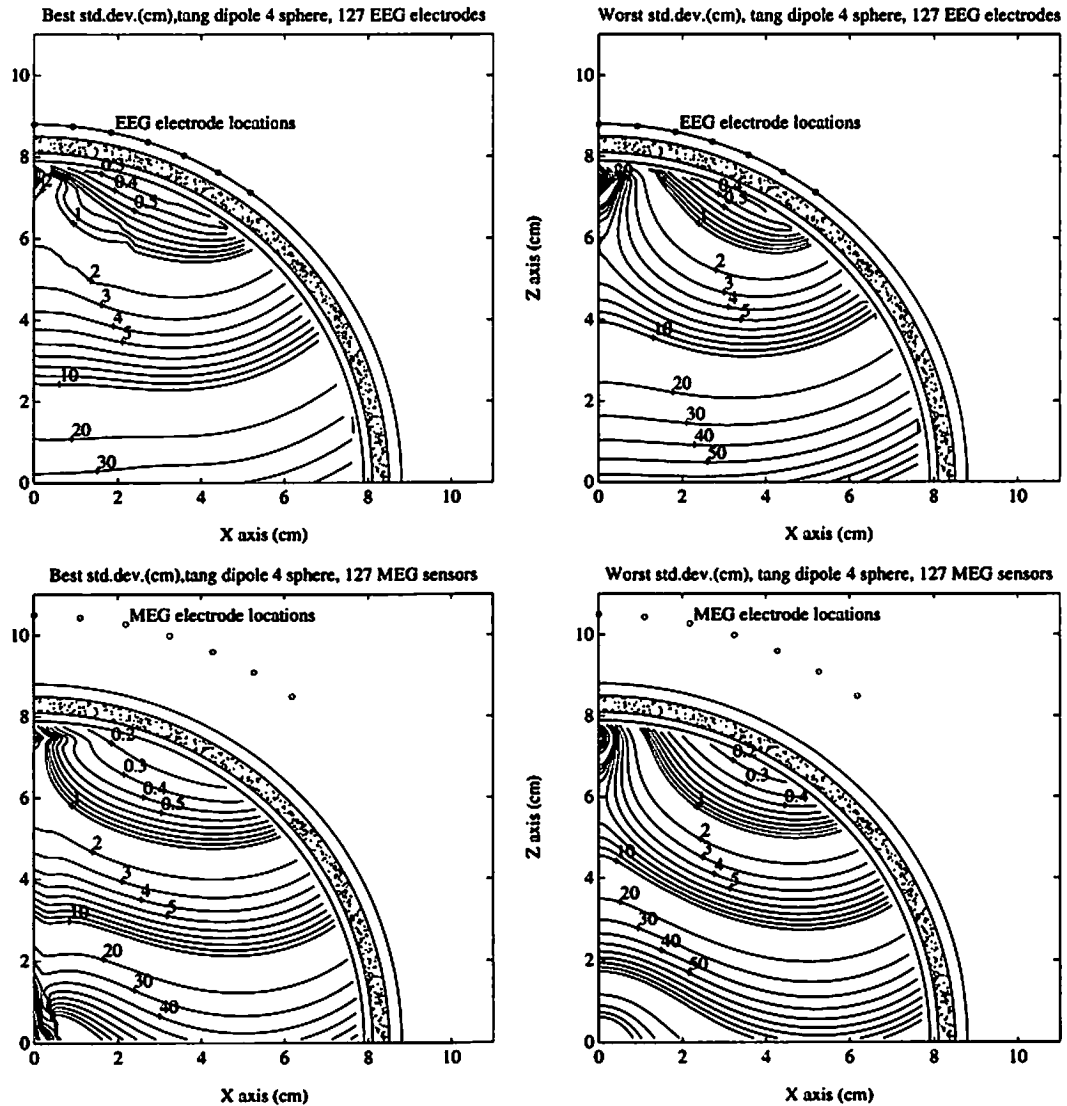
FIGURE 32. Dense 127 sensor case for two tangential dipoles, EEG (top) and MEG (bottom) Cramer-Rao lower bounds. The analysis procedure was identical to that in Fig. 30, but with the sensor pattern of Fig. 31. Compared with Fig. 30, the increased sampling density does allow the two dipoles to be placed more closely together, but only in a greatly reduced region of the head.

108

Single Tangential Dipole

The analysis procedure for the single tangential dipole was identical to that of the127 sensor upper hemisphere study. Fig. 33 (top) shows the average RMS EEG and MEG case for the single dipole restricted to the tangential plane. The accuracy directly under the array is comparable to that of the upper hemisphere array, but the accuracy declines much more rapidly as a function of depth. Also noticeable was a stronger dependency on dipole orientation, similar to that of the dense array above. The overall effect is a greatly reduced area directly under the array that has an accuracy comparable to that of the larger arrays.

Two Tangential Dipoles

The two dipole analysis procedure was identical to that of the 127 sensor upper hemisphere study. Fig. 33 (bottom) shows the average RMS EEG and MEG error bounds of a dipole when an additional dipole of equal intensity was placed on the z-axis at z=7.5 cm. We can see that, in almost all regions, the dipole's error bound is at least double that in the single dipole study. In the worst case, we also found that it is impossible to place two dipoles on the z-axis in the same orientation and still resolve them. This perfect array ambiguity is a consequence of the three perfectly symmetric rings of sensors. The general overall accuracy region is greatly reduced from that of either of the previous sensor patterns.

8.1.5 EEG Single Unconstrained Dipole

The dipole was restricted to the tangential plane in our other studies, so that comparisons could be made more readily between EEG and MEG results. In this study, we allow the EEG dipole to be unconstrained in orientation to study whether there was any significant improvement for the single dipole case. We used the same 37 sensor arrange-

Average stdv.(cm): tan. dipole, EEG, Four-sphere model, 37 electrode
Average stdv.(cm): MEG, Four-sphere model, 37 coils
Average stdv.(cm): two dipoles, EEG, Four-sphere model, 37 electrode
Average stdv.(cm): MEG, two dipoles, Four-sphere model, 37 coils
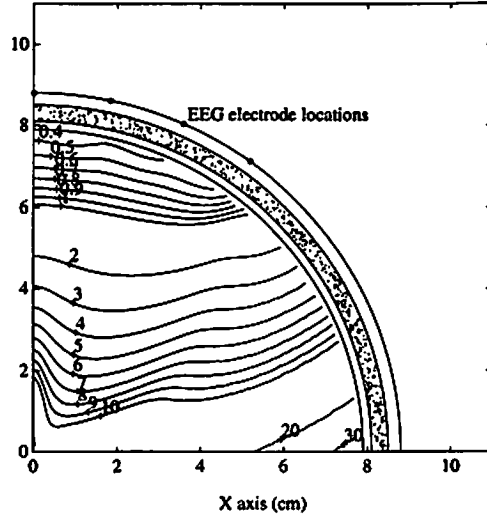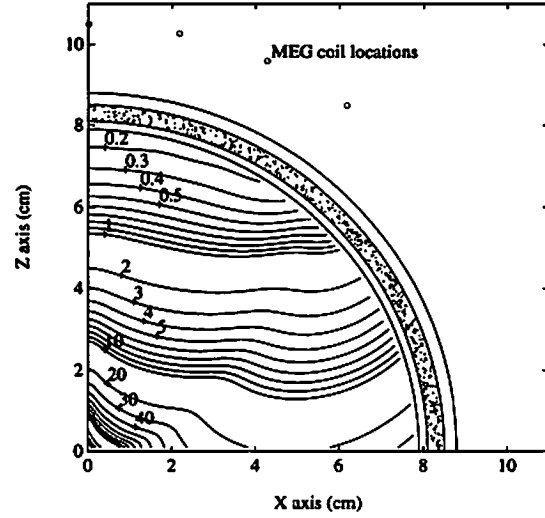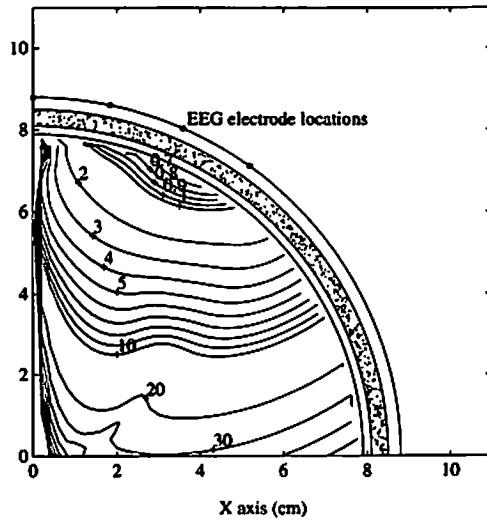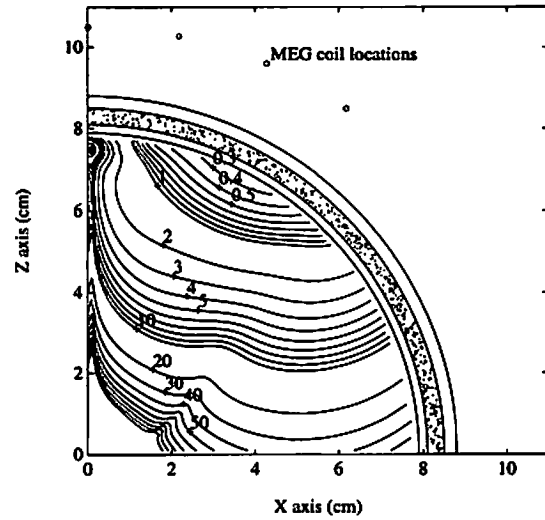
FIGURE 33. The 37 sensor case with a single tangential dipole (top) or with two tangential dipoles (bottom). EEG (left) and MEG (right) CRLBs are shown for any given point in the positive x-z plane. All plots show the average RMS lower bound. The analysis procedures and scaling factors were identical to those in Fig. 29 and Fig. 30. Compared with the 127 sensor studies, the combination here of relatively coarse spatial sampling and limited spatial coverage result in overall markedly poorer lower bounds.

ment, and at each location point, we calculated all possible combinations of radial and tangential moment orientations in 10 degree increments over the range 0 to 170 degrees. The minimization/maximization analysis was carried out in a manner identical to the two dipole studies above, except in this study the two angles were for the one dipole.

Fig. 34 displays the average EEG RMS error bounds for the single unconstrained dipole. In the near region of the array there was only a slight improvement of the best error bounds and a slight degradation of the worst error bounds, but on average, the results remained fairly consistent with those presented in Fig. 33. In the deeper regions, the relaxation of the tangential restriction allowed the dipole to swing into a radial direction and direct more of its surface potential across the array, thereby smoothing the error curves in these deeper regions; nonetheless, the error values are quite comparable to the tangentially restricted dipoles. Overall, the tangential restriction allowed for simpler studies, because the moment was a function of only one angle parameter, and this restriction does not appear to have degraded the localization accuracy for the single dipole case.

8.1.6 EEG Ten-Twenty Sensor Pattern Results

Since EEG data have historically been collected in the Ten-Twenty array pattern using 21 electrodes, we performed a study with this sensor pattern, which features wide spatial coverage and poor spatial sampling. Fig. 35 shows the average RMS results, again using the same analysis procedure as was used for the other studies. We note that a source directly underneath the sensor at approximately x=6 cm and z=6 cm shows no significant improvement in accuracy over radially deeper sources. Although a shallow source generates a significantly stronger signal at the surface, the spatial undersampling is such that only one nearby sensor receives a significant signal. One sensor cannot adequately locate the source, regardless of the source intensity. The deeper sources generate

111

Average stdv.(cm): free dipole, EEG, Four-sphere model, 37 electrode
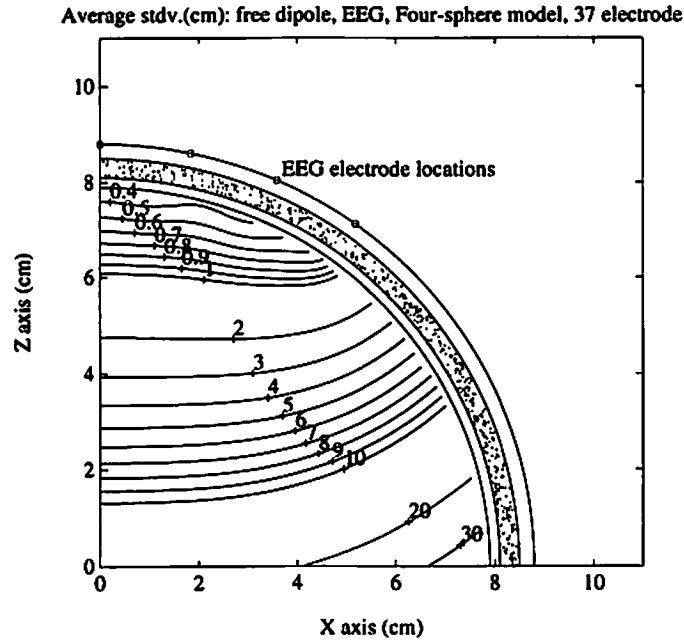
FIGURE 34. EEG CRLBs for the 37 electrode case and a single freely oriented dipole (the dipole can have tangential and radial components) at any given point in the positive x-z plane. The plot shows the average RMS lower bound for all possible dipole orientations. The dipole intensity and EEG noise level are the same as in Fig. 29. The tangential restriction used in Fig. 33 (top left) has little effect on the lower bounds in the regions near the sensors; the deeper regions show relatively inconsequential shifts.

a signal across enough surface sensors to compensate for their relatively weaker surface signal. The overall effect of this sparse array of sensors is a relatively flat and larger lower bound error surface compared with that of the other studies.

8.1.7 EEG and MEG Fusion

The field pattern generated by a dipole across an array of EEG sensors peaks roughly along the axis of the dipole moment. In contrast, the MEG pattern peaks to the sides of the dipole moment, roughly perpendicular to the EEG pattern. In this study, we assume that both the EEG and MEG data are acquired, and we observe the improvement generated from this diversity in the information content. The sensor pattern was the same as that in the 37 sensor system, except that here we have a total of 74 measurements for

112
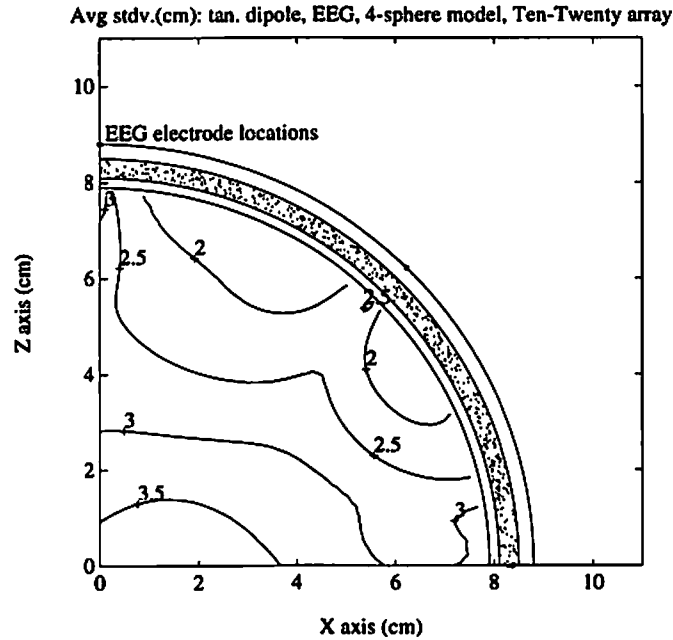
FIGURE 35. EEG CRLBs for the 21 electrode arrangement for the standard Ten-Twenty arrangement and a single tangential dipole at any given point in the positive x-z plane. The dipole intensity and EEG noise level are the same as in Fig. 29. The plot shows the average RMS lower bound for all possible dipole orientations.

the two combined sensor systems. The analysis procedure was identical to that in the other studies. Unlike the other studies, the results do *not* scale with arbitrary dipole intensity and noise variance, because both the EEG and MEG noise must be considered simultaneously. To bring the two modalities into relatively scaled units, we multiplied one of the arrays by the ratio of the two noise variances, which introduces a more complex relationship between standard deviation, dipole intensity, and noise variances.

Fig. 36 shows the bound for a dipole restricted to the tangential plane. In contrast with Fig. 33 for the same array pattern and respective noise variances, we note almost no difference among the best and worst moment orientations. Since the EEG and MEG arrays complement each other so well in their field patterns, the dipole always points in a direction that is captured well by one of the two arrays. In the regions directly below the center of the array, an improvement occurs simply because there is twice as many

113

measurement points. In the deeper regions, the EEG sensors have obviously improved the response near the center, and both sensor modalities have greatly improved the other deep regions.

This analysis confirms the hypotheses of (Cohen and Cuffin 1983, Anogianakis *et al.* 1992, Therapeutics and Technology Assessment Subcommittee 1992) concerning the potential for directly combining EEG and MEG measurements into an overall superior resolution ability, unachievable by either modality alone. One extension of this study would be to augment fixed MEG sensor arrays with a smaller array of EEG sensors to determine whether similar improvements could be obtained.

8.1.8 Discussion

The results presented in these exemplar studies focus on the single time slice problem, but the formulas presented for the CRLB are for the more general temporal problem. The CRLB formulas show the improvement achievable by considering multiple time slices, in which the sample spacing is large enough to decorrelate the noise. In the simplest case of the fixed dipole moment, the standard deviations are, at a minimum, improved by the square root of the number of time slices. This effect is analogous to signal averaging over time. If the time series of the dipole moments have any algebraic independence, the results are improved further. An addition to the formulas would be the inclusion of the fixed moment dipole model, which would improve the lower bounds by incorporating the knowledge that the dipole does not "rotate"; however, the "rotating" formulas presented here are more general. The work of (Baumgartner *et al.* 1991, Achim *et al.* 1991) may have benefited from using these spatiotemporal CRLBs as a rapid analysis tool in interpreting their specific case studies of dipole locations and time series.

The RMS errors presented in this study do not consider the directional bias that could occur. In the case of EEG and MEG, with data measured from external sensors

Best stdv.(cm): EEG/MEG fused, 37 electrodes and 37 coils

Worst stdv.(cm): EEG/MEG fused, 37 electrodes and 37 coils
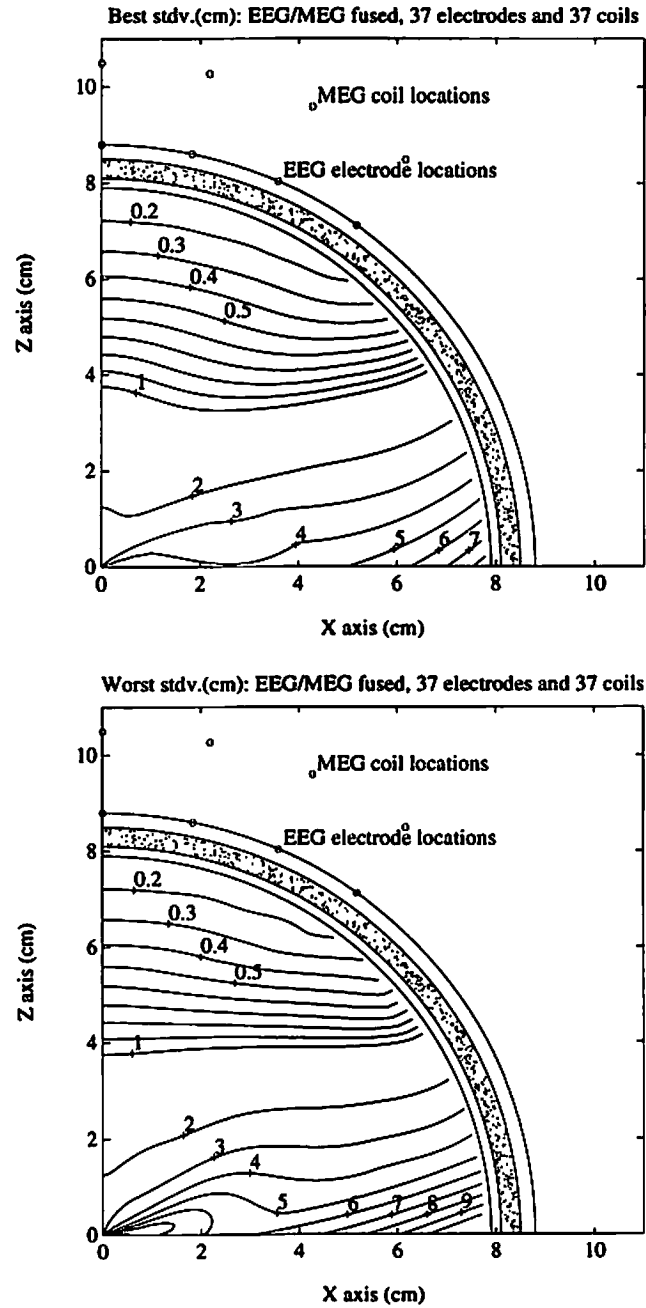
FIGURE 36. Combined EEG/MEG CRLBs for the 37 electrode and 37 magnetic sensor array and a single tangential dipole at any given point in the positive x-z plane. As in the other studies, $(\sigma_V/Q) = 40$ V/(Am), $((\sigma_B/Q) = 3.5 \times 10^{-6}$ T/Am) ; however unlike all other results presented in this chapter, these results do *not* scale linearly with other values of noise variance and dipole intensity. The best and worst moment orientations are presented in the left and right plots, respectively. Compared with Fig. 33 (top), notable here are the greatly improved lower bounds and the lack of any appreciable sensitivity to dipole orientation.

115

(i.e., no invasive probes), the greatest localization error will, in general, be in the radial direction, because the tangential directions are more accurately measured by the surface arrays (the "preferred directions," as noted by (Cohen and Cuffin 1983)). If we were to model the cortex as a simple thin shell beneath the skull, we might be able to ignore this radial error; the tangential errors were in general much smaller. In reality, the cortical folds (analyzed in some detail in (Kaufman *et al.* 1991)) also force consideration of the radial location of the dipole. In the absence of any prior information regarding the importance of one direction over another, we argue here that error in all directions is equally important.

The approaches presented here will also assist in the analysis of novel sensor locations, orientations, and parameter sensitivities by providing a preliminary CRLB baseline. We emphasize that while small CRLB bounds will not guarantee that such standard deviations will ever be achievable, large CRLB bounds will steer us clear of situations where the desired accuracy would be impossible.

8.2 Thunderstorm Localization

To motivate the utility of the CRLB equations for the NASA KSC problem, we specialize the analysis here to a few relatively simple cases of one or two sources. By examining such simple cases, the attempt is to infer the relatively worse accuracies possibly encountered with more complicated models.

8.2.1 Point Charge

In this study, a point charge is moved about the KSC area at fixed altitudes of 1000 and 6000 meters. We examine the horizontal and vertical error in locating such a charge. Fig. 37 presents the results for the charge at 1000 meters. The top figure shows the lower bound on the root mean square (RMS) error in locating the source in the hor-

izontal plane. We have isolated out and plotted separately the vertical component in the bottom figure. Horizontally, we see excellent lower bounds within the cape, with rapidly increasing bounds outside the cape. This kind of result is consistent with the well known problem of attempting to *extrapolate* beyond the bounds of your data. The sources within the cape represent loosely *interpolation*, a more accurate approach in general. We note that the vertical lower bounds are roughly a factor of ten higher. This preference to the horizontal directions is a consequence of all sensors lying in the plane of the earth. We could anticipate reduced vertical bounds if some sort of airborne sensor were in place.

Fig. 38 presents the same situation for the charge at 6000 meters. Here we see much broader lower bound surfaces, in contrast to the 1000 meters. This smoothing is a consequence of the charge not being too close to a single ground sensor, but rather being high enough to be accurately located by several sensors.

We emphasize that the linearity of the parameters allows the user to arbitrarily scale our results to any desired ratio of noise standard deviation versus dipole intensity. Thus these graphs are not necessarily specialized to just the 10 coulomb, 10 volts standard deviation presented here.

8.2.2 Two Positive Charges

Two equal positive charges are placed at 6000 meters, then moved about the area. We examine the horizontal and vertical error in still locating the 6000 meter charge in the presence of a second charge. Fig. 39 presents the results, which can be compared with Fig. 38 for the same charge. Here we see the "jamming" influence the second source at 10,000 meters has in locating the original source. The vertical error has particularly climbed. We interpret this result to say that attempting to model a storm cell as two isolated charges may prove difficult in many regions of the cape, if we insist on

117
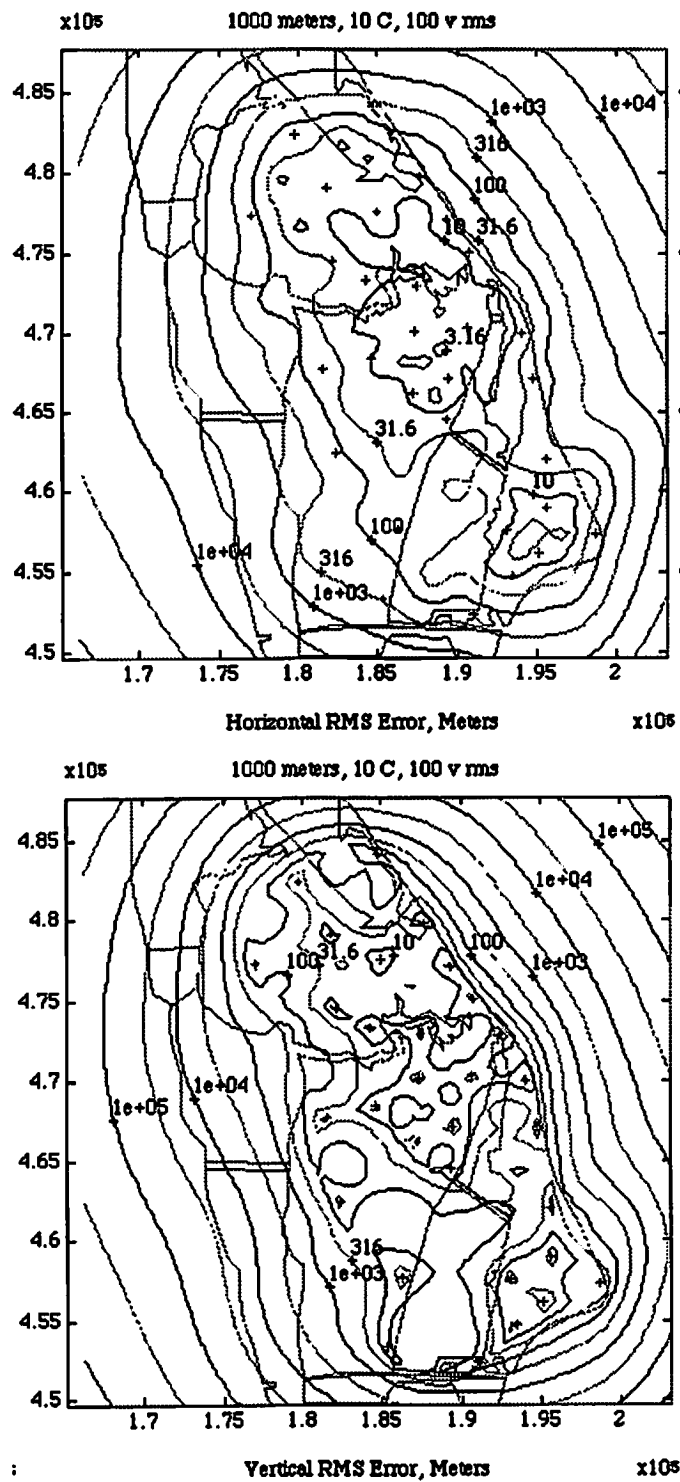
FIGURE 37. Point charge at a fixed altitude of 1000 meters. The top figure represents the lower bound on the horizontal error, and the bottom figure is the lower bound on the vertical error. Values represent the one standard deviation in meters.
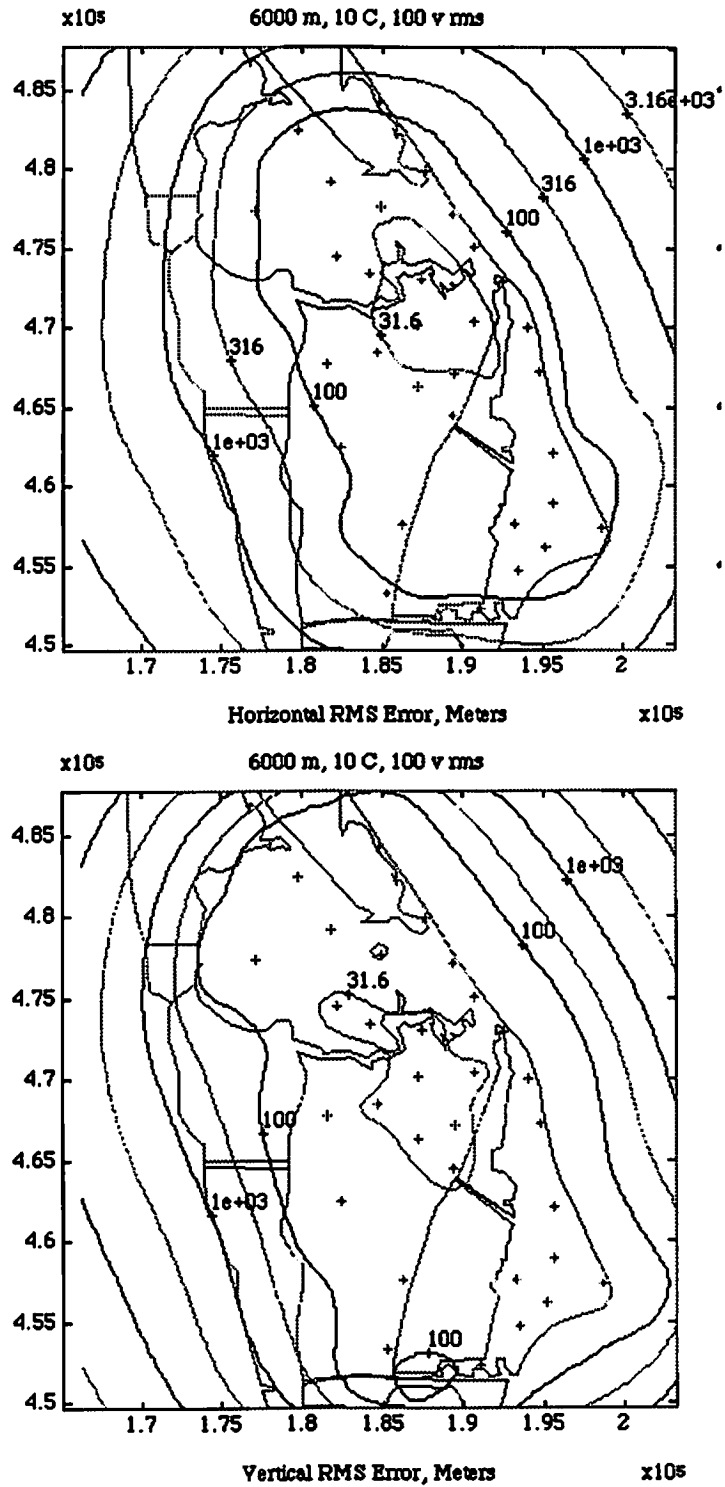
FIGURE 38. Point charge at a fixed altitude of 6000 meters.

identifying each charge individually. The situation worsened dramatically when we modeled a triple charge air mass, with the bottom charge at 2,000 meters suffering very large error bounds.

The Cramer-Rao bound shows us (1) that within the KSC array the possibilities are excellent for good localization for simple storm models, and (2) that outside the array the possibilities are poor. In other words, attempting to accurately localize storm cells over the Atlantic would be fruitless, since there are presently no sea-based electric field sensors. On the other hand, research is quite warranted in tracking small storms within the Cape.
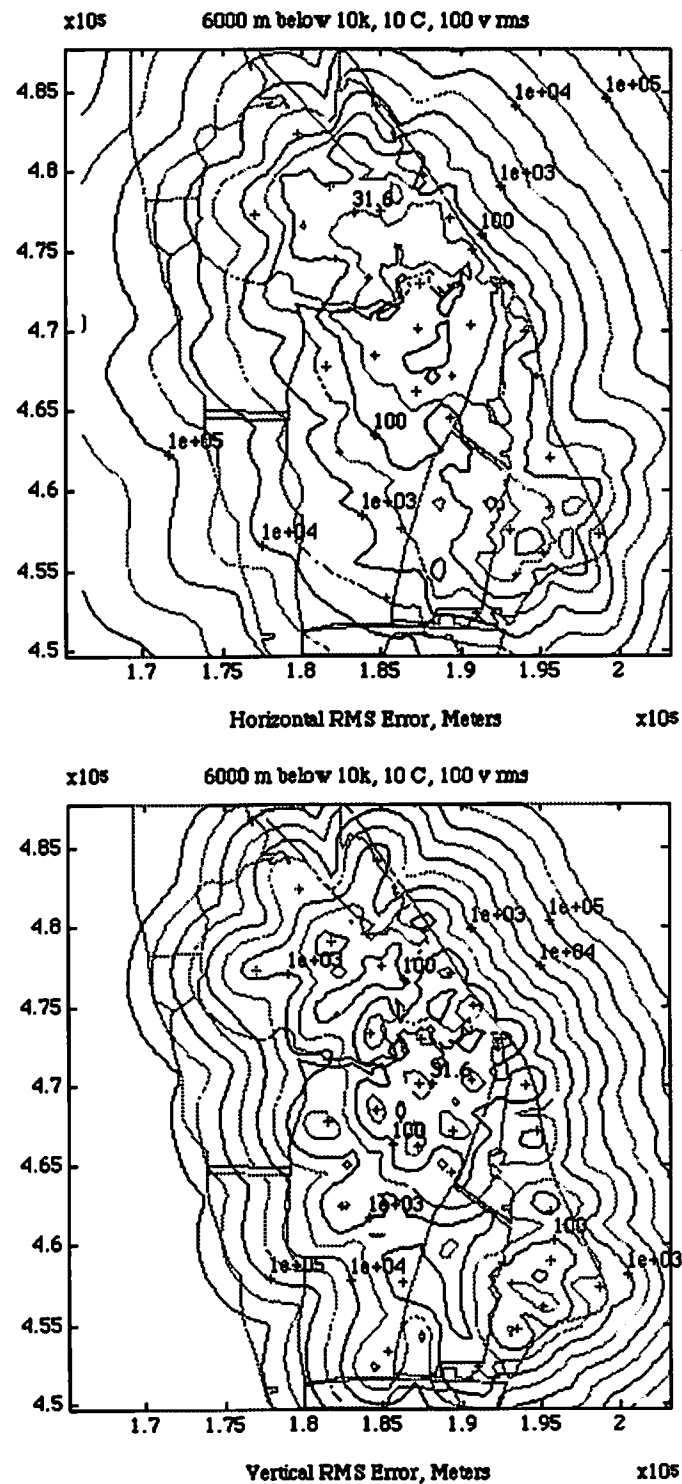
FIGURE 39. Dual point charge at 6,000 and 10,000 meters. The figures represent the one standard deviation error in locating the source (horizontally and vertically) at 6,000 meters. Compare with Fig. 38.

121

Chapter 9
Time-Eigenspectrum Analysis

Time-eigenspectrum (TE) analysis is a novel method of examining the similarity of the response of several sensors over a prescribed block of time. In MEG data, the evoked response is quasi-static transient, sometimes separated in time into distinct response regions. Between the regions lies very low SNR data that corrupts the localization estimates. In thunderstorm data, the response of the array between lightning strikes exhibits a strong degree of correlation, consistent with the simple quasi-static charge model. The lightning strikes result in field changes quite dissimilar at the sensors, due to the non-static nature of the excitation and the nonlinear reaction of the nearby sensors. In either situation, we objectively seek a suitable window in time that surrounds the quasi-static signal and excludes either the very noisy regions or the dissimilar lightning strikes.

9.1 Statement of Problem

Least-squares and subspace estimators implicitly or explicitly make use of the spatial correlation matrix. In a typical MEG application, we might collect 200 ms of data, yet observe that the signal only exists from about 75 ms to 125 ms. If we form the spatial correlation matrix from the entire 200 ms of data, we reduce the SNR in the correlation matrix by effectively averaging in too much noise, which degrades estimator performance.

As an example, we simulated a spherical head model and 37 sensor array pattern, as described in Chapter 8 and (Mosher *et al.* 1993). We simulated the placement of two

dipoles spaced two cm apart just under the surface of the skull, and gave each dipole a Hamming window shaped activation sequence with a peak amplitude of 10 nanoamps. The sequences were arranged such that the first dipole fired completely, then the second dipole fired with no overlap with the first. The overlay of all simulated time series measured at the 37 sensors is shown in the top portion of Fig. 40.

A nonlinear least squares estimator (as described in Chapter 4 and in (Mosher *et al.* 1992)) was then run with 200 different realizations of white random noise with a standard deviation of 70 femtoteslas. The choice of signal strength and noise selections are described in Section 8.1 and in (Mosher *et al.* 1993). The standard deviations on the localization error for the two dipoles was 1.81 mm and 2.14 mm, when estimated using all of the data.

We then partitioned the sequence in half, reducing the estimation to two one-dipole problems. The standard deviation on the localization error drops to 1.00 mm and 1.13 mm for the two dipoles. Thus the partitioning of the data from one two-dipole problem into two one-dipole problems improved the efficiency of the estimator.

This simulation assumed known model order. By focusing the problem to two one-dipole problems, the nonlinear estimator can discard noisy snapshots that degrade its performance. As discussed in Chapter 5, MEG-MUSIC was introduced to overcome some of the problems with order selection and local minima encountered in nonlinear least-squares. However, estimating the subspace also requires careful attention to partitioning, since the subspace estimates are sensitive to noisy snapshots.

In order to improve the subspace and localization estimates, we must identify the extents of the events of interest and partition the time series accordingly. Most signal detection algorithms rely on an explicit temporal model, but temporal models in MEG research are subject to controversy. Consequently, a nonparametric approach to partitioning is more appropriate.

9.2 Solution Approach

We approach the partitioning problem by using the temporal coherence across the sensors evident from the quasi-static formulation of the problem. As the intensity of a dipolar source fluctuates, its signal arrives simultaneously at all sensors. If we place an appropriately sized window at the proper instance in time around a single dipole, we find that the rank of this window is one, i.e., the temporal signals arriving at all sensors are perfectly coherent. If two independent signals are active in this window, we observe that the rank is two.

At a particular instance in time, we begin the analysis by creating a window of width one. Obviously, a single time slice is perfectly similar with itself. We proceed by adding the previous time slice to form a window of width two, then three, four, etc., until we reach some upper window width by design or data limitation. For each window width, we take a measure of the similarity of the window, described below. We then slide this window forward one time slice, and repeat the process. The result is a two-dimensional function, $f(t,w)$, with one dimension corresponding to the most recent sample, t, in the window and the other the window width, w.

The similarity measure we employ is multidimensional and is derived from the singular values obtained from an SVD of the window. We form a matrix from w sequential snapshots of the data, ending at time slice $A(t)$. Denoting the singular values by the ordered vector $s(t,w)$, we form a vector of the cumulative square of the singular values,

normalized by the sum of the squared singular values. Thus, the jth element of the vector similarity measure at time t for window width w is calculated as

$$s(t, w) = \text{svd}(\,[A(t - w + 1)\ldots A(t)]\,)$$

$$f_j(t, w) = \frac{\displaystyle\sum_{i=1}^{j} s_i^2(t, w)}{\|s(t, w)\|^2} \qquad\qquad \text{(EQ 75)}$$

for $j = 1,\ldots,\min(w,m)$, where m is the number of sensors.

The element of our measure vector that approaches unity is our indication of the rank of the window; the last element of f is always unity. Thus a rank two window would have its second and greater elements equal to 1. In practice, noise always prevents such a perfect rank estimate, but this SVD-based measure f allows us to observe at which element we are "close enough" to a lower rank matrix.

9.2.1 Simulation

Using the Hamming-shaped activation sequence described in Section 9.1, we simulated two dipoles firing sequentially. The noiseless time series was five points of no signal, then a 40 point Hamming sequence for the first dipole, then a 40 point Hamming sequence for the second, then finally 5 points of no signal, for a total of 90 samples. The time trace across all 37 simulated sensors is shown in the top portions of Fig. 40 and Fig. 41, with additive random white noise; the standard deviation was 70 femtoteslas. The bottom portions of these figures show the rank 1 and rank 2 time-eigenanalysis contours, i.e., $f_1(t,w)$ and $f_2(t,w)$ respectively. The abscissa gives the time index of the leading edge of the window, and the ordinate gives the width of the sliding window.

The contour intervals indicate the percentage of total "energy" (square of the Frobenius norm) in the window contained in the subspace. In Fig. 40, the contours are above 80% for small windows centered on the responses, indicating that 80% of the sig-
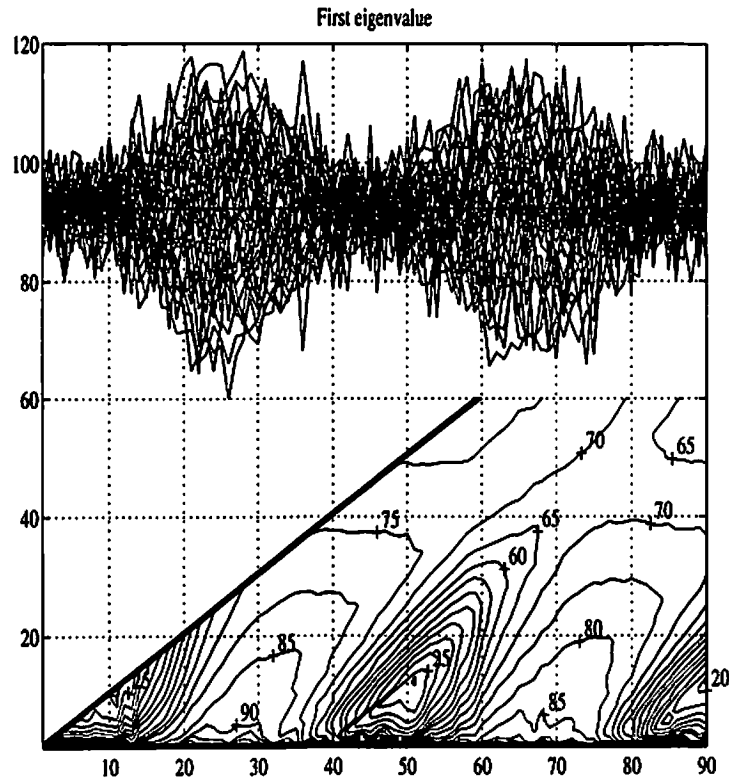
FIGURE 40. Simulation Time-Eigenspectrum. The rank 1 contour plots reveal that the two signals together are insufficiently described by a rank one subspace. Each signal can however be temporally isolated.

nal energy in the given window can be described by the first eigenvalue. The contours rapidly drop for small windows centered on the noise intervals, and the contour shows that the first eigenvalue only accounts for 25% of the signal energy in the transition and end regions. Although the center of the responses is visible in this simulated data, the transitions in the contours more clearly show the segments dominated by either noise or signal.

In Fig. 41, the contours represent the percentage energy contained by the first two dipoles. The windows containing only one active dipole show small increases in percentage energy that those containing both dipoles. The 75% contours are beginning to

126
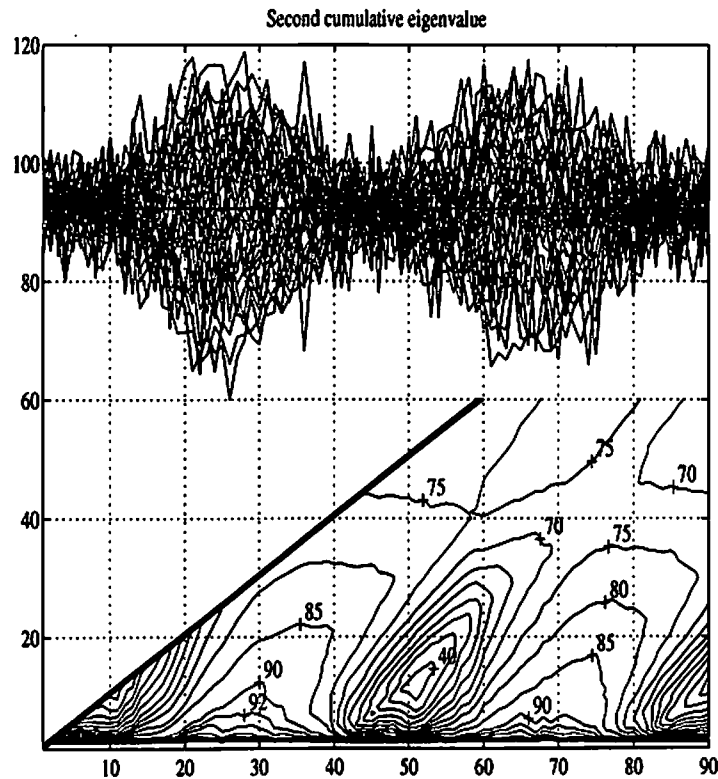
FIGURE 41. Simulation Time-Eigenspectrum (cont'd). The rank 2 contour plots reveal that the individual responses are not much improved with a second eigenvalue.

merge in the upper regions which represent windows that encompass both dipoles. Although the noiseless data is rank two, the proximity of the dipoles and the intensity of the noise make it difficult in this simulation to distinguish the overall data as rank two; however, we do appear clearly justified in partitioning the data into two distinct sets.

This simulation is somewhat transparent, since the two response sequences are mostly visible, and prudent partitioning might be possible by inspection alone. However, the simulation was simplified to highlight some of the contours seen in actual data and to assist in their interpretation. In this next example, we show the utility in partitioning a less obvious simulation.
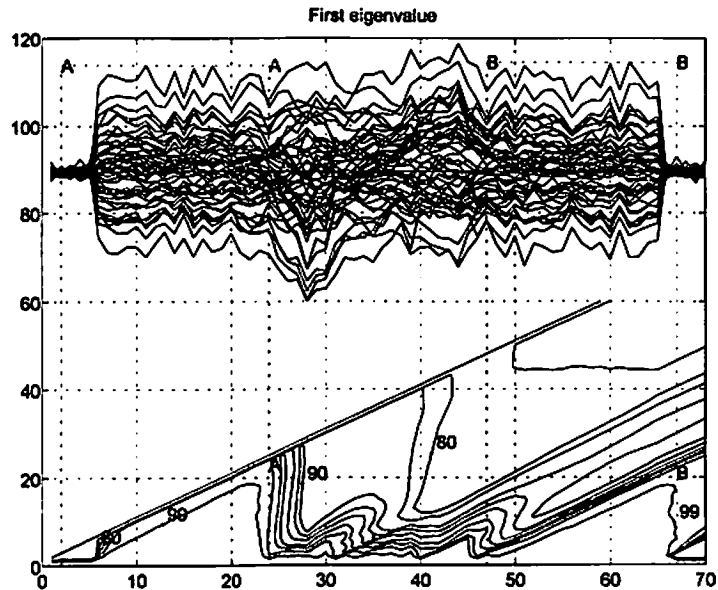
FIGURE 42. Rank 1 analysis of one simulated signal buried inside the other. The symbols "A" and "B" delineate the rank 1 regions.

In this simulation, one signal is of a relatively constant amplitude for about 60 samples, while the second signal is a bipolar signal of about 30 samples, generated from a double Hamming sequence. The second signal begins about 25 samples into the simulation. Fig. 42 and Fig. 43 show the rank 1 and rank 2 analysis. The rank 2 analysis clearly shows only two signals exist, while the rank 1 analysis allows us to partition the region around the second signal. The letters "A" and "B" in the contours correspond to the partitioned regions similarly marked in the overlay.

In the next example, we apply this technique to MEG somatosensory data.

128
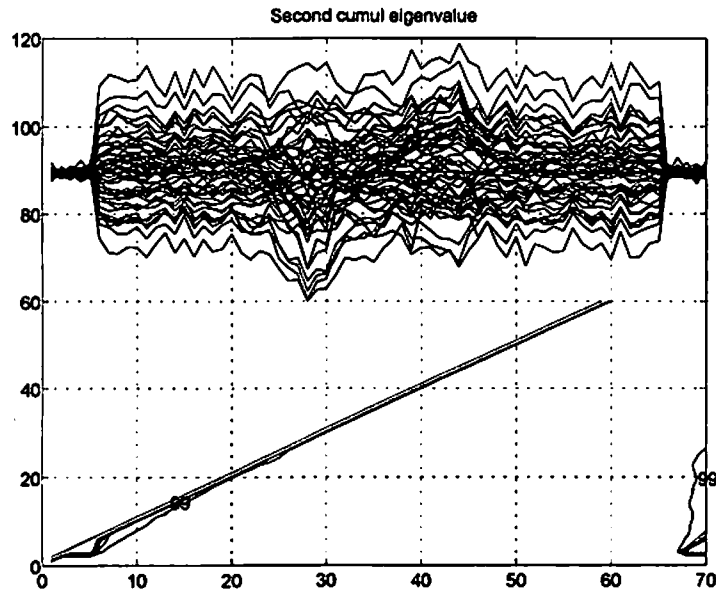
FIGURE 43. Rank 2 analysis of simulated signal buried within another. The signal is everywhere described by a rank 2 model.

9.2.2 Somatosensory Response

In this experiment, biomagnetic sensors at 77 positions about the surface of the head recorded the evoked response of the ring finger to piezoelectric stimulation. Fig. 45 and Fig. 45 show in their top portions the overlay of the response (averaged from 300 trials) across all sensors. The time index corresponds to 2 ms intervals, and the first 20 samples visible are part of the pre-stimulus interval. A stimulus artifact is present at time sample 55, and the first dominant neural response occurs 40 ms later at time index 75. A secondary response is evident beginning around time sample 100.
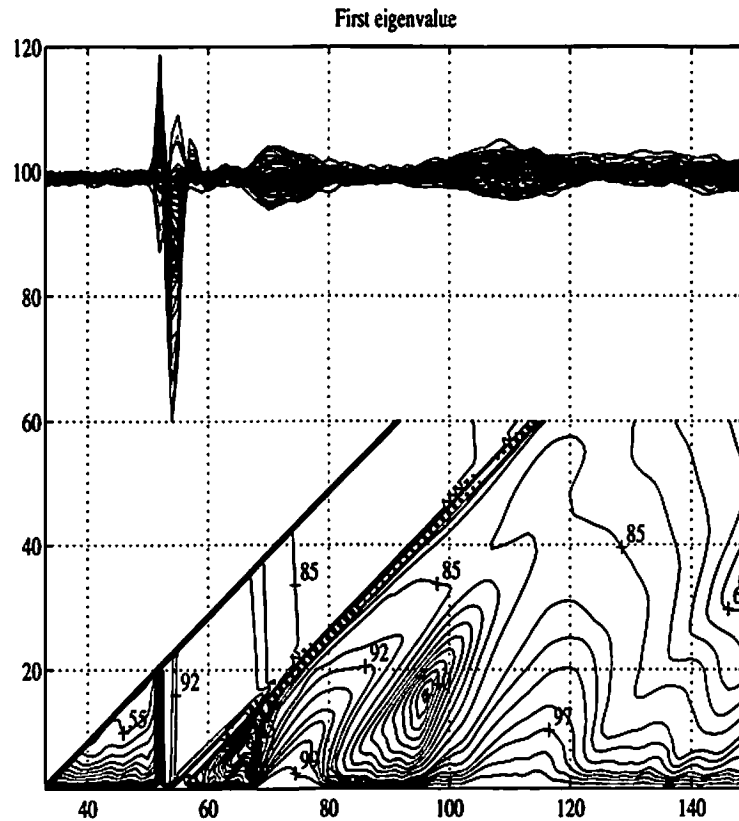
FIGURE 44. Ring Finger Stimulation, Rank 1 analysis.

We ignore the stimulus artifact and focus on the two evoked responses. The contours indicate that the first response is of low rank for only about 15 samples and is preceded and followed by relatively incoherent and low power regions. The second response appears to lie more appropriately in a rank 2 subspace, but only up to about time sample 125. Although the signal levels remain relatively active beyond sample 125, the contours indicate a drop in similarity.

The contour transitions guide how we might partition the data to extract the two responses. The first response region is also obvious in the data, but not so obvious is the high rank of the low power regions surrounding it. The onset of the second response is
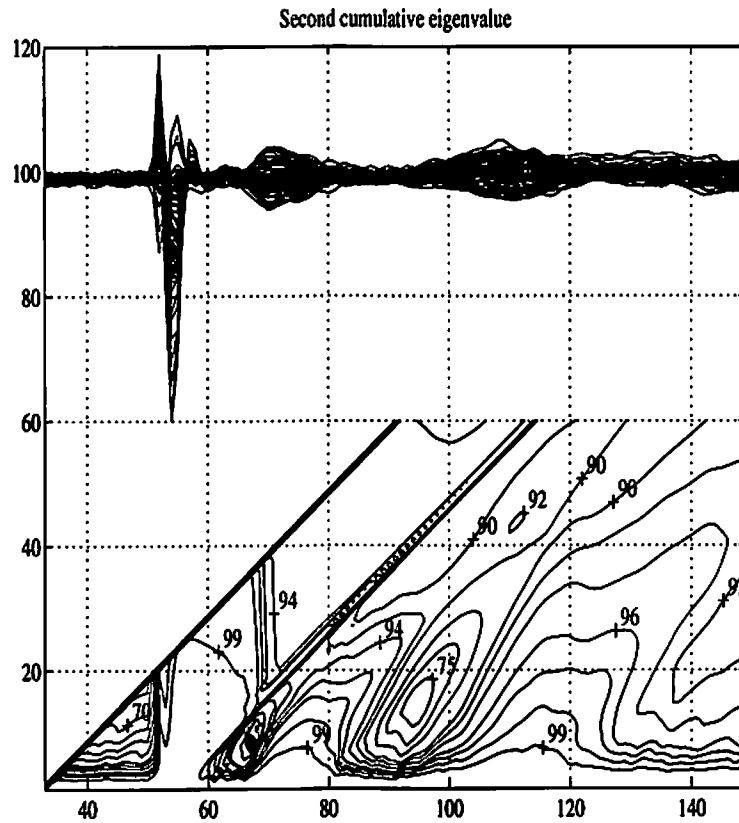
FIGURE 45. Ring Finger Stimulation, Rank 2 analysis.

also somewhat visible in the data, but the contours assist in trimming the late time of the response, where visible inspection of the data does not indicate where we should trim.

Finally, we comment on the computational load in performing the numerous SVDs required. The examples presented each required about five minutes on a SPARC 330 or fifteen minutes on a 486-33 MHz, both running MATLAB.

9.3 Thunderstorm Time-Eigenspectrum

The thunderstorm application of time-eigenanalysis offers a novel method for isolating the lightning strikes from the more static regions of the field mill data streams. Present NASA KSC methods center on attempting to detect large discontinuities in indi-

131

vidual mill streams, then confirming that several other mills have observed a similar jump. The time-eigenspectrum displays graphically display the lightning strikes quite visibly, and the time-eigenspectrum images appear to proportionately respond to the intensity of the flash; distant flashes appear only as minor changes in the images, but they are apparent.

If the window contains a lightning strike segment, the dissimilarity (or signal processing incoherence) of the event will decrease our similarity measure. For the quasi-static MUSIC processing, we desire as large a processing window as possible, yet still avoid these incoherent lightning strikes. Interpretation of the time-eigenanalysis gives us just such a partitioning tool objectively.

We present a simulated thunderstorm example, then follow with two actual thunderstorm studies.

9.3.1 Two Charge Simulation

In this simulation, rather than simulate lightning strikes, we instead abruptly jump the storm cell to the next spatial position in a sequence of positions. Fig. 46 presents the time-eigenspectrum of the simulated data. The top portion of the figure repeats the overlay of all time series for reference. The middle portion of the figure is the rank one spectrum and the bottom portion the rank two. We see in the rank one analysis vertical drops in the contour lines. These lines occur on the transition boundaries between two distinct storm positions. In this simulated data, we could select a horizontal threshold boundary to trigger on these collapsing spectral contours and partition the data accordingly.
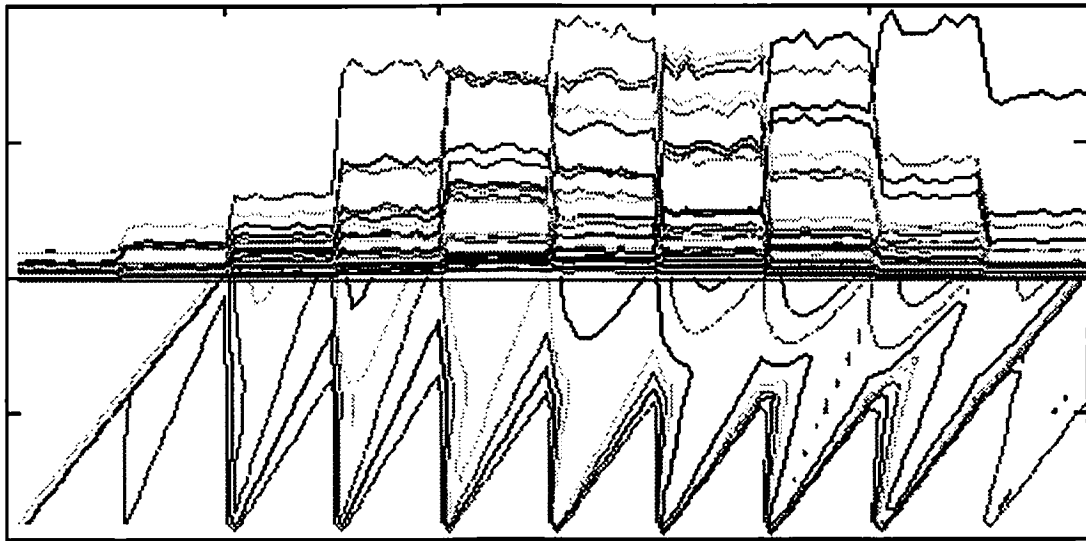
FIGURE 46. Simulation time eigenanalysis. The top portion of the figure shows the same overlay as shown in Figure 21 on page 70 for reference here. The lower portion of the figure shows the rank 1 time-eigenanalysis. The abrupt vertical changes in the time-eigenanalysis match identically with the obvious changes in the field overlay. Thus time-eigenanalysis gives us an objective indicator of sudden changes in the field.

9.3.2 Intense lightning example

Fig. 47 is 200 seconds of thunderstorm data during heavy lightning activity. In contrast to the simulation above, the discontinuities in the data are now due to lightning strikes disrupting the quasi-static electric field of the charged sources. The maximum window width was arbitrarily set to 60 seconds, and we see particularly in the rank one analysis no window that would have allowed such a wide window without including some lightning activity. We observe how each lightning strike apparent in the field mill data corresponds to a rapid vertical collapse of the contour lines in the time-eigenspectrum analysis. In the time window immediately preceding many of the major strikes, we see relatively clear time-eigenspectrum regions, represented by the right triangular shapes in the lowest portions of the contours. We thus have many small windows that can be extracted out of the overall disrupting lightning activity for further processing.
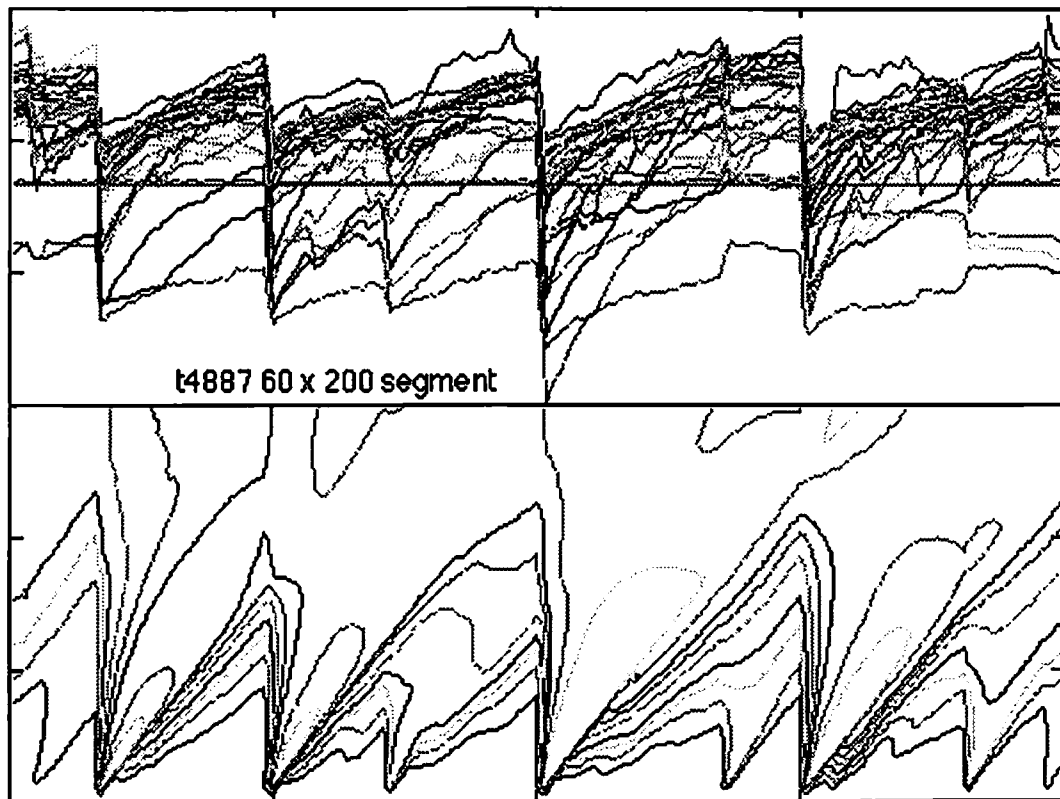
FIGURE 47. Time-eigenspectrum. Over a 200 second segment, we see the electric fields climbing to about 10 kV/m before a strike. After the strike, the spectrum lines condense, the gradually relax as the field mill data resumes a quasi-static state. These quasi-static regions are exactly the regions we need to process for successful point charge modeling.

Using the initial time-eigenanalysis, we stripped out many of the large lightning events, reducing 600 seconds of thunderstorm data down to 360 seconds. We then reran the time-eigenanalysis to again check the coherence of these mill data without many of the intervening lightning strikes. We note that this "strip and reanalyze" method can be repeated until most significant lightning events have been detected and removed. Here we stopped the process after just one iteration to test the robustness of the MUSIC algorithm. We also note the significant coronal damping of the fields, as seen by the exponential clamping of the signals.

Fig. 48 presents the time-eigenanalysis of these 360 seconds. Now we note much wider processing windows of high coherence. Rather than handpick these windows, we

134
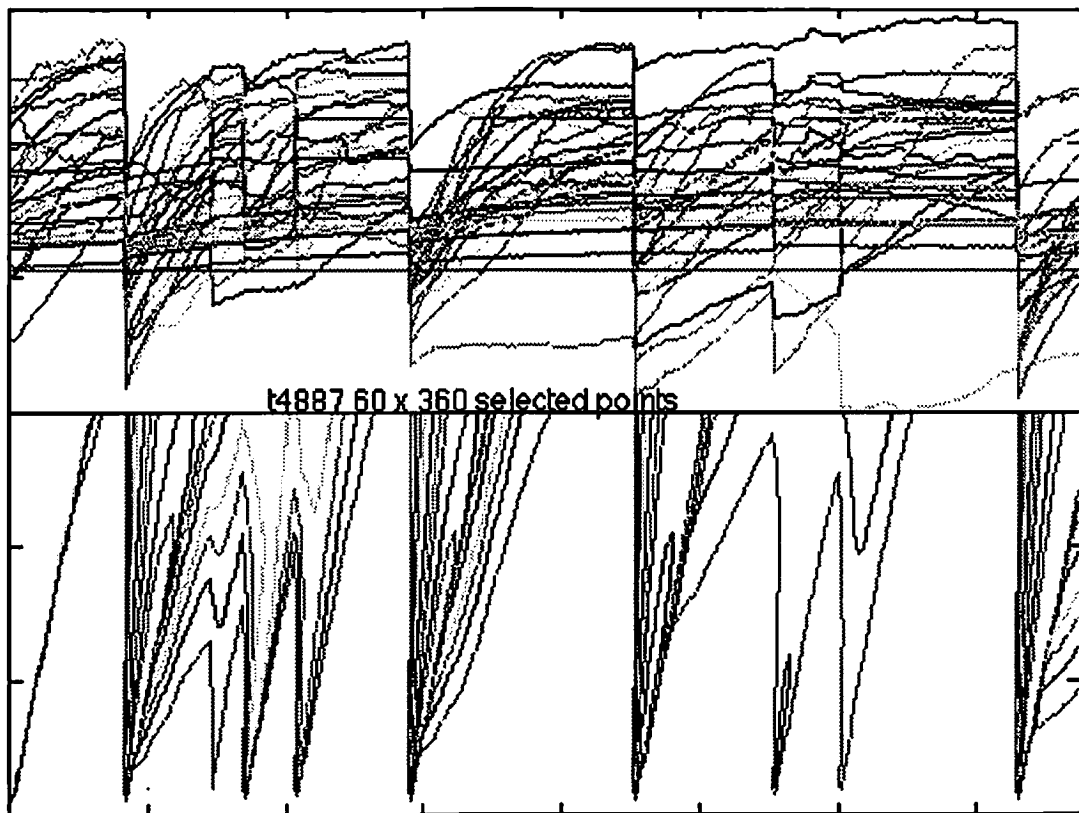
FIGURE 48. Time-eigenspectrum for trimmed data. 600 seconds were trimmed of major lightning events into the 360 total seconds seen here. Significant coronal damping of the fields were occurring, as seen by the exponential clamping of the signals. Rather than carefully select time segments, we evenly divided the entire time segment into six segments of 60 seconds each to test the robustness of the MUSIC algorithm.

instead divided these data into six even windows of 60 seconds each. Clearly some of these six windows contain incoherent time slices, as indicated by the vertical contour lines. We reasoned that an on-line processing algorithm may unavoidably retain such incoherent data, since an experienced operator may not be available to hand pick these processing windows. We therefore sought to examine the MUSIC results under a range of data quality, to stress the emphasis of successful processing under somewhat realistic on-line decisions. The MUSIC results for this set of parsed windows is presented in Figure 25 on page 75.

135

9.3.3 End-of-Storm-Oscillations example

We present here an intriguing novel look at an End-of-Storm-Oscillation (EOSO). In Fig. 49, the figures are an enlargement of just the last hour of the August 5, 1991 data, shown completely in Figure 4 on page 14. The MUSIC processing was applied to test the robustness of the point charge model with relatively static data, yet this data is believed to be degenerating from a point charge into wide spread electrical storm debris. No lightning strikes were observed during the EOSO.

Fig. 50 is the EOSO time-eigenspectrum. The spectrum shows relatively good coherence over five minutes, but does not appear to warrant a much wider window. This observation would be consistent with a storm cell either moving or dispersing. We selected a five minute segment early and late in the EOSO for MUSIC processing.

Fig. 51 is the EOSO MUSIC scans. The top figure is approximately 20 minutes into the EOSO, the bottom figure approximately 50 minutes. Both MUSIC spectra were based on a five minute window. Although the field levels were still above 2 kV/m in the right figure, and the eigenspectrum indicated good coherence, the point charge model intersected quite poorly with the data. We contrast this result with the earlier EOSO data at the top, where still get relatively good intersection of the MUSIC scan. This lack of intersection in the late time is quite consistent with the belief that the storm center should then be well dispersed and poorly modeled as a point charge.

9.3.4 Time-Eigenanalysis Summary

Time-eigenanalysis is an effective tool for measuring the subspace dimension of the KSC array. During time regions of low dimensionality, namely between lightning strikes, then we have a greatly improved opportunities for applying the simplistic point charge model and the MUSIC processing. Conversely, the high rank regions give an
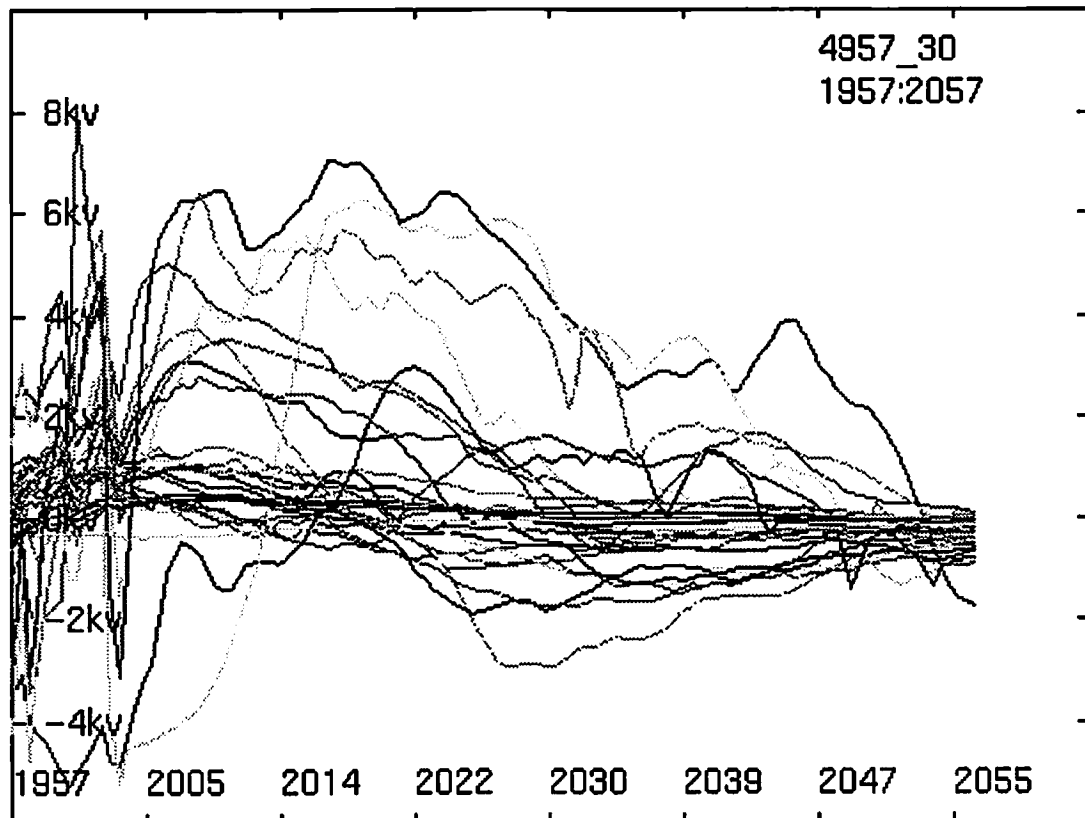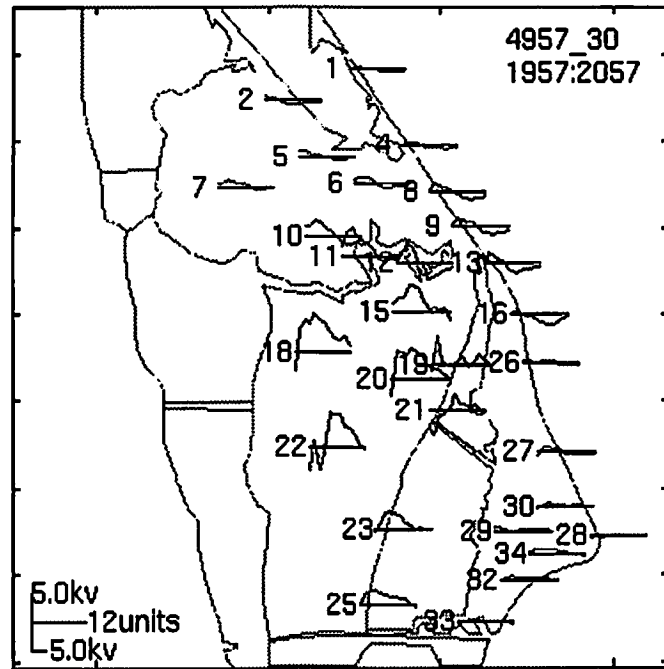
FIGURE 49. End-of-storm oscillation study. The figures are an enlargement of just the last hour of the August 5, 1991 data. The time-eigenspectrum and MUSIC processing were applied to test the robustness of the point charge model with relatively static data.
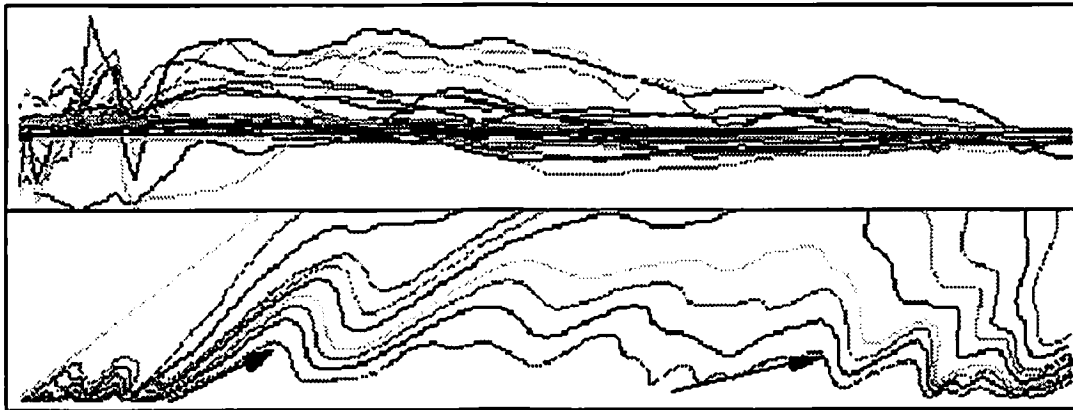
FIGURE 50. The time-eigenspectrum shows relatively good coherence over five minutes, but does not appear to warrant a much wider window. This observation would be consistent with a storm cell either moving or dispersing. We selected five minute segments early and late in the EOSO for MUSIC processing.

excellent indication of the lightning strike temporal extent. These regions could be extracted for further lightning based processing. Proper thresholding of the time-eigenspectrum contour lines would allow the automatic switching between source models and lightning models during the real-time progress of the storm.
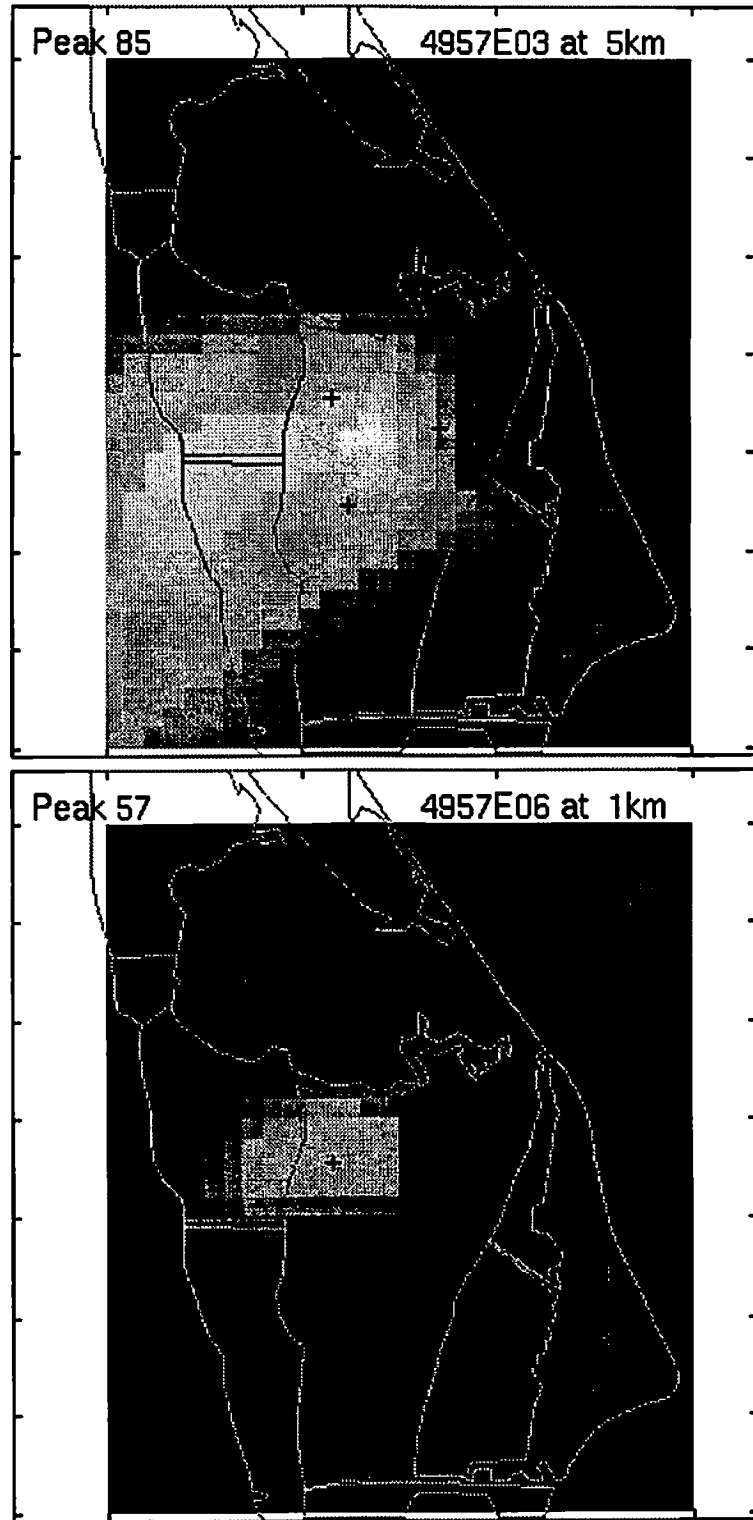
FIGURE 51. EOSO MUSIC. The top figure is approximately 20 minutes into the EOSO, the bottom approximately 50 minutes. Both MUSIC spectra were based on five minute windows.

Chapter 10
Summary and Further Research

Sometimes a scream is better than a thesis. —Ralph Waldo Emerson

We have presented general descriptive models for spatiotemporal data and have shown the separability of the linear moment parameters and nonlinear location parameters in the MEG problem. A forward model with current dipoles in a spherically symmetric conductor was used as an example; however, by the superposition of electromagnetic sources, other more advanced MEG models, as well as many EEG models, can also be formulated in a similar linear algebraic framework. A subspace methodology and computational approach to solving the conventional least-squares problem was then presented. A secondary application of these techniques to the thunderstorm localization problem was also presented.

A new scanning approach, equivalent to the statistical MUSIC method, was developed. This subspace method scans three-dimensional space with a one dipole model, making it computationally feasible to scan the complete head volume. Least-squares and MUSIC demonstrations were presented using simulated noisy data, phantom data and somatosensory MEG data. In general, MUSIC may fail when the noise is of sufficient strength to corrupt the estimates of the noise subspace, when the time series are strongly correlated, or when the sources are closely spaced. Many other authors have analyzed the performance of MUSIC, particularly the sensitivity of the results to errors in estimation of the noise subspace, and have also suggested many modifications of the algorithm (Stoica and Nehorai 1989, Stoica and Sharman 1990, Cadzow 1990, Viberg 1989, Viberg and Ottersten 1991). These results may prove useful in improving the sub-

space scanning method described here. The challenge lies in advancing these methods for actual data where the noise statistics are unknown. The appeal lies in the relative simplicity with which the entire head region is scanned.

General formulas were presented for computing the lower bound in localization and moment error. Specific MEG and EEG formulas were presented for multiple dipoles in a head model with four spherical shells. Localization error bounds were presented for MEG, EEG, and thunderstorm models with different sensor and source configurations. Both one and two dipole cases were examined for all possible dipole orientations and locations within a head quadrant. The results showed a strong dependence on absolute dipole location and orientation. The results also showed that fusion of the EEG and MEG measurements into a combined model reduced the lower bounds. The thunderstorm results showed good localization potential within the Cape Canaveral region.

The time-eigenspectrum analysis provided a novel and objective means of parsing the time data into processing segments. Simulations were presented for multiple sources, then the technique was applied to somatosensory and thunderstorm data. The results appear useful in characterizing the temporal extent of the MEG transient evoked response, and the results appear particularly useful in removing unwanted lightning strikes from the thunderstorm data.

In the application of these methods to data, practical questions arise which are of future interest. Overspecifying the signal subspace domain by one or two dimensions does not appear to significantly alter the results. The original peaks increase somewhat, but spurious peaks do not necessarily appear; however, it is not immediately obvious as to what degree we can exceed the true dimension of the subspace. Linked to this problem is distinguishing a "significant" MUSIC peak from a local maximum in the MUSIC images, i.e., how far reduced from unity are the noisy source peaks. The SNR threshold

and signal subspace small perturbation work of Li and Vacarro (1991) appears to provide preliminary approaches to the problem.

This work has investigated the modeling for the *spatial* component of the spatiotemporal data matrix. Models for *temporal* component of the data are more difficult to assign, yet their inclusion will assist in an overall better understanding of the neural signals. The preliminary models must be quite general, to prevent us from unduly constraining the class of signals accepted. High dimensional state-space identification techniques such as Kung's (1979) appear promising for exploiting the multi-channel data information available from the array of sensors.

Bibliography

Achim A, Richer F, and Saint-Hilaire J, "Methods for separating temporally overlapping sources of neuroelectric data," *Brain Topography*, vol. 1, no. 1, pp. 22--28, 1988.

Achim A, Richer F, Saint-Hilaire JM, "Methodological considerations for the evaluation of spatiotemporal source models," *Electroenceph. clin. Neurophysiology.*, 1991, 79: 227 - 240.

Anogianakis G, Badier JM, Barret G, et al. "A consensus statement on relative merits of EEG and MEG," Editorial, *Electroenceph. clin. Neurophysiology.*, 1992, 82: 317 - 319.

Arthur RM, Geselowitz DB, "Effect of inhomogeneities on the apparent location and magnitude of a cardiac dipole source," *IEEE Trans. Biomedical Eng,* 1970, 17: 141-146.

Ary JP, Klein SA, and Fender DH, "Location of sources of evoked scalp potentials: corrections for skull and scalp thicknesses," *IEEE Trans. Biomedical Eng.*, 1981, 28: 447-452.

Alvarez RE, "Biomagnetic Fourier imaging," *IEEE Transactions on Medical Imaging,* vol. 9, pp. 299--304, September 1990.

Balish M, Sato S, Connaughton P, and Kufta C. "Localization of implanted dipoles by magnetoencephalography," *Neurology* 1991; 41:1072-1076.

Baumgartner C, Sutherling WW, Di S, and Barth DS, "Spatiotemporal modeling of cerebral evoked magnetic fields to median nerve stimulation," *Electroenceph. clin. Neurophysiol.*, 1991, 79: 27 - 35.

Brody DA, Terry FH, and Ideker RE, "Eccentric dipole in a spherical medium: generalized expression for surface potentials," *IEEE Trans. Biomedical Eng.*, 1973, 20:141-143.

Cadzow JA, "Multiple source location -- The signal subspace approach," *IEEE Transactions on Acoustics, Speech and Signal Processing*, vol. 38, pp. 1110--1125, July 1990.

Chen W, Wong KM, and Reilly JP, "Detection of the number of signals: A predicted eigen-threshold approach," *IEEE Transactions on Signal Processing,* vol. 39, pp. 1088--1098, May 1991.

Cohen D, and Cuffin BN, "Demonstrations of useful differences between magnetoencephalogram and electroencephalogram," *Electroenceph. clin. Neurophysiol.* 1983, 56:38-51.

Cohen D, Cuffin BN, Yunokuchi K, Maniewski R, Purcell C. Cosgrove GR, Ives J, Kennedy JG, Schomer DL. "MEG versus EEG localization test using implanted sources in the human brain," *Ann Neurol* 1990, 28:811-817.

Cuffin BN, Cohen D, "Comparison of the magnetoencephalogram and electroencephalogram," *Electroenceph. clin. Neurophysiol.*,1979, 132-146.

Cuffin BN, "Effects of measurement errors and noise on MEG moving dipole inverse solutions," *IEEE Trans. Biomedical Eng.*, 1986, 33: 854 - 861.

Cuffin BN, "Effects of head shape on EEG's and MEG's," *IEEE Trans. Biomedical Eng.*, 1990, 37:44-52.

Cuffin BN, "Eccentric spheres models of the head," *IEEE Trans. Biomed. Engr.*, 1991, 38: 871-878.

Dallas W, "Space solution to the magnetostatic imaging problem," *Applied Optics*, vol. 24, no. 24, pp. 4543--4546, 1985.

de Munck JC, "The estimation of time varying dipoles on the basis of evoked potentials," *Electroencephalography and clinical Neurophysiology*, vol. 77, pp. 156--160, 1990.

Dongarra JJ, Moler CB, Bunch JR, and Stewart GW, *LINPACK User's Guide*. Philadelphia: the Society for Industrial and Applied Mathematics, 1979.

George JS, Aine CJ, Medvick PA, and Flynn ER, "Spatial/temporal resolution of multiple sources: Paths of activation in human visual cortex," in *Advances in Biomagnetism* (S. Williamson *et al.*, eds.), pp. 197--200, New York, NY: Plenum Press, 1989.

Golub GH and Pereyra V, "The differentiation of pseudo-inverses and nonlinear least squares problems whose variables separate," *SIAM Journal Numerical Analysis*, vol. 10, pp. 413--432, April 1973.

Golub GH and Loan CFV, *Matrix Computations*. Baltimore, MD: The Johns Hopkins University Press, 1983.

Golub GH and Loan CFV, *Matrix Computations*. Baltimore, MD: The Johns Hopkins University Press, second ed., 1989.

Guttman I and Pereyra V, "Least squares estimation for a class of non-linear models," *Technometrics*, vol. 15, pp. 209--218, May 1973.

Hari R., Hamalainen M, Ilmoniemi, Lounasmaa R, "MEG versus EEG localization test," Letter to the Editor, *Ann Neruol.* 1991, 30: 222-223.

Ilmoniemi RJ, Hamalainen MS, and Knuutila J, " The forward and inverse problems in the spherical model," *Biomagnetism: Applications and Theory*, ed. Wienberg, H., Stroink, G. and Katila, T. 1985, Oxford: Pergamon Press, pp 278-282.

Jeffs B, Leahy R, Singh M, "An evaluation of methods for neuromagnetic image reconstruction," *IEEE Trans. Biomedical Eng.*, 1987, 34:713-723.

Kaufman L, Kaufman JH, Wang, JZ. "On cortical folds and neuromagnetic fields," *Electroenceph. clin. Neurophysiol.*, 1991, 79: 211 - 226.

Kung S, "A new identification and model reduction algorithm via singular value decomposition," *Conference Record Twelfth Asilomar Conference on Circuits, Systems & Computers*, Pacific Grove, November 1978, pp 705-714.

Lewis PS, Mosher JC, and Leahy RM, "A new approach to neuro-magnetic source localization," *IEEE Conf. on Engineering in Medicine and Biology, Satellite Symp. on Neuroscience and Technology*, Lyon, France, Nov. 2-4, 1992.

Maier J, Dagnelie G, Spekreijse H, and van Dijk B, "Principal Components Analysis for source localization of VEPs in man," *Vision Research*, vol. 27, no. 2, pp. 165--177, 1987.

Maier LM., and Strange TR, "Electric Field Mill Training Handbook," *Computer Sciences Corporation* Kennedy Space Center, Contract NAS10-11400, January 1988.

The Mathworks, Inc., South Natick, MA 01760, *PRO-MATLAB*, 1990.

McGillem CD, Aunon JI, and Yu K., "Signals and noise in evoked brain potentials," *IEEE Trans. Biomedical Eng.*, 1985, 32: 1012 - 1016.

Mocks J and Verleger R, "Principal Component Analysis of event-related potentials: A note on misallocation of variance," *Electroencephalography and clinical Neurophysiology*, vol. 65, pp. 393--398, 1986.

Mosher JC, Lewis PS, Leahy RM, Singh M, "Multiple dipole modeling of spatio-temporal MEG data," In A.F. Gmitro, et al. (Eds.) *Digital Image Synthesis and Inverse Optics*, San Diego, CA, July 1990, Proc. SPIE 1351:364-375.

Mosher JC, Lewis PS, Leahy RM, "Spatial localization of neural sources using the magnetoencephalogram," *Fifth ASSP Wkshp on Spectrum Estimation and Modeling*, Rochester, NY, Oct 1990:289-293.

Mosher JC, Lewis PS, Leahy RM, "Subspace methods for identifying neural activity from electromagnetic measurements of the brain," *IEEE Proc. 25th Asilomar Conf. on Signals, Systems, and Computers*, Pacific Grove, CA, Nov. 1991:237-241.

Mosher JC, Lewis PS, Lewine J, George J, Leahy RM, Singh M, "Electromagnetic imaging of dynamic brain activity," *Proc. IEEE 1991 Medical Imaging Conf*, Sante Fe, NM, Nov 1991.

Mosher JC, Lewis PS, and Leahy RM, "Multiple dipole modeling and localization from spatio-temporal MEG data," *IEEE Trans. Biomedical Eng*, 1992, 39:541-557.

Mosher JC, Spencer ME, Leahy RM, Lewis PS, "Cramer Rao Lower Bounds for the MEG dipole source localization," *IEEE Proc. 26th Asilomar Conf. on Signals, Systems, and Computers*, Pacific Grove, CA, October 1992.

Mosher JC, Leahy RM, Lewis PS, "Biomagnetic localization from transient quasi-static events," *IEEE Acoustics, Speech, and Signal Processing Conference 1993*, Minneapolis, MN, April 1993.

Mosher JC, Spencer ME, Leahy RM, Lewis PS, "Error bounds for EEG and MEG dipole source localization," *Electroenceph. and clin. Neurophys.* (accepted for publication 1993).

Nunez PL, "The brain's magnetic field: Some effects of multiple sources on localization methods," *Electroencephalography and clinical Neurophysiology*, vol. 63, pp. 75--82, 1986.

Oshiro O, Mukai M, Takeuchi F, and Kuriki, S., "Analysis of errors in neuromagnetic localization of multiple current dipole sources," *Phys. Med. Biol.*, 1992, 37:845-852.

Romani GL and Leoni R, "Localization of cerebral sources by neuromagnetic measurements," in *Biomagnetism: Applications and Theory* (H. Weinberg, G. Stroink, and T. Katila, eds.), pp. 205--220, New York: Pergamon Press, 1984.

Sarvas J, "Basic mathematical and electromagnetic concepts of the biomagnetic inverse problem," *Phys. Med. Biol.*, 1987, 32:11-22.

Scherg M and von Cramon D, "Two bilateral sources of the late AEP as identified by a spatio-temporal dipole model," *Electroencephalography and clinical Neurophysiology*, vol. 62, pp. 32--44, 1985.

Scherg M and von Cramon D, "A new interpretation of the generators of BAEP waves I-V: Results of a spatio-temporal dipole model," *Electroencephalography and clinical Neurophysiology*, vol. 62, pp. 290--299, 1985.

Scherg M and von Cramon D, "Evoked dipole source potentials of the human auditory cortex," *Electroencephalography and clinical Neurophysiology*, vol. 65, pp. 344--360, 1986.

Scherg M, "Fundamentals of dipole source potential analysis," in *Auditory Evoked Magnetic Fields and Potentials, Vol. 6* (M. Hoke, F. Grandori, and G. L. Romani, eds.), Adv Audiol. Basel. Karger, 1989.

Schmidt RO, "Multiple emitter location and signal parameter estimation," *IEEE Transactions on Antennas and Propagation*, vol. AP-34, pp. 276--280, March 1986. Reprint of the original 1979 paper from the RADC Spectrum Estimation Workshop.

Singh M, Doria D, Henderson V, Huth G, and Beatty J, "Reconstruction of images from neuromagnetic fields," *IEEE Transactions on Nuclear Science*, vol. NS-31, pp. 585--589, 1984.

Sorenson, Harold W. *Parameter Estimation*. New York: Marcel Dekker, 1985.

Snyder AZ, "Dipole source localization in the study of EP generators: a critique," *Electroenceph. clin. Neurophysiol.*, 1991, 80: 321 - 325.

Stoica Pand Nehorai A, "MUSIC, maximum likelihood, and Cramer-Rao bound," *IEEE Transactions on Acoustics, Speech and Signal Processing*, vol. 37, pp. 720--741, May 1989.

Stoica P and Sharman KC, "Maximum likelihood methods for direction-of-arrival estimation," *IEEE Transactions on Acoustics, Speech and Signal Processing*, vol. 38, pp. 1132--1143, July 1990.

Stok CJ, "The influence of model parameters on EEG/MEG single dipole source estimation," *IEEE Trans. Biomedical Eng.*, 1987, 34: 289 - 296.

Strang G, *Linear Algebra and its Applications*. Orlando, Florida 32887: Academic Press, Inc., second ed., 1980.

Therapeutics and Technology Assessment Subcommittee, "Assessment: Magnetoencephalography (MEG)," *Neurology* 1992; 42: 1-4.

Trip JH, "Physical concepts and mathematical models," in *Biomagnetism: An Interdisciplinary Approach* (S. J. Williamson, ed.), pp. 101--149, Plenum Press, 1982.

Viberg M, *Subspace Fitting Concepts in Sensor Array Processing*. PhD thesis, Department of Electrical Engineering, Linkoping University, S-581 83 Linkoping, Sweden, 1989. Linkoping Studies in Science and Technology, Dissertations No. 217.

Viberg M and Ottersten B, "Sensor array processing based on subspace fitting," *IEEE Transactions on Signal Processing*, vol. 39, pp. 1110--1121, May 1991.

Westerkamp JJ, Aunon JI. "Optimum multielectrode a posteriori estimates of single-response evoked potentials," *IEEE Trans. Biomedical Eng.*, 1987, 34: 13 - 22.

Wikswo JP Jr., van Egeraat J, Ma YP, Sepulveda NG, Staton DJ, Tan S, and Wijesinghe RS, "Instrumentation and techniques for high-resolution magnetic imaging," in *Digital Image Synthesis and Inverse Optics* (A. F. Gmitro, P. S. Idell, and I. J. LaHaie, eds.), pp. 438--470, Proc. SPIE 1351, July 1990.

Williamson, SJ "MEG versus EEG localization test," Letter to the Editor, *Ann Neruol.* 1991, 30: 222.

Williamson SJ and Kaufman L, "Biomagnetism," *Journal of Magnetism and Magnetic Materials*, vol. 22, pp. 129--201, 1981.

Williamson SJ, Romani GL, Kaufman L, and Modena I, eds., *Biomagnetism: An Interdisciplinary Approach*. New York: Plenum Press, 1983.

Wilson FN, Bayley RH, "The electric field of an eccentric dipole in a homogeneous spherical conducting medium," *Circulation*, 1950, 1:84-92.

Wood CC, "Application of dipole localization methods to source identification of human evoked potentials," *Annals New York Academy Science*, vol. 388, pp. 139--155, 1982.

Wood CC and McCarthy G, "Principal Component Analysis of event-related potentials: Simulation studies demonstrate misallocation of variance across components," *Electroencephalography and clinical Neurophysiology*, vol. 59, pp. 249--260, 1984.